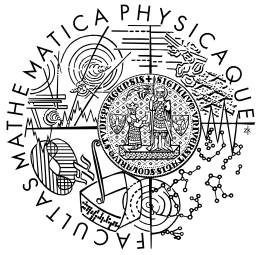

FACULTY
OF MATHEMATICS
AND PHYSICS
Charles University

DOCTORAL THESIS

Stanislav Valenta

Study of statistical γ decay in well-deformed rare-earth nuclei

Institute of Particle and Nuclear Physics

Supervisor of the doctoral thesis:	Doc. Mgr. Milan Krtička, Ph.D.
Study programme:	Physics
Study branch:	Nuclear Physics

Prague 2018

I declare that I carried out this doctoral thesis independently, and only with the cited sources, literature and other professional sources.

I understand that my work relates to the rights and obligations under the Act No. 121/2000 Sb., the Copyright Act, as amended, in particular the fact that the Charles University has the right to conclude a license agreement on the use of this work as a school work pursuant to Section 60 subsection 1 of the Copyright Act.

In Prague, August 3, 2018 signature of the author

From all the people that I wish to thank, I must start with women of my life – my girlfriend Simonka, my mom Vendy and my daughter Eliška. They bring the endless love and care into my life and have always been supportive and patient with me. My big family as a whole deserves my never-ending gratitude, I can not name them all alongside with my friends, it would take a page.

During my doctoral study I have met many people who I now consider friends and who positively influenced my work and my life. The times at CERN were enjoyable thanks to the whole n_TOF collaboration, I feel the need to name a few people – thanks Daniela, Federica, Carlos, Frank and Toby. Coming to Los Alamos and getting data from there was an essential event of my PhD, I am in debt to all the people that run DANCE. The hospitality, the explanations and getting a bunch of remarks and questions about a draft were very helpful as well, thanks for that Aaron, Bayar, John and Marián. The gadolinium article would not exist without Ivo, who also took me to see the reactor at Řež and whom I shared the roadtrip to Grenoble with.

Our institute is truly a great place to work at. From all the friends that I have met here I wish to mention Dan and Pavel, who were always there to help me with statistics and software, Tomik and Martin, who showed me a perspective of big collaboration, Ingrid, who recently joined our little group, and Jiřík – we have shared the office, the problems of our analyses during our doctoral studies and much more and I hope we will continue doing so.

Last but not least I wish to express my deepest gratitude to my supervisor and my consultant, two of my friends, the most important people for my doctoral study itself. Milane, Františku, thank You!

Title: Study of statistical γ decay in well-deformed rare-earth nuclei

Author: Stanislav Valenta

Department: Institute of Particle and Nuclear Physics

Supervisor: Doc. Mgr. Milan Krtička, Ph.D., Institute of Particle and Nuclear Physics

Abstract: The γ decay of highly excited nuclear levels can be described within the statistical model of nucleus in terms of the level density and a set of photon strength functions. The knowledge of these quantities enables more accurate calculations of reaction rates in many different reactions which are important especially in nuclear astrophysics and in the development of advanced nuclear reactors. Despite the fact that the photon strength functions have been studied for decades, there are still contradicting experimental results regarding the low energy behavior of dipole strength. One of these cases is the shape of electric dipole photon strength function and the strength of the scissors mode in well-deformed rare-earth nuclei. In this thesis the analyses of γ-ray spectra measured by two different experimental setups are presented. The two-step γ cascades measurements with odd gadolinium targets were performed at the research reactor LVR-15 at the Research Centre Řež. In the multi-step γ cascades experiments the γ rays following resonance neutron capture on $^{161-163}$Dy targets were measured with the highly-segmented γ-ray calorimeter Detector for Advanced Neutron Capture Experiments in the Los Alamos Neutron Science Center at Los Alamos National Laboratory. Experimental spectra were compared to their simulated counterparts obtained by the Monte Carlo based code for simulation of radiative decay DICEBOX. The common result for all analysed isotopes is the clear influence of the scissors mode on the decay of excited levels, which persists quite high in the excitation energy. The preference of the Back Shifted Fermi Gas model of level density and the Modified Generalized Lorentzian model of electric dipole photon strength function is also a common feature. The models best describing present gadolinium data are in agreement with previously published multi-step γ cascades results on even-even Gd isotopes, confirming the consistency of two methods. The wealth and precision of the resonance experimental data on dysprosium isotopes enabled, for the first time, the analysis of fluctuations for a sizeable set of neutron resonances.

Keywords: Statistical Model of γ decay, Level Density, Photon Strength Functions, Scissors Mode, DICEBOX

Contents

Chapter 1

Introduction

After discovery of neutron by James Chadwick [1] the questions arrised about its interaction with matter. Chadwick himself immediatelly started to answer some of these questions [2], focusing on (n,α) reactions on light nuclei and on "neutron-proton collisions" – neutron-proton scattering.

A year later, the activation experiments using Po-Be neutron source were performed in the Physical Laboratory of the University of Rome. E. Fermi and colleagues observed the "Artificial Radioactivity produced by Neutron Bombardment" [3] – they measured the decays of β-radioactive isotopes produced in (n,α) and (n,p) reactions on very light and light isotopes and in some cases the decays of the isotopes produced by (n,γ) reaction on medium-heavy and heavy isotopes. The observation of (n,γ) reaction was proved by chemical analysis methods – some of the produced radioactive isotopes were of the same element as the target ones.

In succesive work [4] with neutrons slowed down by passing through paraffin, Fermi's team measured "surprisingly large values" of nuclear cross section for the activating impact of a *slow* neutron for boron, yttrium and cadmium. It was found that "no activation, or at least no strong activation, corresponds to an anomalously large absorption (B,Y,Cd). In these cases we might expect that the capture of the neutron leads to the formation of a stable nucleus. ... if the slow neutron is simply captured, we might expect that the absorption process should be accompanied by the emission of a γ-radiation, with energy corresponding to the binding energy of the neutron." They were able to measure this emission by altering their experimental setup, most importantly by including a lead-shielded Geiger Müller counter, see Fig. 1.1. A "very marked increase" of counts was observed when the counter was surrounded by the "strongly absorbing substances", in particular for yttrium and cadmium. The radiative capture of slow neutrons was measured.

There were, however, "some theoretical difficulties in understanding this capture process".

Shortly after Niels Bohr published, aiming to overcome said difficulties, two articles in Nature [5] and Science [6]. There he formulated, illustrated on mechanical model and compared – to then available experimental data – his idea of compound nuclear reactions.

According to Bohr the first step of the reaction is the relatively long formation of compound nucleus. He described [5] the key experimental result: "... the

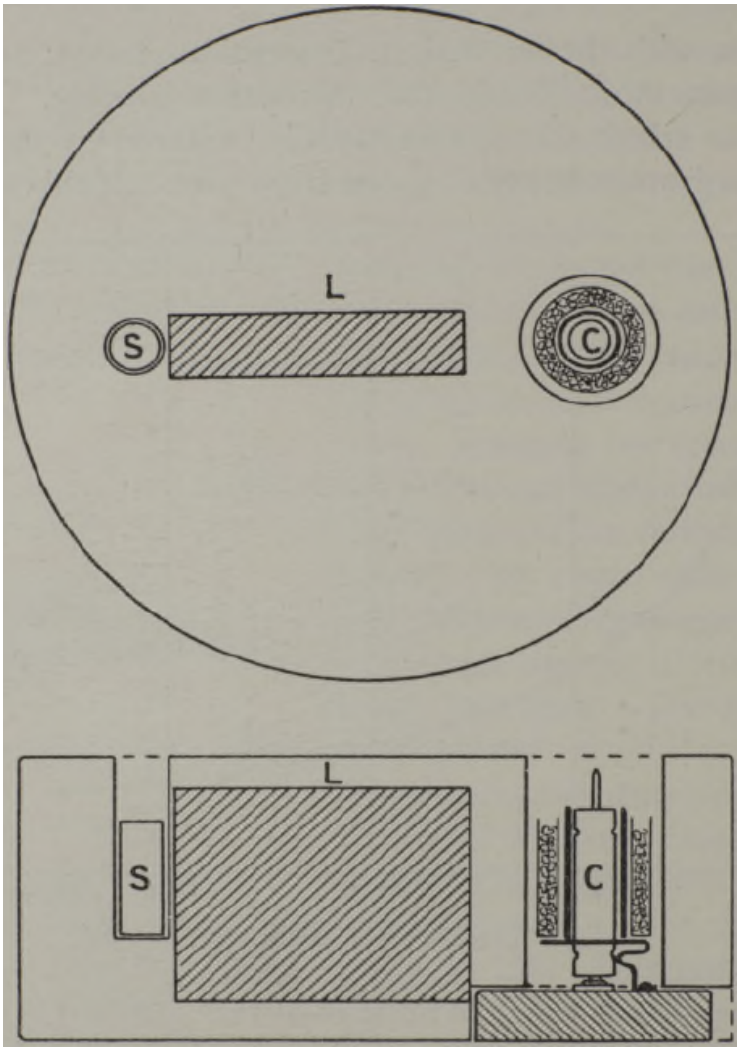

Figure 1.1: The schematic view of the experimental setup in the Physical Laboratory of the University of Rome. The Geiger Müller counter (C), surrounded by a layer of lead (in full black) and optionally by a layer of substance under study (shaded), is shielded by block of lead (L) from the Po-Be neutron source (S). The whole setup is enclosed by paraffin (empty). The figure is taken from Ref. [4].

surprisingly great tendency even for a fast neutron in collision with a heavy atom to attach itself to the nucleus with the emission of γ-radiation and the formation of a new isotope which may be stable or radioactive according to the circumstances. ... it is therefore clear that the duration of the encounter must be extremely long compared with the time interval, *circa* 10^{-21} sec., which the neutron would use in simply passing through a space region of nuclear dimensions." This "phenomena ... force us to assume ... the formation of a compound system of remarkable stability." In his mechanical model [6] Bohr compares the incident neutron to the billiard ball sent into shallow basin with a number of balls as illustrated in his famous sketch, see Fig. 1.2. As in the case of billiard balls' collisions, the excess energy (the neutron separation energy S_n and the kinetic energy of the incident neutron) "must in this state be assumed to be temporarily stored in some complicated motions of all the particles in the compound system, and its possible subsequent breaking up with the release of some elementary or complex

nuclear particle may from this point of view be regarded as a separate event not directly connected with the first stage of the collision process."

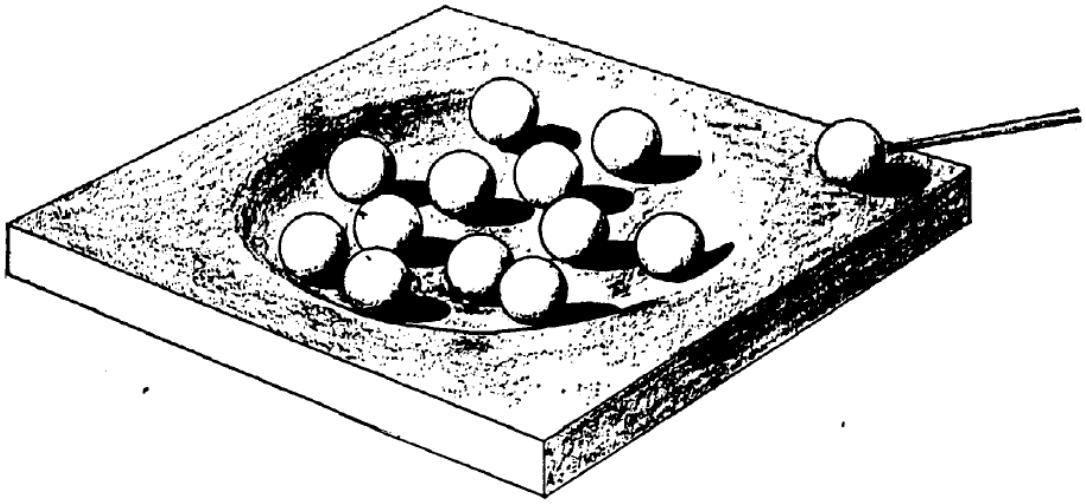

Figure 1.2: Bohr's mechanical analogy of formation of excited compound nucleus. The figure is taken from Ref. [6].

In regard to slow neutron capture, Bohr basically just described the experimental results - presence of "selective capture" [4] and the width of the resonances "as small as a fraction of a volt" [7]. He used this experimental information to supports his thoughts about the fast neutron interactions regarding the stability of the compound nucleus. In Science article [6] he mentions two works that derived the formula for the resonance cross section – the optical resonance analogy of Breit and Wigner [8] and the derivation of Bethe and Placzek [9] dealing more generally with the resonance effects in nuclear processes. Bohr then describes that the capture probability increases with respect to "neutron escape" with decreasing neutron energy and mentions that the thermodynamical analogies of evaporation (of a liquid or solid body at low temperature) fail to describe the capture reaction unlike the higher energy ones with neutron escaping in final state.

Bohr [6] also pointed out the essential difference between the level density ρ at low excitation energies (known experimentally from γ spectra after α decay), excitation energies just above neutron separation energy (known from very selective excitations by slow neutrons [10–12]) and by a few MeVs higher excitation energies (indicated from fast neutron reactions), see Fig. 1.3. How the level density increases with excitation was at that time calculated by Bethe [13, 14] and will be discussed in more details in Chapter 2.

The characteristic of three regions is as follows: the detailed knowledge of levels in close vicinity of the ground state is usually well determined experimentally and is a subject of the microscopical calculations. With increasing excitation energy, i.e. decreasing spacing between levels, the experiments lose the ability to resolve individual levels. Nevertheless, the spacing between the levels is still considerably higher than their natural width. This interval of excitation energy is usually refered to as the quasi-continuum. The continuum then refers to the domain of even higher excitation energies where the spacing drops so that it becomes comparable to the natural width of levels.

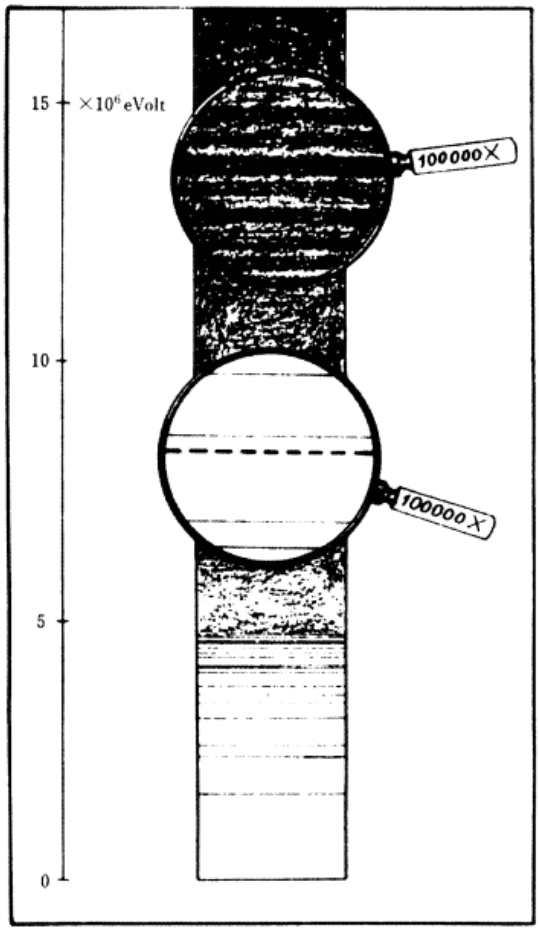

Figure 1.3: Bohr's illustration of "the general character of the distribution of energy levels for a heavy nucleus". The dashed line in the lower magnifying glass represents the neutron separation energy. The figure is taken from Ref. [6].

Inspired by this principial division, we adopt similar, but more practical approach, as will become aparent in Chapter 4. The boundary of the low energy region, denoted as the critical energy E_{crit}, is determined by the requirement of the completeness of the presently known decay scheme. Usually, the experiments can resolve levels to higher excitation energy than the critical energy, but fail to unambiguosly ascribe their spin and parity and to place the measured transitions in the level scheme. The levels above the critical energy up to the initial state of the decay are then believed to be described within the *Statistical Model* of nucleus.

The term Statistical Model was first used for the description of a nuclear reaction in terms of the decay of an equilibrium system of long lifetime in Refs. [15, 16]. Weisskopf and Ewing calculated the cross section and the decay of highly excited states, characterized by the neutron and radiative widths. The analogy to the evaporation formula was mentioned and the results were compared to it. They also compared their results on the radiative width to the ones of Bethe and Placzek [9].

Similar calculations were performed by Bethe [14], who examined also the character of γ rays related to nuclear processes – the reactions and the radioactive

decays. Bethe divided the γ rays into "two main classes", the first one being the "γ rays emitted during the nuclear process itself", i.e. the primary γ rays, and the second one the "γ rays emitted in a secondary process following the proper (primary) nuclear process". In his view the cascade deexcitation after neutron capture consists of one class 1 γ ray followed by emission of one or more class 2 γ rays. Using a simplyfing assumption about the nature of "dipole moment for transitions between any two states" and his result on the exponential decrease of the level spacing, Bethe calculated the distribution of primary γ rays from the slow neutron capture on a heavy nucleus, see Fig. 1.4. From the result that the primary γ ray most probably carries away a quarter to half of the available excitation energy, Bethe deduced that the secondary γ-radiation would usually be softer than the primary one and the number of γ rays emitted in the capture process, i.e. the multiplicity, would be on average between three and ten.

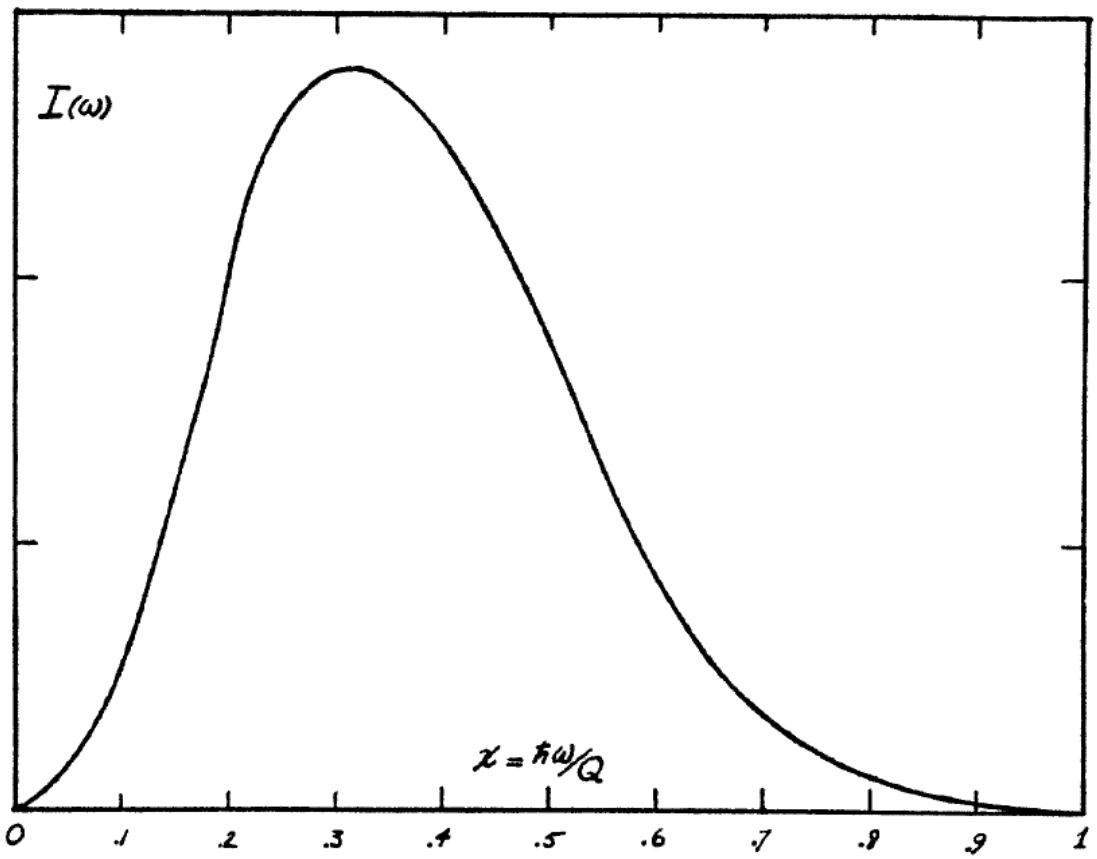

Figure 1.4: The distribution of primary γ rays from the slow neutron capture on a heavy nucleus as calculated by Bethe. The abscissa is the ratio of the γ-ray energy to the neutron separation energy and the ordinate is the relative intensity. The figure is taken from Ref. [14].

A simplyfing assumption similar to Bethe's was introduced by Ericson in 1960 [17] as the basis of the Statistical Model: "It might however be expected that the matrix elements have randomly distributed phases due to the randomized nature of the Compound Nucleus." Ericson calculated the spectrum of "evaporated γ rays" within the evaporation approximation which is quite similar to the estimation of Bethe [14].

By that time it was well known that the electric-dipole ($E1$) transitions play a dominant role in the decay of compound nuclei at excitations above the neutron separation energy due to the presence of the Giant Electric Dipole Resonance (GEDR). The GEDR was discovered by measuring photoabsorption cross section above neutron separation energy by Baldwin and Kleiber [18]. Few years earlier Migdal [19] predicted the GEDR as a consequence of collective dipole vibrations of proton and neutron fluids.

In 1959 Lane and Lynn [20] exploited the experimentally determined characteristic shape of the photoabsorption cross section σ_γ given by the presence of the GEDR in their calculation of capture cross section. They defined the *Photon Strength Function* (PSF) $S(E_\gamma)$ by its relation to the photoabsorption cross section $\sigma_\gamma \propto E_\gamma S(E_\gamma)$. In their calculation they also assumed that the photoabsorption cross section for any excited state has the same properties as for the ground state – this assumption was originally proposed by Brink [21] and is now known as the *Brink hypothesis*.

In the work focused on the analysis of primary transitions [22] following the neutron capture, Bartholomew defined the PSF, which he called "radiation strength" or "reduced widths", as a ratio of partial radiative widths to the spacing D_0 of levels at neutron separation energy with the same spin and parity as the capturing state $S(E_\gamma) = \Gamma_\gamma(E_\gamma)/(E_\gamma^3\ D_0)$.

Within the notion of the PSF introduced by Bartholomew, one can calculate the primary γ-ray spectrum given the knowledge of the final states, the PSF $S(E_\gamma)$ and the spacing at separation energy D_0, i.e. the level density $\rho(S_n)$. The comparison to the experimental primary γ-ray spectrum for the wide range of γ-ray energies is complicated by the unavoidable detection of secondary transitions. Nevertheless, given the knowledge of the level density $\rho(E)$ at all excitation energies up to the neutron separation energy, we can calculate the secondary γ-ray spectrum for any intermediate level populated by the primary transition analogously to the calculation of the primary spectrum and repeat such calculation until the ground state is reached. Reversely, the analysis of the complete γ cascades – detected by coincident experimental setup – could reveal information about the LD and PSFs. The present state of the knowledge on PSFs in the rare-earth nuclei is described in Chapter 3. Such analysis is however complicated by the fluctuations of involved quantities. For this reason, a trial-and-error approach of comparing the observables simulated under different assumptions about the LD and PSFs to their experimental counterparts was adopted. The simulations of γ cascades are described in Chapter 4.

In order to fully register as many cascades of as many multiplicities as possible, we have to rely on highly efficient detector system with high solid angle coverage like the Detector for Advanced Neutron Capture Experiments (DANCE) in the Los Alamos Neutron Science Center at Los Alamos National Laboratory, which was used to measure the so-called multi-step γ cascades (MSC) spectra from radiative capture of resonance neutrons. Alternatively, we can focus on specific subset of γ cascades exploiting the advantages of high resolution detectors such as the HPGe detectors. The pair of such detectors was dedicated to measure two-step γ cascades (TSC) following radiative capture of thermal neutrons. The TSC experimental setup was installed at the research reactor LVR-15 of the Research Centre Řež and the measurements were performed in collaboration with

colleagues from the Nuclear Physics Institute of Czech Academy of Sciences. The description of both experimental setups is given in Chapter 5.

As mentioned above, the information on LD and PSFs was obtained by a trial-and-error approach of comparing the simulated observables to their experimental counterparts. The results of the TSC and MSC analyses with emphasis on the MSC measurement of ^{162}Dy(n,γ) reaction are presented in Chapter 6. The results of TSC measurement of ^{155,157}Gd(n,γ) reactions were published and are attached in App. A and the MSC analysis of ^{161,163}Dy(n,γ) reactions was published and is attached in App. B. The conclusions and outlook are given in Chapter 7.

Chapter 2

Level Density

Level density (LD) is one of the basic statistical properties of excited nucleus. In our approach the decay of highly excited level is considered to be described by the statistical model of nucleus[1]. Hence the LD is one of the quantities needed for our modeling of γ decay.

2.1 Early Considerations

The formula for LD was derived by Bethe [13] in statistical approach. The complete information on the spectrum of a system is equivalent to the knowledge of the partition function of the system. For a gas of noninteracting fermions Bethe obtained LD ρ

$$\rho(E) = \frac{1}{4\sqrt{3}} \frac{\exp\left(2\sqrt{aE}\right)}{E} \tag{2.1}$$

at excitation energy E with a being the so-called level density parameter. For two-component gas of noninteracting fermions the formula reads

$$\rho(E) = \frac{1}{4\sqrt{3}} \sqrt{\frac{\pi}{3a^{1/2}}} \frac{\exp\left(2\sqrt{aE}\right)}{E^{5/4}}. \tag{2.2}$$

In his successive review [14] Bethe derives the level density $\rho(E, J)$ of levels with given spin J

$$\rho(E, J) = \rho(E, 0) \times \frac{J + \frac{1}{2}}{c\tau} \exp\left(\frac{-\left(J + \frac{1}{2}\right)^2}{2c\tau}\right), \tag{2.3}$$

where τ is the nuclear temperature, c is a constant coefficient (for given nucleus) and $\rho(E, 0)$ is proportional to $\rho(E)$ in Eq. (2.2).

Driven by then available data on spacing of "slow neutron resonances" D_0 Newton discussed [23] the influence of shell effects on level densities with emphasis on higher energies. He presented a formula for ρ with a dependence

[1]Practically, decay of any level above certain excitation energy E_{crit} is considered statistical in our simulations. For experimentally well-known levels above E_{crit} we could, in principle, determine if their decay is consistent with predictions of statistical model. Such study was not performed, mainly due to the fact that current version of our simulations does not allow to add extra levels with defined decay above E_{crit} to the levels randomly generated from LD.

$\sim 1/(2E + 3T)^2$, where T is the nuclear temperature, with no changes to the $\exp\left(2\sqrt{aE}\right)$ term, however his derivation was later shown incorrect by Gilbert and Cameron [24].

Noticing that if a sub-shell in the shell model has a degeneracy and is filled by k particles, these can be rearranged in $n!/k!(n-k)!$ different, degenerate configurations at zero excitation energy, Rosenzweig [25] derived a correction to the excitation energy E. An effective energy E' replaces excitation energy E in Eq. (2.2) with correction depending on mean spacings between states and the degeneracies of the last-filled neutron and proton shells. This correction decreases with excitation energy.

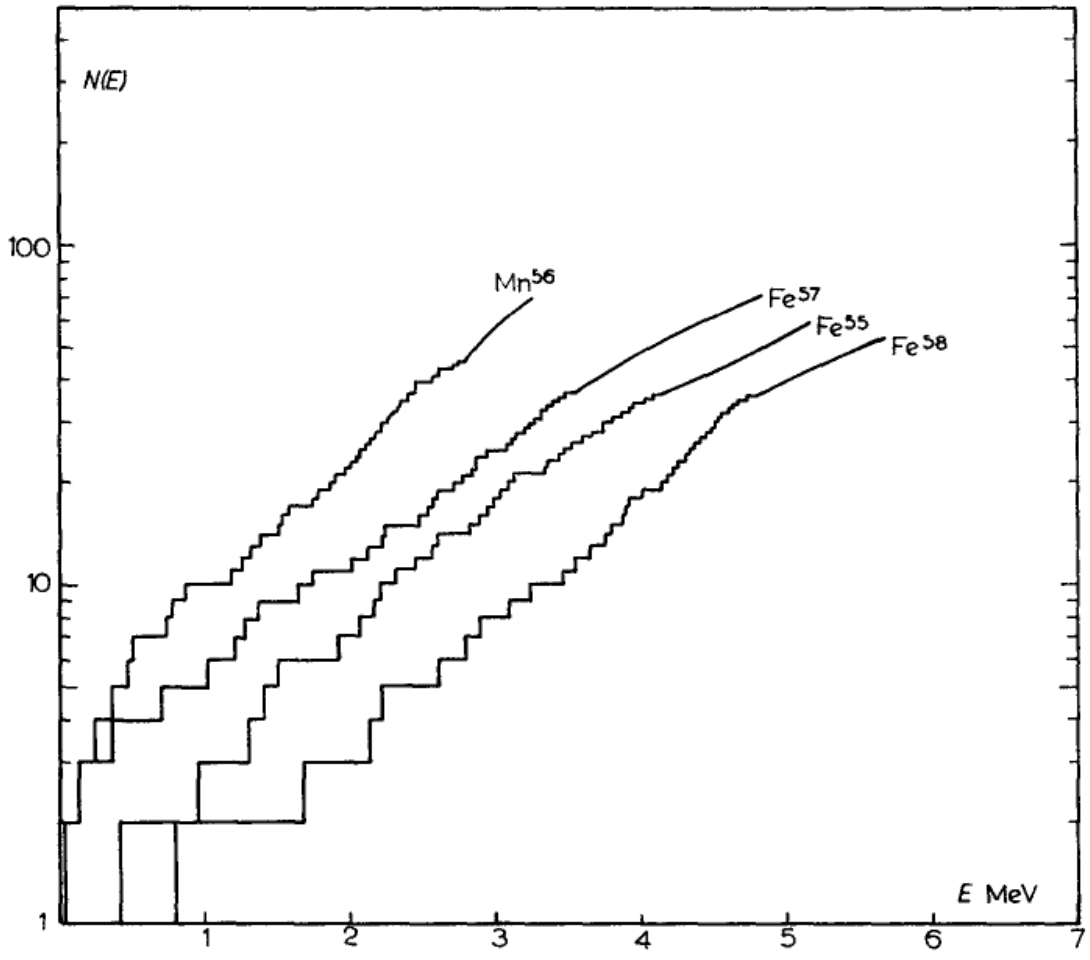

Figure 2.1: The measured total number of levels for isotopes in iron region as presented in Ref. [26]. ^{58}Fe is an even-even isotope, ^{55,57}Fe are odd (in neutrons) and ^{56}Mn is an odd-odd isotope. We remind that the presented quantity is the number of levels $N(E)$.

These two attempts were motivated by the experimental fact that taking E simply as an excitation energy does not work when looking at LD of neighbouring odd-odd, odd and even-even nuclei. This was pointed out in several works – first time by Newton [23], perhaps most convincingly by Ericson with data on number of levels for isotopes in iron region [26], see Fig. 2.1. Newton [23], besides the correction mentioned above, introduced the idea of subtracting a pairing energy from the excitation energy. While the existence of an energy gap in the nuclear

spectrum was shown before for few models [27, 28], the idea of replacing the excitation energy E in LD formula by effective energy with constant correction reflecting this energy gap was fully developed by Cameron [29] and later in his work with Gilbert [24]. In the later work the shell and pairing corrections were introduced based on semi-empirical mass formula of Cameron and Elkin [30]. To keep the right-hand side of LD formula as given in Eq. (2.2) the excitation energy E is replaced by the effective energy E' defined as

$$E' = E - P(N) - P(Z), \tag{2.4}$$

where the $P(\bullet)$ is the nucleon pairing energy – zero for odd values of N or Z and positive for even ones. Authors concluded that "there is no systematic difference left (in LD parameter a) due to odd-even effects. Thus the pairing energies have fulfilled their intended function".

The resulting, so-called *Back-Shifted Fermi Gas* (BSFG) formula is usually presented in the form

$$\rho(E) = \frac{\exp\left(2\sqrt{a(E-\Delta)}\right)}{12\sqrt{2}\sigma a^{1/4}(E-\Delta)^{5/4}}, \tag{2.5}$$

where Δ is an energy shift, in treatment of Gilbert and Cameron equal to $\Delta = P(N) + P(Z)$.

Gilbert and Cameron [24] proposed to use another formula to better describe the experimentally determined low-energy behavior of number of nuclear levels, e.g. data in Fig. 2.1. The systematic analysis of number of observed levels $N(E)$ throughout the nuclei chart (from Na isotopes to ^{245}Cm) showed that an exponentially increase according to formula $N(E) \sim \exp\left(\frac{E-E_0}{T}\right)$ provides good description, thus the LD is given as

$$\rho(E) = \frac{1}{T}\exp\left(\frac{E-E_0}{T}\right). \tag{2.6}$$

The two parameters E_0 and T in this so-called *Constant Temperature* (CT) formula were obtained for each studied isotope from fitting the $N(E)$ to the above-mentioned experimental data.

As their final result Gilbert and Cameron [24] proposed a composite formula, in which the CT formula is used up to certain excitation energy E_x and the BSFG formula is used above E_x, naturally the function is required to be continuous. They obtained the parameters of the composite formula for each studied isotope from fitting to then available experimental data on low-lying levels and D_0's. From the results on E_x the systematic formula was derived

$$E_x = 2.5 + 150/A + P(Z) + P(N)(\text{MeV}). \tag{2.7}$$

This formula is refered to as *Composite Gilbert-Cameron* (G-C) formula.

As can be seen from Eq. (2.3), the LD of levels with given spin J can be determined as a product of the total LD $\rho(E)$ and the spin distribution $f(J)$. Assuming the Gaussian distribution of spin projections M, Ericson [17] and Gilbert and Cameron [24] derived the $f(J)$ dependent on the so-called spin cut-off parameter σ. While Ericson used the $J(J+1)$ approximation in the exponential

term, Gilbert's and Cameron's formula was given in presently used form

$$f(J) = \exp\left(-\frac{J^2}{2\sigma^2}\right) - \exp\left(-\frac{(J+1)^2}{2\sigma^2}\right) \approx \frac{2J+1}{2\sigma^2}\exp\left(-\frac{(J+1/2)^2}{2\sigma^2}\right) \quad (2.8)$$

with the spin cut-off parameter given as

$$\sigma^2 = 0.0888A^{2/3}\sqrt{a(E-\Delta)}. \quad (2.9)$$

The question of parity was somewhat tackeled by Ericson [17] and by Gilbert and Cameron [24]. Using simple combination formula and well known properties of fermionic states they arrived at a conclusion that the LD of levels with both parities at high excitation energies should be practically the same.

2.2 Phenomenological Parametrizations

The LD formulae presented above – BSFG, CT and G-C formulae – are often used with parameters determined by fitting the experimental data, namely the spectroscopic information on low-lying levels and the spacings of s-wave neutron resonances.

In such phenomenological approach the LD is usually assumed to have a separable form

$$\rho(E, J, \pi) = \rho(E)f(J)g(\pi), \quad (2.10)$$

with the total LD $\rho(E)$, the spin distribution $f(J)$ and the parity distribution $g(\pi)$. For the sake of clarity we neglect other possible dependencies of distributions, they will be specified later in the text and corresponding equations. As an example, the spin distribution is usually a function of excitation energy E through the E-dependent σ, so we could write $f(J, \sigma)$, $f(J, \sigma(E))$ or $f(J, E)$.

2.2.1 Back-Shifted Fermi Gas Formula

Two most recent relevant sources of parametrizations are the compilations by von Egidy and Bucurescu [31, 32] and the results of RIPL project [33].

BSFG Formula with Energy Independent Parameters

In both papers von Egidy and Bucurescu use the BSFG formula for $\rho(E)$ as given in Eq. (2.5) with the spin distribution $f(J)$ in the standard form of Eq. (2.8). In the earlier work [31] the spin cut-off parameter is modified with respect to Eq. (2.9) to better account for the region of low excitations

$$\sigma^2 = 0.0146\frac{1+\sqrt{1+4a(E-\Delta)}}{2a}A^{5/3}, \quad (2.11)$$

while in the later work [32] the spin cut-off parameter resembles the A-dependence of Eq. (2.9), but omits the a-dependence and the coefficients and exponents are a result of a global fit of low-lying levels of 227 nuclei

$$\sigma^2 = 0.391A^{0.675}\left(E - 0.5Pa'\right)^{0.312}, \quad (2.12)$$

where Pa' is the deuteron pairing energy calculated from mass or mass excess values $M(A, Z)$ of the mass tables [34] as

$$Pa' = \frac{1}{2}\left[M(A+2, Z+1) - 2M(A, Z) + M(A-2, Z-1)\right]. \tag{2.13}$$

The parity distribution is neglected in both articles, assuming $g(+) = g(-) = \frac{1}{2}$ [31].

The parameters of LD, namely a and Δ, are considered free parameters in the above mentioned fit and are thus uniquely determined for each studied isotope. They are, together with Pa' in case of later parametrization, available in convinient tabulated form [31, 32]. The resulting total LD $\rho(E)$ is for ^{163}Dy shown in Fig. 2.2 and for ^{162}Dy Fig. 6 of App. B.

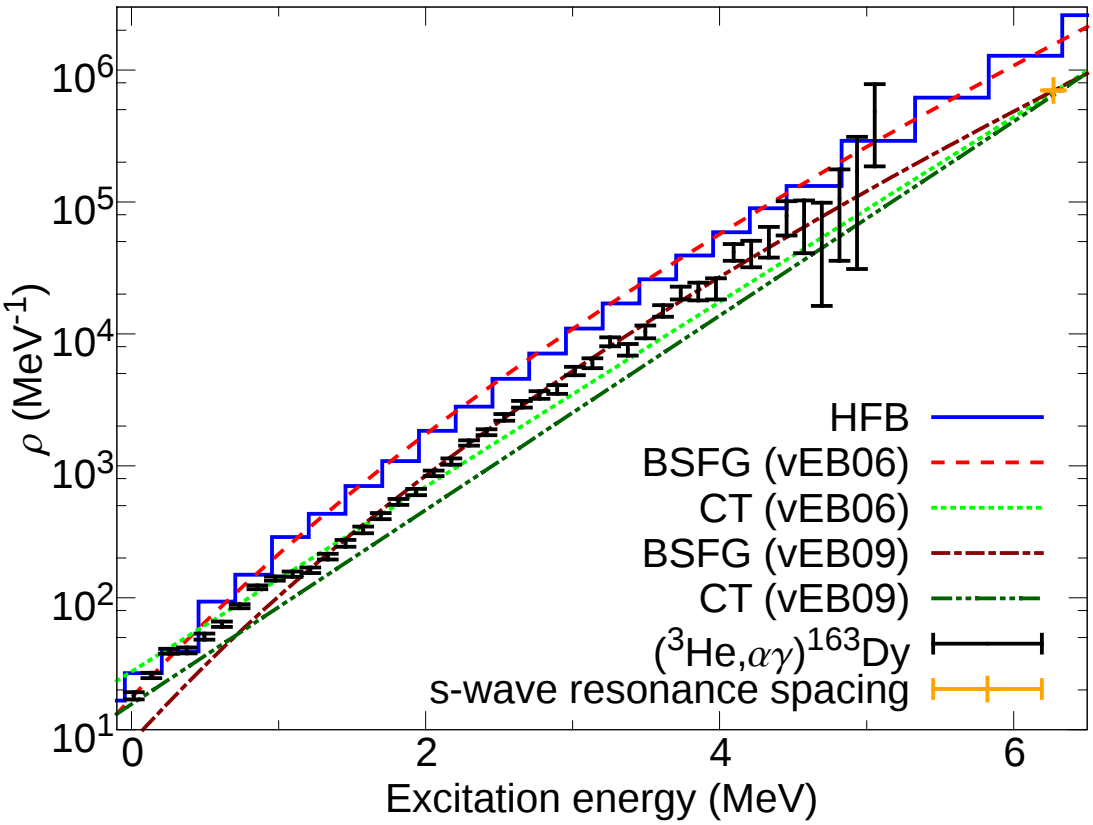

Figure 2.2: Spin- and parity-summed level density of ^{163}Dy according to the CT and BSFG formulae and the HFB calculations. The parameters of the CT and BSFG LDs were taken from Refs. [31] and [32], denoted as (vEB06) and (vEB09) respectively. The experimental data $\rho^{\text{Oslo}}(E)$ from the Oslo method [35] labeled (^{3}He,$\alpha\gamma$)^{163}Dy are also shown. Different predicted absolute values at S_n = 6.271 MeV originate from different spin distributions in the formulae. The point corresponding to the s-wave resonance spacing [36] was converted to the summed LD using the spin distribution with the spin-cutoff parameter from [32].

BSFG Formula with Energy Dependent Parameters

The presence of shell effects that vanish with excitation energy, as mentioned above [25], motivates the use of more complicated BSFG formulae. In particular,

following the phenomenological approach [37], the damping of the shell effects is included in energy dependent LD parameter a

$$a(E) = \tilde{a}\left\{1 + \frac{\delta W}{E-\Delta}\left[1 - e^{-\gamma(E-\Delta)}\right]\right\}, \tag{2.14}$$

where δW is a shell correction energy, γ is the damping parameter, $\tilde{a}$ is the asymptotic level density parameter and Δ the energy shift. Parameters $\tilde{a}$ and Δ are fitted for individual isotopes.

In case of parametrization by von Egidy and Bucurescu [31] the LD formula is obtained by substituting a in Eqs. (2.5) and (2.11) by $a(E)$ of Eq. (2.14). The distributions $f(J)$ and $g(\pi)$ remain in the same form with respect to BSFG formula with energy independent parameters, see Sec. 2.2.1. The damping parameter $\gamma = 0.06$ MeV^{-1} comes from a global fit, the shell correction energy δW reflects the difference between the experimental mass and the mass given by liquid drop formula corrected for the pairing energy, the individual values are tabulated [31].

Within the RIPL project [33] more complicated formula for $\rho(E)$ with respect to Eq. (2.5) was used with the LD parameter $a(E)$ given by Eq. (2.14). The parameters δW and γ are determined in a similar way to Ref. [31] with a difference of A-dependent γ. The values for individual isotopes are tabulated [38]. The distributions $f(J)$ and $g(\pi)$ are unchanged with respect to BSFG formula of Sec. 2.2.1. The spin cut-off parameter σ is given as a linear combination of a high energy (for $E \geq S_n$) limit

$$\sigma_F^2 = 0.01389\frac{A^{5/3}}{\tilde{a}}\sqrt{a(E-\Delta)} \tag{2.15}$$

with low energy behavior – the so-called discrete spin cut-off parameter σ_d determined from the experimental information on low-lying levels or from the global systematics

$$\sigma_d = 0.83A^{0.26}. \tag{2.16}$$

For futher details see Ref. [33].

2.2.2 Constant Temperature Formula

Despite its original purpose described above, the CT formula Eq. (2.6) is frequently used for the description of the total level density up to excitation energies as high as neutron separation energy. As in the case of BSFG formula, von Egidy and Bucurescu [31, 32] used the available experimental data to fit the formula and determine the parameters T and E_0 for number of isotopes. The spin distribution $f(J)$ was taken in the standard form of Eq. (2.8), the parity distribution was neglected in both articles, assuming $g(+) = g(-) = \frac{1}{2}$ [31].

The spin cut-off parameter used in their earlier work [31] was taken independent on excitation energy in simple form determined before [39]

$$\sigma = 0.98A^{0.29}. \tag{2.17}$$

The later version [32] uses the same formula for σ as is used for the BSFG formula, see Eq. (2.12).

The total LD given by these two parametrizations is for ^{163}Dy shown in Fig. 2.2 and for ^{162}Dy in Fig. 6 of App. B.

2.2.3 Gilbert-Cameron Formula

The composite G-C formula uses the CT formula Eq. (2.6) up to certain excitation energy E_x and BSFG formula Eq. (2.5) above E_x as described in Sec. 2.1. The spin and parity distributions are usually given by the standard form of Eq. (2.8) and $g(+) = g(-) = \frac{1}{2}$, respectively.

Following the derivation in Ref. [24] the spin cut-off parameter is expressed as

$$\sigma^2 = kA^{2/3}\sqrt{a(E-\Delta)}. \tag{2.18}$$

The constant k was proposed to be $k = 0.0888$ in [24], later parametrization [40] suggested $k = 0.1146$.

In the RIPL project [33] the G-C formula is used with BSFG formula, spin cut-off parameter and LD parameter as described above, see Sec. 2.2.1.

2.3 Microscopical Calculations

We restrict ourselves to describe only the calculations that we consider relevant, namely the calculations dealing directly with the rare-earth nuclei, the calculations of well-deformed nuclei showing features that are expected to occur in well-deformed rare-earth isotopes and the calculations revealing the features that were experimentally observed in many mass regions including the rare-earths.

Paar and coauthors [41] performed large-scale combinatorial calculations of level densities for selected well-deformed nuclei using Gaussian polynomial generating function method (GPM). Despite the fact that they did not choose a rare-earth isotope, their results showed common features for two distinct nuclear masses, one lighter and one heavier than rare-earths. The level density in their approach could be factorized into $\rho(E) \times f(J, E)$. The total LD $\rho(E)$ was well fitted by BSFG formula Eq. (2.5). Their results were described by a different form of $f(J)$ with respect to Eq. (2.8) with some energy dependent factors, for futher details see Sec. 2.4 and Ref. [41].

A microscopic combinatorial approach was used to calculate the state and level densities with fixed exciton numbers in some actinide nuclei by Garcia *et al.* [42]. The deformed Woods-Saxon shell model was used as a basis from which all possible configurations were generated. The pairing interaction was taken into account by applying the BCS theory to each configuration. Both the spin and parity distributions were obtained, considering the deformation of ^{239}U and ^{233}Th nuclei. The results were compared to the results of spherical case. Futher remarks about the spin and parity distributions are given in Sec. 2.4 and 2.5, respectively.

The authors in Refs. [43, 44] used Hartree-Fock-Bogoljubov (HFB) plus a combinatorial method to obtain the tabulated LD as a function of energy for levels with each spin and parity, hereafter denoted as HFB LD. These calculated level densities usually suffer from difficulties in reproducing the cumulative number of observed low-lying levels as well as the average neutron resonance spacing. In order to bring the calculations into agreement with experimental data, the HFB LD was suggested to be renormalized [43]. In our simulations we usually use the renormalized version in tabulated form. The spin- and parity- summed HFB LD is plotted in Fig. 2.2 for ^{163}Dy and in Fig. 6 of App. B for ^{162}Dy. The energy dependence of the spin- and parity- summed HFB LD is in both cases rather

close to the BSFG formula with parameters from Ref. [31]. The details about the distributions of spins and parities are discussed in Sec. 2.4 and 2.5, respectively.

The LD of variety of nuclei was calculated within the shell model Monte Carlo (SMMC) approach, recently including the well-deformed rare-earth isotopes. The initial work on ^{162}Dy [45] showed the feasibility of such calculations and was followed by studies of Nd and Sm isotopical chains that exhibit a transition from spherical to well-deformed isotopes [46–48]. The energy dependence of LD $\rho(E)$ from SMMC calculations did not show significant deviation from the BSFG formula in any studied rare-earth isotope. In particular, the SMMC LD of ^{162}Dy [45] is compatible with the BSFG formula with parameters from [32] between $E_{\rm crit}$ and S_n. The results of SMMC calculations on spin and parity distributions are presented in Secs. 2.4 and 2.5, respectively.

2.4 Spin Distribution

As already mentioned in Sec. 2.3, a systematic deviation from theoretical spin distribution formula given in Eq. (2.8) was calculated within GPM [41]. Nevertheless, the formula describing their results falls between the spin distributions of two BSFG parametrizations of von Egidy and Bucurescu [31, 32] presented in Sec. 2.2.1. The $f(J)$ results from Ref. [42] showcase the difference between deformed and spherical actinide nuclei. There is no reason to doubt that the spin distribution at all relevant excitation energies can be described using Eq. (2.8) with properly adjusted, energy dependent σ.

In case of even-even isotopes the experimentally well established deviation from Eq. (2.8) at low excitation energies, in particular the high abundance of $J = 0$ levels and the preference of even spins with respect to odd spins, prompted both phenomenological studies and theoretical calculations.

This so-called even-odd spin staggering effect in the spin distribution was explicitly shown in SMMC calculation of ^{56}Fe [49] and later in the extension of the ^{162}Dy calculation [45]. Kaneko and Schiller published results on LD of ^{56}Fe from a thermal and quantum-mechanical treatment of nuclear rotation using the formalism of static path approximation (SPA) plus random-phase approximation (RPA) [50]. Their calculation clearly showed an enhanced abundance of $J = 0$ levels at low excitation energies as well as the transformation to the standard spin distribution given by Eq. (2.8) with increasing excitation energy. The HFB LD calculations [43,44] of even-even rare-earth isotopes exhibit a persisting even-odd spin staggering at practically all excitation energies below S_n, see example of ^{162}Dy result in Fig. 2.3.

The effect of even-odd spin staggering was pointed out in the survey of 310 nuclei by von Egidy and Bucurescu [51]. The enhancement factors of $J = 0$ and even J levels with respect to Eq. (2.8) were obtained from a global fit. In the later paper [32] the spin-cutoff parameter was determined as given in Eq. (2.12) and the spin distribution of the even-even nuclei at low excitation energies was modified using the so-called staggering parameter x

$$f_{\rm ee}(J) = f(J)(1 + x), \tag{2.19}$$

where $x = 0.227$ for even spin, $x = -0.227$ for odd spin and $x = 1.02$ for the zero spin. Authors did not mention the excitation energy dependence of x. The

SMMC calculation [45] showed that for ^{162}Dy the spin distribution is compatible with Eq. (2.19) using parameters from Ref. [32] if the staggering parameter x decreases linearly with excitation energy and reaches zero at $E = 4$ MeV. The spin distribution following these conclusions is plotted in Fig. 2.3.

It is worth pointing out that the width of the spin distribution and the persistence of even-odd spin staggering with excitation energy drastically differs between SMMC and HFB calculations.

2.5 Parity Distribution

As described in Sec. 2.2, the parametrizations of both BSFG and CTF formulae work with the assumption of parity independence of level density. However, the parity dependence cannot be a priori excluded – extending the above mentioned idea [17, 24] Cerf [52] and Pichon [53] showed the characteristic behavior for the model in idealized case and in number of $A \sim 50$ isotopes, respectively. One can argue that the observed parity asymmetry would be negligible above a few MeV's of excitation energy in heavier spherical nuclei. Futhermore this asymmetry is supposed to vanish more quickly with a deformation of nuclei. Garcia and coauthors [42] calculated, for ^{239}U and ^{233}Th, that the oscillation is at most 2% (around 1/2) and slowly decreases with excitation energy.

The phenomenological formula

$$g(+) = 1 - g(-) = \frac{1}{2}\left(1 \pm \frac{1}{1 + \exp\left[c_p(E - \delta_p)\right]}\right), \tag{2.20}$$

where + or − is chosen in accordance with the dominant spin of low-lying levels, was used to describe the experimental data for nuclei $20 \leq A \leq 110$ in Ref. [54]. Authors performed a global fit that yielded $c_p = 3$ MeV^{-1} and different δ_p formulae for even-even, odd-even, even-odd and odd-odd nuclei. While the rare-earth isotopes studied in the present work ($A \sim 160$) are significantly heavier, we employ the formula of Eq. (2.20) in some of our simulations. Futhermore we also test the values of parameters coming from the systematics proposed by Al-Quraishi and coauthors, i.e. $c_p = 3$ MeV^{-1} with, for example, $\delta_p = 2.15$ and 0.73 MeV for ^{162}Dy and ^{163}Dy, respectively.

One of the results of SMMC calculation [45] was that the parity symmetry is restored at ≈ 3 MeV and the parity distribution could be described using the formula of Eq.(2.20). Considering the experimental data on low-lying levels we use the parameters $c_p = 3$ MeV^{-1} and $\delta_p = 1.5$ MeV to describe the SMMC result on parity distribution in ^{162}Dy.

The HFB LD [43, 44] showed the expected exclusivity of positive parity levels at very low excitation energies in even-even isotopes. Above certain excitation energy in even-even isotopes and from zero excitation energy in other isotopes an oscillation, similar to results in Ref. [42], was observed with much bigger amplitude (up to 50%) but disappearing much faster – the parity symmetry (within few percent) is restored at ~ 4 MeV and ~ 3 MeV in ^{162}Dy and ^{163}Dy, respectively.

2.6 Experimental Determinations of Level Density

The pointwise LD can be extracted in the energy range used in our analyses ($E_{\rm crit}$–S_n) from the experimental data within two methods.

The first kind of LD determination is based on the measurements of shapes of neutron evaporation spectra in various reactions, e.g. (p,n), (d,n), (α,n), ... The reaction cross sections for number of isotopes including rare-earth ones were analysed within the Hauser-Feshbach statistical approach and the LDs were found to reasonably agree with the BSFG formula [55, 56]. Some nuclei in the vicinity of closed shells with $A \approx 208$ display a CT-like LD [57].

The second source of pointwise LD and PSF is the so-called Oslo method [58]. The γ rays are measured in reactions induced by charged particles – typically by ^{3}He, recently also by protons and deuterons. The initial excitation of compound nucleus $E_{\rm ini}$ is determined by measuring the energy of outgoing charged particle using the $\Delta E - E$ silicon telescope. The γ-ray spectra are recorded by the array of NaI detectors and analysed in coincidence with the charged particles. After unfolding of the detector response [59], the so-called first generation matrix, i.e. the primary γ-ray spectra for each bin of accessible excitations $E_{\rm ini}$, are calculated by sequential substraction of the unfolded γ-ray spectra. The Oslo results – LD $\rho^{\rm Oslo}(E)$ and PSF $S^{\rm Oslo}(E_\gamma)$ – are a result of a fit of the first generation matrix.

The possible systematic errors of the Oslo method were thoroughly discussed in a dedicated article [60]. From the perspective of a comparison with our results, it is important to point out that the fitting procedure of the Oslo method relies on some assumptions and has an infinite number of solutions which can be obtained from any particular solution by a transformation

$$\tilde{\rho}^{\rm Oslo}(E_{\rm ini} - E_\gamma) = A \exp\left[\alpha(E_{\rm ini} - E_\gamma)\right] \rho^{\rm Oslo}(E_{\rm ini} - E_\gamma), \tag{2.21}$$

$$\tilde{S}^{\rm Oslo}(E_\gamma) = B \exp\left(\alpha E_\gamma\right) S^{\rm Oslo}(E_\gamma), \tag{2.22}$$

where the argument of LD is written in the form of $(E_{\rm ini} - E_\gamma)$ to emphasize the way it is calculated. To normalize the Oslo results, the constants A, B and α have to be fixed using external data on low-lying levels, s-wave neutron resonance spacing and average radiative width of s-wave neutron resonances. We will restrict the discussion to the favourable case when all three types of the external data are available from reliable sources.

One of the assumptions of the Oslo method is that the PSF is E-independent, i.e. follows the Brink hypothesis [21]. In principle one could fit the rows of the first generation matrix with the condition of a common LD $\rho^{\rm Oslo}(E)$, which would in general result in E-dependent PSF $S^{\rm Oslo}(E_\gamma)$. However, for practical reasons the $\rho^{\rm Oslo}(E)$ and $S^{\rm Oslo}(E_\gamma)$ are, as already mentioned, a result of a fit of the first generation matrix as a whole, which requires the use of Brink hypothesis.

The $\rho^{\rm Oslo}(E)$ and $S^{\rm Oslo}(E_\gamma)$ are not determined on the full energy interval that is in principle accessible, i.e. $(0, S_n)$, as can be seen in Fig. 2.2. This fact implies that the normalization requires an analytic continuation of the Oslo results, which introduces some degree of model dependence. The s-wave neutron resonance spacing, which is used for the normalization of $\rho^{\rm Oslo}(E)$, is converted

to the total LD using the spin distribution with a certain spin-cutoff parameter[2] usually taken from one of Refs. [31, 61], which adds another source of model dependence. The normalization of $S^{\mathrm{Oslo}}(E_\gamma)$ relies also on its transformation to the average radiative width of s-wave neutron resonances. This includes a use of normalized $\rho^{\mathrm{Oslo}}(E)$, the assumption that only dipole transitions play a role in the decay and again the use of the spin distribution with certain spin-cutoff parameter. The specifics of decomposition to the individual components of PSFs, e.g. scissors mode or pygmy resonances, are discussed later in Sec. 3.4.2, the comparison of our results with the Oslo results in Sec. 6.3.3.

The convenient circumstance for the comparison of our results with the Oslo results is that $^{160-164}$Dy were analysed within the Oslo method [35, 62, 63]. The $\rho^{\mathrm{Oslo}}(E)$ of ^{163}Dy [35] is shown in Fig. 2.2. The Oslo result for ^{162}Dy [63] is shown in Fig. 6 of App. B.

[2]If we used the BSFG formula's spin-cutoff parameter of Eq. (2.11) from Ref. [31] for the conversion of the s-wave neutron resonance spacing, the orange datapoint would fall on the BSFG (vEB06) curve in the Fig. 2.2. The difference between the two BSFG curves in the figure at S_n indicates a magnitude of one of the uncertainties in the normalization of the Oslo results.

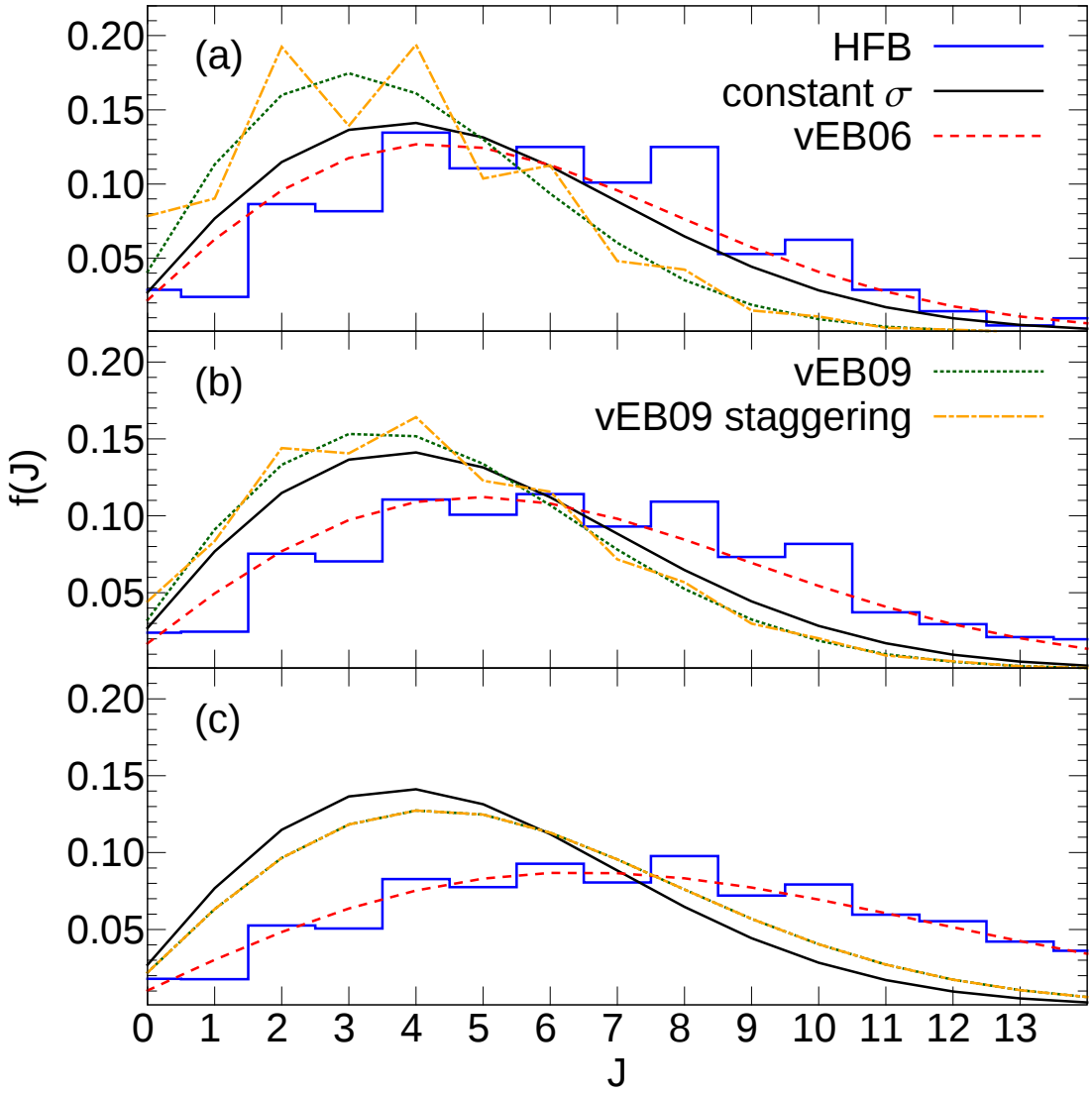

Figure 2.3: Spin distribution $f(J)$ of ^{162}Dy as obtained from result of HFB calculation [43, 44] and as given by different LD parametrizations. The panels (a), (b) and (c) show the spin distributions at excitation energies of 1.87, 3.0 and 8.2 MeV. These energies correspond to the critical energy E_{crit} used in our simulations, see Sec. 5.2.3, the energy where the parity symmetry of LD is restored according to SMMC calculation [45], see Sec. 2.5, and to the neutron separation energy, respectively. The curve labeled constant σ uses the spin cut-off parameter of Eq. (2.17) from Ref. [39], the resulting $f(J)$ is used with CT formula with parameters from Ref. [31]. The curve labeled vEB06 corresponds to the spin cut-off parameter of Eq. (2.11) and the parameters of BSFG formula from Ref. [31]. The curve labeled vEB09 employs the spin cut-off parameter of Eq. (2.12), which is common for the BSFG and CT formulae when the parameters are taken from Ref. [32]. To illustrate the effect of even-odd staggering, as defined in Eq. (2.19), the curve labeled vEB09 staggering is plotted. The effect decreases linearly with increasing excitation energy and vanishes at $\approx$ 4 MeV in accordance with the SMMC result [45], see Sec. 2.4, so the distribution is identical to the vEB09 distribution in panel (c).

Chapter 3

Photon Strength Functions

Two possible introductions of photon strength function were mentioned in Chapter 1. In accord with Lane and Lynn [20] the $(X\lambda)$ PSF relates to the $(X\lambda)$ component of the photoabsorption cross section $\sigma_\gamma^{(X\lambda)}$

$$S^{(X\lambda)}(E_\gamma) = \frac{1}{(\pi\hbar c)^2}\frac{\overline{\sigma}_\gamma^{(X\lambda)}(E_\gamma)}{(2\lambda+1)E_\gamma^{2\lambda-1}}, \tag{3.1}$$

for a transition of type X ($E \equiv$ electric or $M \equiv$ magnetic) and multipolarity λ. The PSF is introduced as an average quantity, hence we use the energy smoothed photoabsorption cross section $\overline{\sigma}_\gamma^{(X\lambda)}(E_\gamma)$, as Lane and Lynn naturally did for the case of GEDR.

Bartholomew defined the PSF using the partial radiative width of neutron capturing state [22]. In this spirit the PSF as an average quantity can be defined as

$$S^{(X\lambda)}(E_\gamma) = \frac{\overline{\Gamma}_{i\gamma f}^{(X\lambda)}(E_\gamma)\rho(E_i, J_i, \pi_i)}{E_\gamma^{2\lambda+1}}, \tag{3.2}$$

where $\overline{\Gamma}_{i\gamma f}^{(X\lambda)}(E_\gamma)$ stands for an average partial radiative width of transitions with energy $E_\gamma = E_i - E_f$ of type X and multipolarity λ from any initial level i of spin J_i and parity π_i in the vicinity of the excitation energy E_i to any accessible final level f with excitation energy E_f, spin J_f and parity π_f. The accessibility of final levels is determined by the selection rules for electromagnetic transitions, which for initial and final spins J_i and J_f and multipolarity of the transition λ reads

$$|J_f - J_i| \leq \lambda \leq |J_f + J_i|\,, \tag{3.3}$$

while the parities of the initial and final levels π_i and π_f satisfy the identity

$$\pi_i\pi_f = (-1)^\lambda \tag{3.4}$$

for electric transitions of multipolarity λ and

$$\pi_i\pi_f = (-1)^{\lambda+1} \tag{3.5}$$

for magnetic transitions of multipolarity λ.

For a particular transition between two given levels τ and τ' with $E_\gamma = E_\tau - E_{\tau'}$ the detailed-balance principle relates the partial radiative width $\Gamma^{(X\lambda)}_{\tau\gamma\tau'}$ and the $(X\lambda)$ component of the photoabsorption cross section $\sigma^{(X\lambda)}_{\tau'\gamma\tau}$ as

$$\Gamma^{(X\lambda)}_{\tau\gamma\tau'} = \frac{E_\gamma^2}{(\pi\hbar c)^2}\frac{2J_{\tau'}+1}{2J_\tau+1}\sigma^{(X\lambda)}_{\tau'\gamma\tau}. \tag{3.6}$$

Let us now average the partial radiative widths $\Gamma^{(X\lambda)}_{\tau\gamma f}$ of transitions to level f from levels τ in the ϵ vicinity of excitation energy E_i. The number of initial levels is $\epsilon\rho(E_i, J_i, \pi_i)$. Consider also that the photoabsorption cross section for transitions from level f to all accessible levels (not just those with spin J_i and parity π_i) in ϵ vicinity of excitation energy E_i is averaged over the interval ϵ. The detailed-balance relation Eq. (3.6) can be then written as

$$\overline{\Gamma}^{(X\lambda)}_{i\gamma f}(E_\gamma)\rho(E_i, J_i, \pi_i) = \frac{E_\gamma^2}{(\pi\hbar c)^2}\frac{1}{2\lambda+1}\overline{\sigma}^{(X\lambda)}_{\gamma, f\to E_i}(E_\gamma), \tag{3.7}$$

showing that two definitions of PSF in Eqs. (3.1) and (3.2) are identical.

The phenomenological approach of deriving the PSF from the fit of the photoabsorption cross section or the partial radiative widths does not reveal the relation of the PSF to the properties of individual nuclear levels and transitions between them. The photoabsorption cross section $\sigma^{(X\lambda)}_{\tau'\gamma\tau}$ can be also expressed as

$$\sigma^{(X\lambda)}_{\tau'\gamma\tau} = \frac{8\pi^3 c^2\hbar^2\alpha_{\mathrm{FS}}}{E_\gamma e^2}\frac{k^{2\lambda}}{[(2\lambda+1)!!]^2}\frac{\lambda+1}{\lambda}B(X\lambda, \tau'\to\tau), \tag{3.8}$$

where the reduced transition probability $B(X\lambda, \tau'\to\tau)$ for the transition of type X and multipolarity L with the energy E_γ is defined as

$$B(X\lambda, \tau'\to\tau) = \frac{1}{2J_{\tau'}+1}\left|\left\langle\tau\,||\,\hat{\mathcal{M}}^{(X\lambda)}\,||\,\tau'\right\rangle\right|^2. \tag{3.9}$$

The operators $\hat{\mathcal{M}}^{(X\lambda)}$ are the transition operators of type X (electric or magnetic) and multipolarity λ. From the reduced transition probabilities to the levels τ with energy E_τ in the ϵ vicinity of excitation energy E_i we can define the photon strength function $\mathcal{S}^{(X\lambda)}$ as

$$\mathcal{S}^{(X\lambda)}(\tau'\to E_i) = \rho(E_i, J_i, \pi_i)\,\overline{B}(X\lambda, \tau'\to E_i) = \frac{1}{\epsilon}\sum_{E_\tau\in\epsilon} B(X\lambda; \tau'\to\tau). \tag{3.10}$$

Calculating the average photoabsorption cross section from Eqs. (3.8) and (3.10), we can obtain the relation between $\mathcal{S}^{(X\lambda)}$ and the PSF $S^{(X\lambda)}$ defined in Eq. (3.1):

$$S^{(XL)}(E_\gamma) = \frac{8\pi\alpha_{\mathrm{FS}}}{e^2(\hbar c)^\lambda}\frac{\lambda+1}{\lambda[(2\lambda+1)!!]^2}\frac{2J_{\tau'}+1}{2J_\tau+1}\mathcal{S}^{(X\lambda)}(\tau'\to E_i). \tag{3.11}$$

3.1 Electric Dipole PSF

The phenomenological approach of deriving the PSF from the fit of the photoabsorption cross section in the region of GEDR gave raise to the so-called *Standard*

Lorentzian (SLO) model of $E1$ PSF

$$S^{(E1)}_{\mathrm{SLO}}(E_\gamma) = \frac{1}{3(\pi\hbar c)^2}\sigma_G\Gamma_G\frac{E_\gamma\Gamma_G}{\left(E_\gamma^2 - E_G^2\right)^2 + E_\gamma^2\Gamma_G^2}, \tag{3.12}$$

where E_G, Γ_G, σ_G are the energy, width and cross section at the maximum of the resonance, respectively. An example of such fit is shown in Fig. 3.1, the expected necessity of using sum of two terms in deformed nuclei is illustrated. In this thesis we are dealing with well-deformed rare-earth nuclei, so the PSF describing the GEDR is always the sum of two terms with sets of parameters $\{E_{Gi}, \Gamma_{Gi}, \sigma_{Gi}\}_{i=1}^2$, for details see Sec. 6.2.3. For simplicity only one resonance term is assumed in equations for $S^{(E1)}$ in this section, so the sets of parameters $\{E_{Gi}, \Gamma_{Gi}, \sigma_{Gi}\}_{i=1}^2$ are replaced by a single set $\{E_G, \Gamma_G, \sigma_G\}$. In reality, the sum over two resonance terms is used in all models. The shape of the SLO model in the energy region below S_n is shown in Figs. 3.2, 3.4, 3 of App. A and 5 of App. B. The shape of dipole PSF given by the SLO model plus the composite $M1$ model is then shown in Figs. 3.3, 3.5 and 5 of App. B.

The SLO model well describes the $E1$ PSF near the peaks of GEDR, however its inadequacy at lower energies, i.e. below the neutron separation energies, was shown from compilations of (n,γ) data [64, 65] as well as from the measurement of ^{143}Nd(n,$\alpha\gamma$) reaction [66–68]. The energy dependent $E1$ PSF with a nonzero limit for $E_\gamma \to 0$ for levels with nonzero nuclear temperature T_f was observed together with T_f-dependent width Γ_G. The nuclear temperature of the final level f is usually considered in the form

$$T_f = \sqrt{\frac{E - \Delta}{a}}, \tag{3.13}$$

which corresponds to the temperature in the BSFG model. Here a and Δ are the level density parameter and the energy shift of Eq. (2.5).

Kadmenskii, Markushev and Furman [69] proposed a model for spherical nuclei with the above-described features using the semi-microscopic shell model together with Fermi-liquid theory of finite systems. The temperature-dependent width $\Gamma_G(E_\gamma, T_f)$ has a form

$$\Gamma_G(E_\gamma, T_f) = \frac{\Gamma_G}{E_G^2}\left(E_\gamma^2 + 4\pi^2 T_f^2\right), \tag{3.14}$$

and the so-called KMF model of $E1$ PSF reads

$$S^{(E1)}_{\mathrm{KMF}}(E_\gamma, T_f) = \frac{1}{3(\pi\hbar c)^2}F_K\sigma_G\Gamma_G\frac{E_G\Gamma_G(E_\gamma, T_f)}{\left(E_\gamma^2 - E_G^2\right)^2}. \tag{3.15}$$

It is evident that this model is not applicable near the peaks of GEDR. Despite the fact that this model was proposed for spherical nuclei, it is often used for deformed ones as well. The value $F_K = 0.7$ is adopted in the KMF model [33,69]. The shape of the KMF model in the energy region below S_n is shown in Figs. 3.2, 3.4, 3 of App. A and 5 of App. B. The shape of dipole PSF given by the KMF model plus the composite $M1$ model is then shown in Figs. 3.3 and 5 of App. B.

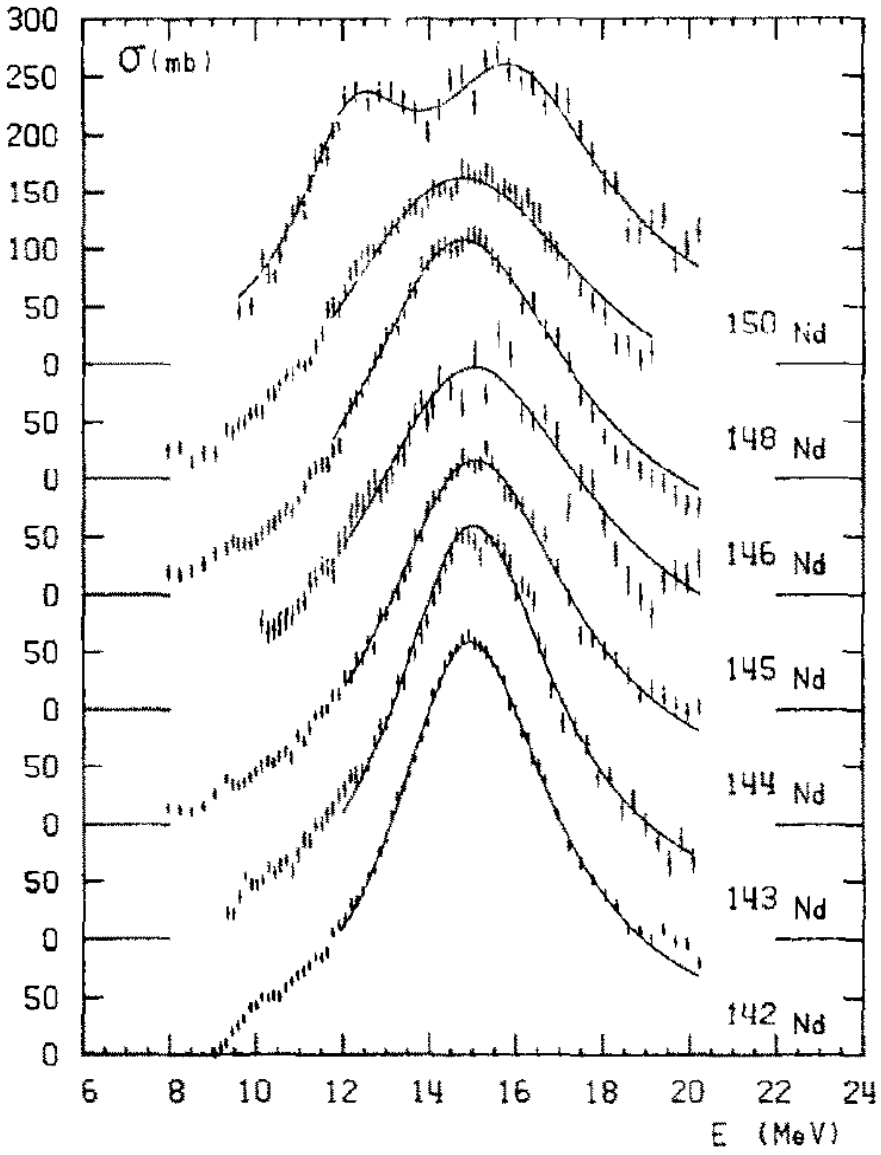

Figure 3.1: The measured photonuclear absorption cross section $\sigma(\gamma,\mathrm{xn})$ of Nd isotopical chain. The lines are the fits of the GEDR by the Lorentzian term (in case of ^{150}Nd sum of two terms). The widening and eventual splitting of the GEDR with the increasing deformation (which for this case of isotopical chain increases with mass) is apparent. The figure is taken from Ref. [70].

Two other phenomenological models use the energy and temperature dependence of Γ_G given in Eq. (3.14). The *Generalized Lorentzian* (GLO) was introduced [71] as

$$S^{(E1)}_{\mathrm{GLO}}(E_\gamma,T_f)=\frac{1}{3(\pi\hbar c)^2}\sigma_G\Gamma_G\left[\frac{E_\gamma\Gamma_G(E_\gamma,T_f)}{\left(E_\gamma^2-E_G^2\right)^2+E_\gamma^2\Gamma_G^2(E_\gamma,T_f)}+F_K\frac{\Gamma_G(0,T_f)}{E_G^3}\right], \tag{3.16}$$

with aim to describe the $E1$ PSF in both low-energy and GDER energy region in spherical nuclei. The so-called *Lorentzian with energy-dependent width* (ELO)

model reads

$$S^{(E1)}_{\mathrm{ELO}}(E_\gamma, T_f) = \frac{1}{3(\pi\hbar c)^2}\sigma_G\Gamma_G\frac{E_\gamma\Gamma_G\left(E_\gamma, T_f\right)}{\left(E_\gamma^2 - E_G^2\right)^2 + E_\gamma^2\Gamma_G^2\left(E_\gamma, T_f\right)}. \tag{3.17}$$

Some models with a form similar to Eq. (3.17) with more complicated form of temperature-dependent width were proposed not long ago, namely the *Generalized Fermi Liquid* (GFL) model in Ref. [72], the *hybrid model* (GH) in Ref. [73], which is very similar to the KMF model in the energy region $E_\gamma \leq S_n$, and a family of *Modified Lorentzian* (MLO) [74] models, which exhibit an additional energy-dependent scaling factor of the $E1$ PSF compared to Eq. (3.17). The detailed description of the models is given also in Ref. [33]. The shape of the MLO2 model in the energy region below S_n is shown in Figs. 3.2, 3.4 and 5 of App. B.

A phenomenological modification of the width of Eq. (3.14) was proposed by Kopecky, Uhl and Chrien [75] to achieve better agreement in case of deformed nuclei. Aditional *ad hoc* empirical factors k_0 and E_{γ_0} modify the width formula

$$\Gamma_G(E_\gamma, T_f, k_0) = \left[k_0 + \frac{E_\gamma - E_{\gamma_0}}{E_G - E_{\gamma_0}}(1 - k_0)\right]\frac{\Gamma_G}{E_G^2}\left(E_\gamma^2 + 4\pi^2T_f^2\right). \tag{3.18}$$

The $E_{\gamma_0} \approx 4.5$ MeV is recommended [76]. For $k_0 > 1$ the width is enhanced with respect to Eq. (3.14). The so-called *Enhanced Generalized Lorentzian* (EGLO) model [75] was introduced by substituting $\Gamma_G(E_\gamma, T_f)$ with $\Gamma_G(E_\gamma, T_f, k_0)$ in Eq. (3.16). For EGLO model in conjunction with BSFG LD model the systematic trend of k_0 was determined based on the comparison with average radiative widths of s-wave neutron resonances and with the experimental values of $E1$ PSF from the average resonance capture data (ARC) compilation, this systematic trend yields a maximum $k_0 = 2.5$ for $A = 160$ [76]. In our simulations we often observe that the recommended value of k_0 does not reproduce the average radiative width, probably because of different $M1$ PSF and LD models, hence we treat k_0 as a free parameter and determine its value based on the simultaneous reproduction of measured spectra and average radiative width of s-wave neutron resonances.

Inserting the width given by Eq. (3.18) into the Eq. (3.17) the so-called *Enhanced Lorentzian with energy dependent width* (EELO) model is introduced. The so-called *Modified Generalized Lorentzian* (MGLO) model [77] was proposed by inserting the width given by Eq. (3.18) into the following expression:

$$S^{(E1)}_{\mathrm{MGLO}}\left(E_\gamma, T_f\right) = \frac{\sigma_G\Gamma_G}{3\left(\pi\hbar c\right)^2}\left[\frac{E_\gamma\Gamma_G(E_\gamma, T_f, k_0)}{\left(E_\gamma^2 - E_G^2\right)^2 + E_\gamma^2\Gamma_G^2(E_\gamma, T_f, k_0)} + F_K\frac{\Gamma_G 4\pi^2T_f^2}{E_G^5}\right]. \tag{3.19}$$

The second term can be also written as $F_K\Gamma_G(0, T_f, 1)/E_G^3$. The MGLO model was introduced as an alternative to the EGLO model. For the decay of highly excited states the MGLO model has a similar high energy behavior as the EGLO model. The MGLO model steadily decreases with decreasing γ-ray energy to similar values as given by the KMF model, unlike the EGLO model it exhibits a significantly smaller preference of low-energy transitions. As in the case of EGLO model the k_0 is treated as a free parameter and adjusted as described above. With $k_0 \approx 1.5 - 2$ the MGLO model is similar to KMF model. The shape

of the MGLO model in the energy region below S_n is shown in Figs. 3.2, 3.4, 3 of App. A and 5 of App. B. The shape of dipole PSF given by the MGLO model plus the composite $M1$ model is then shown in Figs. 3.3, 3.5 and 5 of App. B.

The calculations of S. Goriely and coauthors are available for rare-earth nuclei in the RIPL3 database [38]. These $E1$ PSFs were determined within the QRPA+HFB approach based on the SLy4 Skyrme force [78, 79] and are shown in Figs. 3.2 and 3.4. The HFB results taken from RIPL3 are practically same for $^{162-164}$Dy isotopes.

Recently, the axially-symmetric-deformed QRPA+HFB calculations were performed employing the finite-range D1M Gogny interaction [80]. These new results, again very similar for $^{162-164}$Dy isotopes, are much closer to the MLO2 model than to the previous calculations with SLy4 Skyrme force with the exception of more rapid fall below 3 MeV.

3.2 Magnetic Dipole PSF

The decay of excited nuclear states below S_n in well-deformed rare-earth nuclei is heavily influenced by magnetic dipole ($M1$) transitions. The description of the $M1$ strength for well-deformed nuclei consists of two modes - the spin-flip mode (SF) and the scissors mode (SM). The $M1$ PSF is then composed of Lorentzian terms $S_{\rm SF}^{(M1)}$ and $S_{\rm SM}^{(M1)}$ corresponding to the SF resonance and SM resonance. In our phenomenological studies we sometimes include a constant term $S_{\rm SP}^{(M1)}$ in the $M1$ PSF, which corresponds to the $M1$ strength in the single particle model. The sum $S^{(M1)} = S_{\rm SM}^{(M1)} + S_{\rm SF}^{(M1)} + S_{\rm SP}^{(M1)}$ is denoted as the composite $M1$ PSF model. The strict validity of the Brink hypothesis is assumed for all $M1$ models. We are aware that there is no theoretical justification for the use of the composite $M1$ PSF model. We emphasize that our goal is to describe the experimental observables with easily adjustable $S^{(M1)}$. The shape of the composite $M1$ PSF model might mimic more complicated, maybe temperature-dependent behavior of the $M1$ PSF.

3.2.1 Spin-Flip Mode

In the SF resonance model the $S_{\rm SF}^{(M1)}(E_\gamma)$ is usually assumed to have a Lorentzian shape given in Eq. (3.12) with $E_G \simeq 7$ MeV and $\Gamma_G \simeq 4$ MeV [33]. Experimentally, the $M1$ strength corresponding to the SF mode was measured for several rare-earth nuclei using inelastic proton scattering [81]. A double-humped structure was observed between 5 and 10 MeV. We adopted a double-resonance Lorentzian parametrization of the SF resonance in our simulations with the strength adjusted according to the ARC data [82], see below in Sec. 3.4.1.

3.2.2 Scissors Mode

In 1976, Hilton [83] and later Lo Iudice and Palumbo [84], using the geometrical two rigid rotors model, and Iachello [85], using the proton-neutron interacting boson model, predicted an isovector $M1$ collective vibrational mode in deformed nuclei – the scissors mode.

The first experimental observation of the mode for ground-state transitions was made in high-resolution electron inelastic scattering at low momentum transfer in ^{156}Gd [86] and ^{164}Dy [87]; in Dy the $M1$ excitation at 3.1 MeV revealed a transition strength of 1.5(3) μ_N^2.

A systematic study of the mode for the ground-state transitions in rare-earth nuclei was performed with help of the (γ, γ') reaction – the so-called nuclear resonance fluorescence scattering (NRF) experiments [88]. Experimental data indicated that the total observed $M1$ strength in even-even nuclei in the energy range $E_\gamma \approx 2.5{-}4.0$ MeV is fragmented into several transitions and is proportional to the square of the nuclear deformation [89]. For well-deformed nuclei the total $M1$ strength reaches $\sum B(M1) \approx 3\ \mu_N^2$ and the centroid of the strength is located near 3 MeV, almost independent of A [90]; in even-even Dy nuclei the centroids are at 2.870(5) MeV, 2.956(4) MeV and 3.143(2) MeV while summed $M1$ strengths in energy range $2.7 - 3.7$ MeV are 2.42(18) μ_N^2, 2.49(13) μ_N^2 and 3.18(15) μ_N^2 for ^{160}Dy, ^{162}Dy and ^{164}Dy, respectively [91–93].

The scissors mode in odd ^{163}Dy was thoroughly examined using different reactions. The properties of the SM above ground state were again adressed from NRF - improving the experiment from 90's [94] a wealth of transitions was observed around 3 MeV with summed $M1$ strength $3.3\mu_N^2$ [95]. Data on two-step γ cascades (TSCs), following the thermal neutron capture on ^{162}Dy nucleus, revealed that enhancement of transitions by SM in radiative decay is more general property influencing even nuclear levels with excitation energy of several MeV [96, 97]. The scissors mode was represented by Lorentzian term in $M1$ PSF centered at 3 MeV with integrated strength of $6.2\mu_N^2$ [97]. Meanwhile, isotope chain of dysprosium nuclei was measured using ^{3}He-induced reactions in Oslo Cyclotron Laboratory, see Refs. [35, 62, 63, 98, 99]. The Oslo results on SM parameters of ^{163}Dy were consistent with those coming from TSC data, authors reported the SM strength of $7.8(22)\mu_N^2$ [99].

Futhermore, the strength of SM derived by the Oslo method in neighboring even-even dysprosium isotopes was claimed to be comparable to SM strength in ^{163}Dy, e.g. $6.8(8)\mu_n^2$ in ^{162}Dy [63]. On the contrary, the systematic study of SM in gadolinium isotope chain using data on MSCs accompanying the resonance neutron capture [77,100,101] revealed that the strength of the mode in even-even nuclei is 2–3 times lower compared to neighboring odd ones, e.g. $2.7(8)\mu_N^2$ and $8.0(1.5)\mu_N^2$ in ^{156}Gd and ^{157}Gd respectively.

As in the case of $E1$ PSF, the $M1$ PSF was calculated using the D1M Gogny interaction in the QRPA+HFB calculation [102]. For the gadolinium and dysprosium isotopes the shape of $M1$ PSF somewhat resembles the presence of SM and SF resonances – the concentration of strength is observed just above $E_\gamma \approx 2$ MeV and between $6 - 8$ MeV.

We usually adjusted the absolute value of the $M1$ PSF to be consistent with a ratio of $S^{(E1)}/S^{(M1)}$ deduced from the ARC data. The value of ≈ 7 at 7 MeV was observed in several rare-earth nuclei in average resonance capture experiments [103]. In the most recent evaluation of ARC data [82] this ratio was found to be slightly lower. For the nuclei with $A \simeq 160$ the datapoints lie between 2 and 8, the proposed systematics yields the ratio of 5.25 for $A = 160$ at 6.5 MeV. The specific values are 7.78 (at $E_\gamma = 6.8$ MeV), 3.76 (at 5.7 MeV), 4.39 (at 7.2 MeV), 7.58 (at 7.4 MeV) and 6.42 (at 6.4 MeV) for ^{162,163,164}Dy and ^{156,158}Gd,

respectively. The uncertainty of these ratios are $\approx 10 - 20\%$.

3.3 Electric Quadrupole PSF

In addition to dipole transitions, electric quadrupole ($E2$) transitions might also play a role in the cascade decay after slow neutron capture. If $E2$ transitions are not extremely strong, any effect of them is similar to that of $M1$ transitions due to the same parity selection rules. The use of the giant quadrupole resonance model is recommended in Ref. [33]. Nonetheless, we adopted a simple single-particle model ($S_{SP}^{(E2)} = \text{constant}$) in the majority of our simulations. $S_{SP}^{(E2)}$ was adjusted to reproduce the ratio of partial radiation widths at about 7 MeV measured in average resonance capture experiments in deformed nuclei ($\Gamma(E1)/\Gamma(E2) \gtrsim 100$) [103]. We note here that under these conditions our results do not depend on the choice of the $E2$ PSF model.

3.4 Experimental Determination of Dipole PSF

The description below is restricted to the commonly used sources of experimental information on dipole PSFs in well-deformed rare-earth nuclei.

3.4.1 Average Resonance Capture Data

The intensities of primary transitions were measured in the average resonance capture experiments. The pointwise dipole PSFs were derived from these intensities in the ARC compilation [82] and are shown in Figs. 3.2 and 3.4. The errorbars on the datapoints correspond to the statistical uncertainties only, the considerable spread of the values is due to the Porter-Thomas fluctuations. Because of these fluctuations the ARC datasets should be understood as a set that can be tested for a compatibility with a given PSF model, not as a determination of the value of PSF.

3.4.2 Oslo Method

The pointwise PSF as a function of E_γ was extracted within the Oslo method for chain of dysprosium isotopes [63, 98, 99], see Figs. 3.3, 3.5 and 5 of App. B.

The steps regarding the normalization of Oslo results were described in Sec. 2.6. The parameters of possible SM or pygmy resonances are determined from $S^{\text{Oslo}}(E_\gamma)$ assuming that $S^{\text{Oslo}}(E_\gamma)$ is an exact sum of $E1$ and $M1$ PSFs. This assumption easily breaks down for lighter nuclei when only levels of one parity are accessible in considerable interval of low excitation energies.

In this approach the specific model (with all its parameters but an additional scaling) is chosen for the GEDR part of the $E1$ PSF as well as for the SF resonance in the $M1$ PSF. Because the Oslo method relies on the validity of Brink hypothesis, the authors [63, 98, 99] chose to use a modified KMF model - the KMF prescription with a constant temperature $T_f = const$. However, in the studied dysprosium isotopes the temperature given by Eq. (3.13) changes from

zero to values bigger than 0.6 MeV in the energy range up to S_n. The determined temperature $T_f \approx 0.3$ MeV corresponds to excitation energies $E \lesssim 2$ MeV.

The scaling factor of GEDR and SF resonance was determined to be as high as ≈ 1.8 in case of ^{163}Dy [99]. This factor has no justification and might contradict the well determined magnitude of GEDR as well as the SF resonance.

3.4.3 Low-energy Enhancement of Dipole PSF

Recently, the PSF extracted from the measurement of ^{152,154}Sm(p,dγ) reactions with Ge clover detectors using the Oslo method revealed a strong low-energy PSF enhancement [104], see Figs. 3.3, 3.5 and 5 in App. B. Similar, albeit stronger, enhancement was reported earlier in lighter nuclei. The shell model calculations for lighter nuclei [105–108] indicate the $M1$ nature of a low-energy enhancement with the exponentially decreasing dependence on the γ-ray energy. Particularly, Sieja [108] calculated both the $E1$ and the $M1$ PSFs in lighter nuclei resulting in the $M1$ low-energy PSF enhancement and a flat, non-zero $E1$ PSF for $E_\gamma \to 0$. The analysis of the $M1$ strength in Ref. [107] shows that the sum of the low-energy PSF enhancement and the SM strength does not significantly vary throughout the chain of Fe isotopes. While these calculations deal with lighter nuclei, authors of Ref. [106] argue that the $M1$ low-energy enhancement is expected in nuclei throughout the nuclear chart. There are also calculations suggesting the $E1$ character of the low-energy enhancement, e.g. Ref. [109]. For details about our tests for the presence of low-energy enhancement of dipole PSF see Sec. 6.2.5.

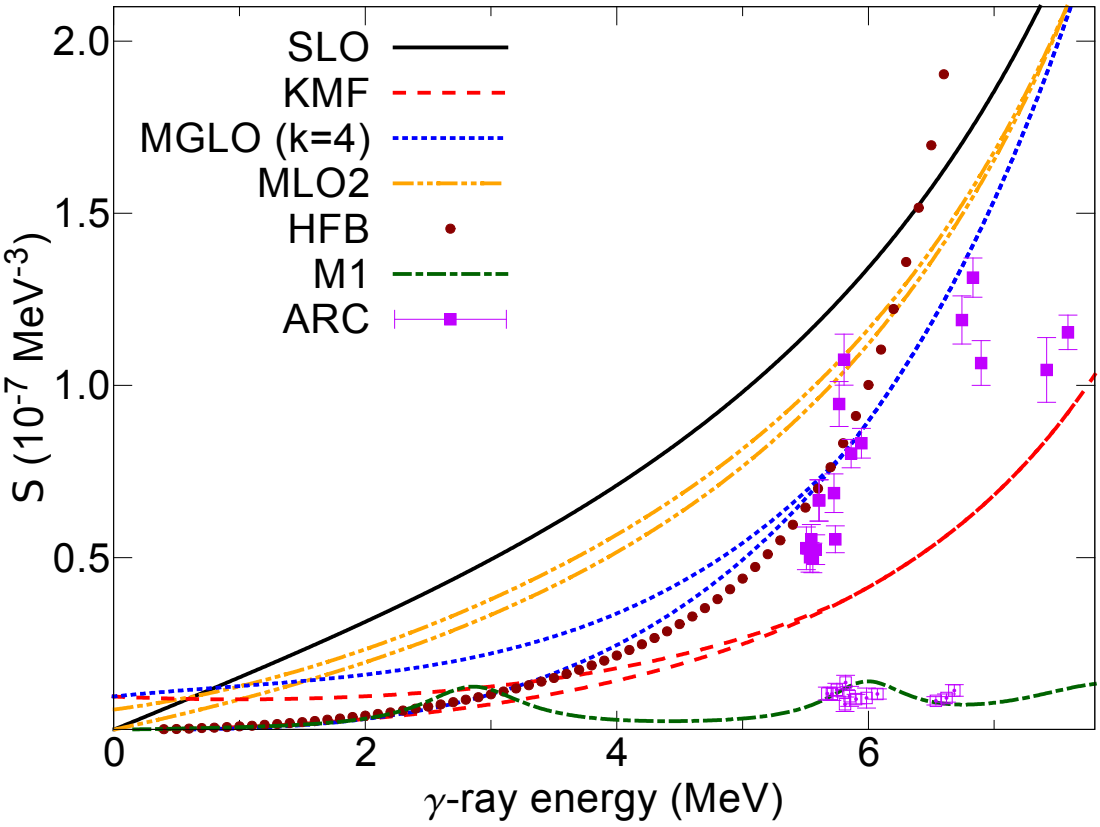

Figure 3.2: Dipole photon strength functions of ^{164}Dy as a function of γ-ray energy for some of the models used in our simulations. The figure displays the $E1$ models as well as the $M1$ model consisting of the SM and SF modes. The SM parameters are $E_{\mathrm{SM}} = 2.9$ MeV, $\Gamma_{\mathrm{SM}} = 1.0$ MeV, and $\sigma_{\mathrm{SM}} = 0.4$ mb. If there are two curves for the $E1$ PSF model, they indicate how the model changes as a function of temperature - the lower curve corresponds to $T_f = 0$ while the upper one to $T_f = \sqrt{(S_n - E_\gamma - \Delta)/a}$. The HFB calculation is taken from Ref. [33]. The data points labeled ARC correspond to the primary transitions in ^{163}Dy(n,γ) reaction and come from the compilation of average resonance capture data [82], the full symbols correspond to the $E1$ primary transitions, the empty symbols to $M1$.

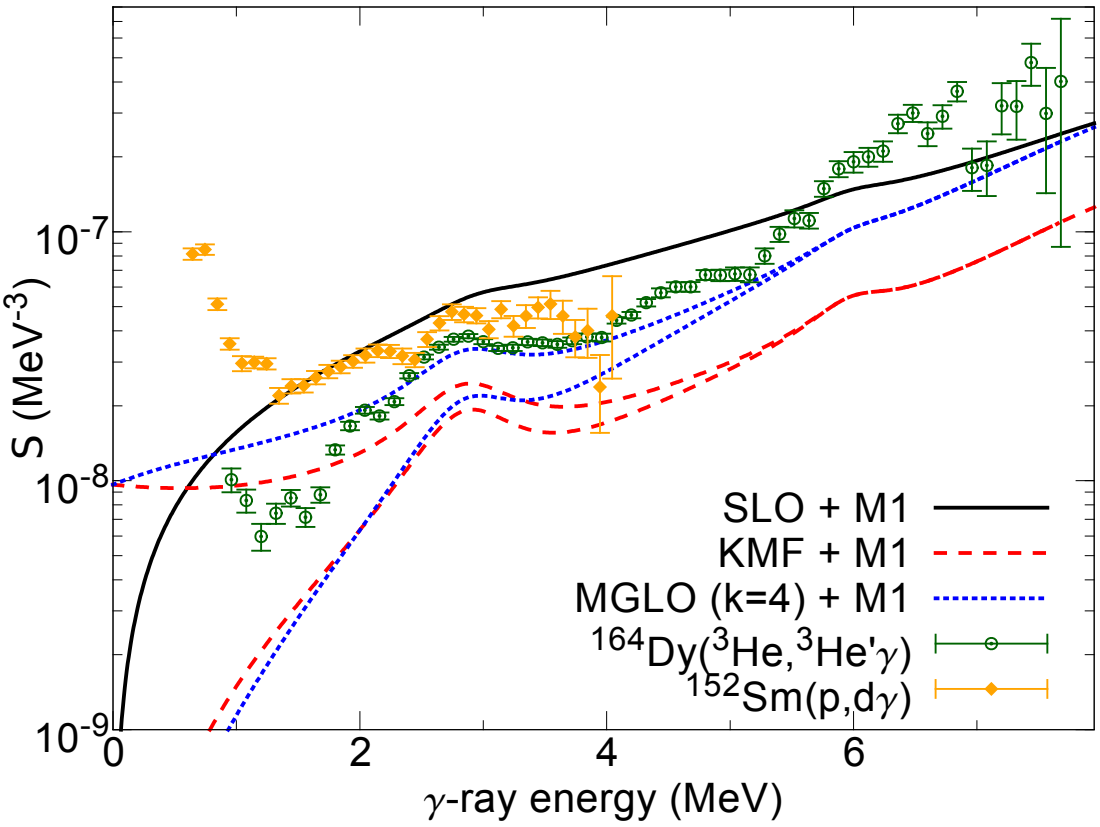

Figure 3.3: Sum of dipole photon strength functions of ^{164}Dy as a function of γ-ray energy for some of the models used in our simulations. The $E1$ and $M1$ PSF models correspond to the Fig. 3.2 as indicated by the labels. The experimental data from ^{3}He-induced and ^{152,4}Sm(p,dγ) reactions are taken from Refs. [99] and [104], respectively.

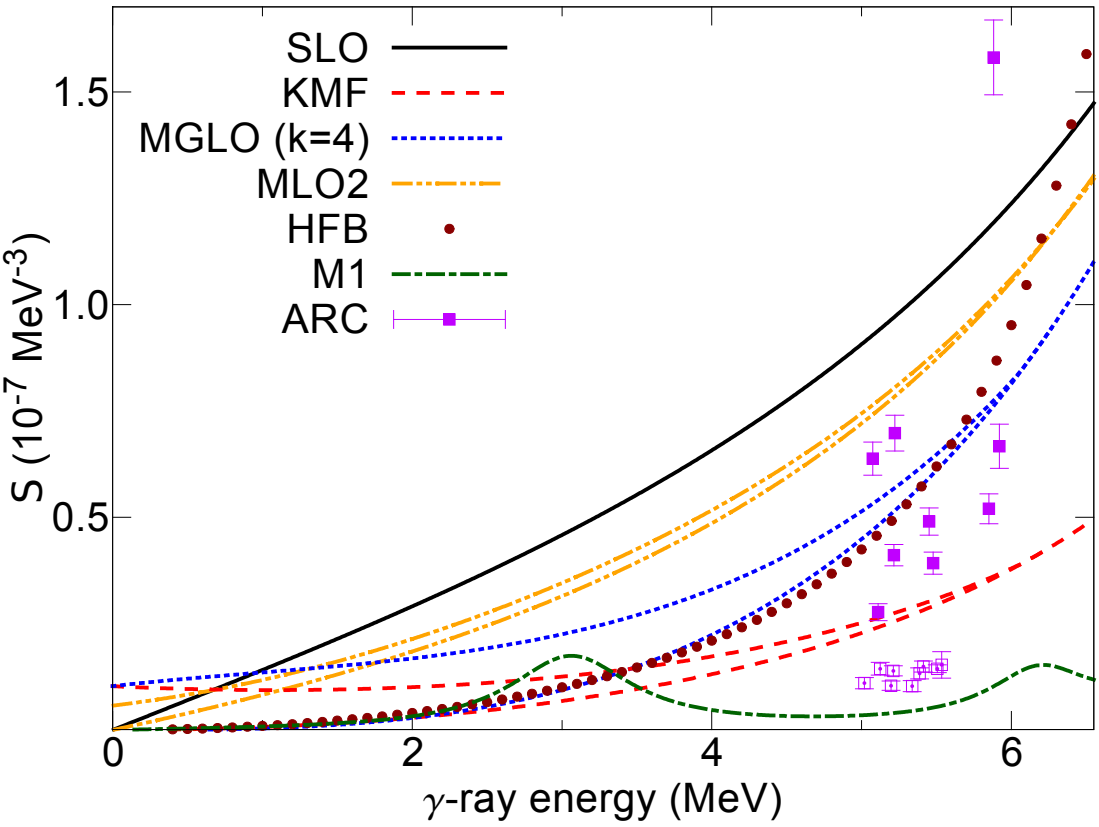

Figure 3.4: Photon strength functions of ^{163}Dy as a function of γ-ray energy for some of the models used in our simulations. The figure displays the $E1$ models as well as the $M1$ model consisting of the SM and SF modes. The SM parameters are $E_{\mathrm{SM}} = 3.1$ MeV, $\Gamma_{\mathrm{SM}} = 1.0$ MeV, and $\sigma_{\mathrm{SM}} = 0.6$ mb. If there are two curves for the $E1$ PSF model, they indicate how the model changes as a function of temperature - the lower curve corresponds to $T_f = 0$ while the upper one to $T_f = \sqrt{(S_n - E_\gamma - \Delta)/a_c}$. The HFB calculation is taken from Ref. [33]. The data points labeled ARC correspond to the primary transitions in ^{162}Dy(n,γ) reaction and come from the compilation of average resonance capture data [82], the full symbols correspond to the $E1$ primary transitions, the empty symbols to $M1$.

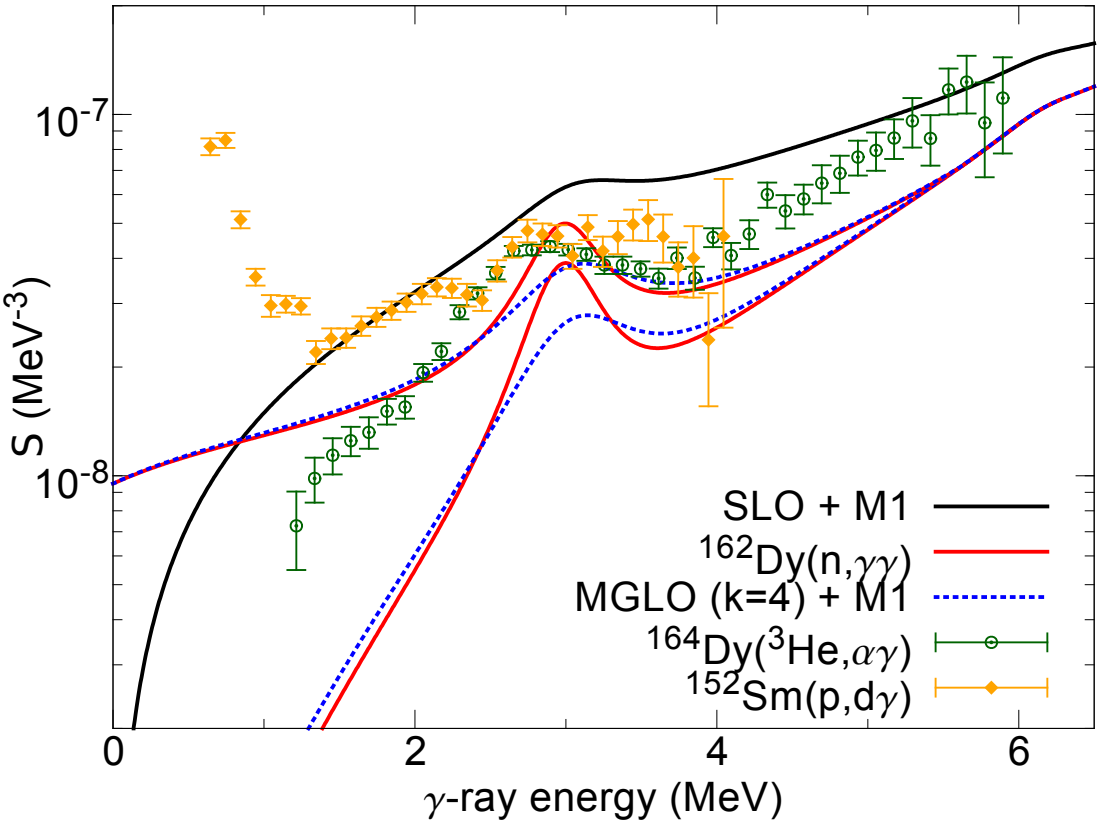

Figure 3.5: Sum of dipole photon strength functions of ^{163}Dy as a function of γ-ray energy for some of the models used in our simulations. The $E1$ and $M1$ PSF models correspond to the Fig. 3.4 as indicated by the labels. The curve labeled ^{162}Dy(n,$\gamma\gamma$) shows the sum of dipole PSFs deduced in the TSC analysis [97]. The experimental data from ^{3}He-induced and ^{152,4}Sm(p,dγ) reactions are taken from Refs. [99] and [104], respectively.

Chapter 4

Simulations of Statistical γ Cascades

About 20 years ago a Monte-Carlo based code for simulation of γ decay, known as DICEBOX [110] was developed. The main aim of the code was to correctly treat the fluctuations of individual transition intensities, which are believed to be governed by the χ^2 distribution with one degree of freedom around the expectation value; which is usually called Porter-Thomas (PT) distribution [111] in nuclear physics. In addition, it introduced a fluctuation in positions of individual levels.

During past 20 years the DICEBOX algorithm has been used in many works for several different purposes. Most often it was exploited for description of the γ decay following the slow neutron radiative capture. Several modifications have been incorporated into the code since late 90's including the recent introduction of the so-called *nuclear suprarealizations*.

In our analyses the γ cascades generated with the DICEBOX algorithm are then folded with the detector response – processed either by the GEANT4 simulation of the detector setup or analytically using the efficiency curves, see Chapter 5.

4.1 The Assumptions of the Method

The method is based on the validity of the statistical model of γ decay and on other simplifying assumptions:

- The role of the particle channels in the process of cascade deexcitation is negligible compared to the electromagnetic channels.
- Below a certain excitation energy denoted as the critical energy E_{crit} a *complete level scheme* is known, in particular the level energies, spins, parities and ratios of branching intensities.
- Individual levels of the simulated nucleus above E_{crit} come from discretization of an *a priori* known LD.
- Each cascade starts from an *initial level*, that is a single, well-defined level with a known excitation energy E_0, spin J_0 and parity π_0.
- The partial width $\Gamma_{\tau\tau'}$ for an electromagnetic transition $\tau \to \tau'$ from a level τ with excitation energy E_τ in the interval $E_0 \geq E_\tau > E_{\mathrm{crit}}$ is assumed to be a random quantity whose value is given by Eq. (4.1).

- Partial widths for different initial and/or final levels are statistically independent.

In a general case, when a mixing of transitions of various types and multipolarities is allowed by selection rules, the partial width $\Gamma_{\tau\tau'}$ is given as

$$\begin{aligned}\Gamma_{\tau\tau'} &= (1+\alpha_{\tau\tau'})\sum_{X\lambda}\Gamma^{(X\lambda)}_{\tau\gamma\tau'} = \\ &= (1+\alpha_{\tau\tau'})\sum_{X\lambda}\left(y^{(X\lambda)}_{\tau\tau'}\right)^2\frac{S^{(X\lambda)}(E_\tau-E_{\tau'},\beta)}{\rho(E_\tau,J_\tau,\pi_\tau)}(E_\tau-E_{\tau'})^{2\lambda+1}, \quad (4.1)\end{aligned}$$

where $\Gamma^{(X\lambda)}_{\tau\gamma\tau'}$ is the partial radiative width for a transition of type X and multipolarity λ, $S^{(X\lambda)}(E_\gamma,\beta)$ is the corresponding PSF, $\rho(E_\tau,J_\tau,\pi_\tau)$ is the LD at initial excitation energy E_τ for levels with spin J_τ and parity π_τ, and $\alpha_{\tau\tau'}$ is the internal conversion coefficient. The two arguments of $S^{(X\lambda)}(E_\gamma,\beta)$ indicate that this quantity is a function of γ-ray energy $E_\gamma = E_\tau - E_{\tau'}$ and possibly of other variables, which are labeled together as β. The $y^{(X\lambda)}_{\tau\tau'}$ is a random number drawn from the normal distribution with a zero mean and a unit variance. These random numbers ensure that the individual partial radiative widths $\Gamma^{(X\lambda)}_{\tau\gamma\tau'}$ fluctuate according to the PT distribution [111].

The summation in Eq. (4.1) in principle goes over all allowed $X\lambda$. In practice, only $E1$, $M1$ and $E2$ transitions are considered above $E_{\rm crit}$. The only possibility of mixed transition is then the $M1+E2$, for which the internal conversion coefficient $\alpha_{\tau\tau'}$ is given as

$$\alpha_{\tau\tau'} = \frac{\alpha^{(M1)}_{\tau\tau'} + \delta^2\alpha^{(E2)}_{\tau\tau'}}{1+\delta^2}, \qquad \delta^2 = \Gamma^{(E2)}_{\tau\gamma\tau'}/\Gamma^{(M1)}_{\tau\gamma\tau'}, \quad (4.2)$$

where δ is the mixing ratio. Within this notation the Eq. (4.1) can be for the $M1+E2$ mixed transition written as

$$\Gamma_{\tau\tau'} = \left(1+\alpha^{(M1)}_{\tau\tau'}\right)\Gamma^{(M1)}_{\tau\gamma\tau'} + \left(1+\alpha^{(E2)}_{\tau\tau'}\right)\Gamma^{(E2)}_{\tau\gamma\tau'}. \quad (4.3)$$

The main hurdle in practical implementations of the above-given assumptions is the huge number of partial radiative widths. In a typical case of a radiative capture of slow neutrons on the rare-earth or actinide nucleus, there is about $10^5 - 10^7$ levels below S_n and corresponding large number of partial radiative widths. This problem can be bypassed by the algorithm described below in Sec. 4.3.

4.2 Nuclear Realizations and Suprarealizations

The control over the fluctuations of observables in DICEBOX simulations was accomplished by introducing the concept of nuclear realizations (NR) [110]. Let us now introduce an additional concept of *nuclear suprarealizations* (NSs).

In Ref. [110] the nuclear realization ω_k denoted a set of all levels together with *all* partial widths. Let us now define a nuclear suprarealization θ_k as a set of I nuclear realizations $\{\omega_{ik}\}_{i=1}^{I}$. The NRs $\omega_{ik}, i = 1, ..., I$ within a given NS θ_k share an identical set of all levels and partial widths excluding the partial widths of the

initial level. In other words, two NRs ω_{ik} and $\omega_{i'k'}$ differ only by the intensities of primary transitions if $k = k'$, i.e. they belong to the same NS θ_k.

Similarly to the case of the original definition of nuclear realizations [110], there exists virtually an infinite number of nuclear realizations ω_{ik}, even within a fixed nuclear suprarealization θ_k. Within the current definition the same results are obtained when simulating one NR for each of K NSs, i.e. with the choice of $I = 1$ leading to a set $\{\omega_{1k}\}_{k=1}^{K}$, compared to the K NRs in original definition of Ref. [110], i.e. to a set $\{\omega_k\}_{k=1}^{K}$.

The introduction of NSs is motivated by the behavior observed in real nuclei. The decay of different neutron resonances, or in general any group of initial levels with a given spin and parity in the close vicinity of excitation energy E_0, differs only in partial widths of primary transitions, while the levels below E_0 and their partial widths are identical. In this contemplation it is assumed that the transition probabilities between these initial levels are negligible.

4.3 The Algorithm

The electromagnetic cascades resulting from the decay of a compound nucleus are generated within the above-mentioned assumptions using the Monte-Carlo technique. The key element necessary for the following algorithm is a deterministic random number generator (RNG), which produces a sequence of quasi-random numbers uniquely predetermined by an adjustable parameter – a seed ζ_τ. A random number drawn from a uniform distribution on the interval $[0, 1)$ is denoted $r^{(\bullet)}$ in the present DICEBOX algorithm, which reads:

1. The nuclear level density $\rho(E, J, \pi)$ is discretized to yield energies E_{τ_k}, spins J_{τ_k} and parities π_{τ_k} of all levels $\tau_k = 1_k, ..., n_k$ between the critical energy $E_{\rm crit}$ and the energy E_0 of the initial level which is labeled by 0.

2. A seed ζ_{τ_k} is ascribed to each level τ_k with excitation energy $E_0 > E_{\tau_k} > E_{\rm crit}$ and stored in the computer memory. The set of partial widths $\Gamma_{\tau_k\tau'_k}$ is generated only at the time of need by the above-mentioned deterministic RNG initialized by the seed ζ_{τ_k}. The seeds ζ_{τ_k} are to be ascribed to individual levels randomly.

3. The seed ζ_0^{ik} is ascribed to the initial level.

4. The partial widths $\Gamma^i_{0\tau'_k}$ for a full set of possible transitions $0 \to \tau'_k$ from the initial level to all accessible levels τ'_k with $E_{\tau'_k} < E_0$ are generated. The RNG is preset using the seed ζ_0^{ik}, attributed to the initial level in Item 3. The total width of the initial level

$$\Gamma_0^{ik} = \sum_{\tau'_k} \Gamma^i_{0\tau'_k} \tag{4.4}$$

is calculated. A full set of branching intensities $I^i_{0\tau'_k}$ from the initial level obtained as

$$I^i_{0\tau'_k} = \Gamma^i_{0\tau'_k}/\Gamma_0^{ik} \tag{4.5}$$

satisfies by definition the normalizing condition

$$\sum_{\tau'_k} I^i_{0\tau'_k} = 1, \tag{4.6}$$

and is stored, because it is used as the starting point of each cascade.

5. A level, $\tau_k^{(1)}$, to which the initial level decays, is determined by a random number $r^{(1)}$. The choice of $\tau_k^{(1)}$ follows from the requirement

$$\sum_{\tau'_k=1}^{\tau_k^{(1)}-1} I^i_{0\tau'_k} \leq r^{(1)} < \sum_{\tau'_k=1}^{\tau_k^{(1)}} I^i_{0\tau'_k}. \tag{4.7}$$

As a result, the level $\tau_k^{(1)}$ at excitation energy $E_{\tau_k^{(1)}}$ of spin $J_{\tau_k^{(1)}}$ and parity $\pi_{\tau_k^{(1)}}$, reached by the first step of the cascade, is determined.

6. If $E_{\tau_k^{(1)}} > E_{\mathrm{crit}}$, the partial widths $\Gamma_{\tau_k^{(1)}\tau'_k}$ for a full set of possible transitions $\tau_k^{(1)} \to \tau'_k$ from the level $\tau_k^{(1)}$ to all accessible levels τ'_k with $E_{\tau'_k} < E_{\tau_k^{(1)}}$ are generated. The RNG is preset using the seed $\zeta_{\tau_k^{(1)}}$. Analogously to the Item 4, the total width $\Gamma_{\tau_k^{(1)}}$ and a full set of branching intensities $I_{\tau_k^{(1)}\tau'_k}$ are calculated.

   If $E_{\tau_k^{(1)}} < E_{\mathrm{crit}}$, the set of branching intensities $I_{\tau_k^{(1)}\tau'_k}$ is calculated exclusively from the experimental data, as stated in Sec. 4.1.

7. Using the set of branching intensities $I_{\tau_k^{(1)}\tau'_k}$ and a random number $r^{(2)}$ a second level, $\tau_k^{(2)}$, to which the level $\tau_k^{(1)}$ decays, is chosen in a way analogous to that described in the Item 5.

8. The procedure from the Items 6 and 7 is repeated until the n-th step of a generated cascade reaches the ground state[1]. Whenever the ground state is reached, all data characterizing a single cascade are available: energies $E_{\tau_k^{(\bullet)}}$, spins $J_{\tau_k^{(\bullet)}}$ and parities $\pi_{\tau_k^{(\bullet)}}$ of all encountered levels, as well as the multipolarities λ and types X of individual transitions together with the multipolarity mixing ratios δ and information whether the decay happened via emission of a photon or a conversion electron. In addition, total radiative width $\Gamma_{\tau_k^{(\bullet)}}$ is also available for all levels above E_{crit}. This set of data is at disposal for calculation of any quantity of interest, which might require an additional simulation of detector response.

9. The simulation of cascades described in the Items 5-8 is to be repeated L times until satisfactory statistical accuracy of a quantity of interest in a given NR is achieved.

[1] In reality, the cascade might not end at the ground but at any "isomeric" state – a state with no possibility of electromagnetic decay. Absence of any assumed electromagnetic decay for levels below E_{crit} can also mimic a level with its lifetime longer than the time resolution of a detection setup.

10. In order to assess the role of the PT fluctuations of the primary transition intensities, the algorithm described in Items 3-9 is to be repeated I times ($i = 1, ..., I$). The nature of many quantities of interest requires the simulation and analysis of the set of NRs $\{\omega_{ik}\}_{i=1}^{I}$ for each NS θ_k. For some quantities of interest it might be sufficient to use only one NR ω_{1k} within each NS θ_k.

11. Finally, to assess the role of the PT fluctuations of transition intensities below initial level and fluctuations due to the random discretization of the LD, the algorithm described in the Items 1-10 is to be repeated K times ($k = 1, ..., K$). The details of calculating the measures of a quantity of interest using the full set $\{\omega_{ik}\}_{i=1,k=1}^{I,K}$ of NRs within NSs are given in Sec. 6.2.

4.4 The Average Radiative Width

The total width of the initial level Γ_0^{ik} given by Eq. (4.4) is in general the only quantity simulated with the DICEBOX code that depends on the absolute values of the PSFs. The simulated average radiative width $\overline{\Gamma}_\gamma = \frac{1}{IK}\sum_{ik}\Gamma_0^{ik}$ can be compared to the experimental average radiative width of s-wave neutron resonances $\overline{\Gamma}_\gamma$ without any influence of the detector system description[2]. This comparison can be used to further restrict the acceptability of the model combinations found in the comparison of other simulated observables with their experimental counterparts, see Sec. 6.2.6.

[2]In principle we can compare not only average but also the distribution of simulated and experimental radiative widths.

Chapter 5

Experimental Setups

To obtain the experimental data for our analyses we rely on two different experimental setups. They differ in some aspects – mainly in the energy of incident neutrons and the detectors used to detect the capture γ rays – but share the nature of a coincidence measurement with well determined initial state of the cascade deexcitation of the compound nucleus.

In a two-step γ cascades measurement a specific subset of capture cascades is analysed – the cascades of multiplicity $M = 2$ terminating at preselected low-lying levels, hereafter referred to as *TSC final levels*, following the thermal neutron capture. We used a pair of Ge detectors installed at the thermal neutron beam guide of the research reactor LVR-15 at the Research Centre Řež. In this TSC experimental setup the samples were situated between the cylindrical surfaces of the HPGe detectors in close side-to-side arrangement.

The aim of the multi-step γ cascades experiments is to measure the cascades depositing practically all of their energy in the detector system for as many multiplicities as possible. The γ-ray calorimeter Detector for Advanced Neutron Capture Experiments (DANCE) – the highly-segmented ball of 160 BaF_2 crystals – is installed at the flight path 14 of the Manuel Lujan Jr. Neutron Scattering Center in the Los Alamos Neutron Science Center (LANSCE) at Los Alamos National Laboratory (LANL). The neutrons coming from the 20 m distant spallation target impinge on the sample, which is placed in the center of the DANCE detector. The initial states of analysed cascades – exclusively the s-wave neutron resonances in well-deformed rare-earth nuclei – are identified using the time-of-flight technique.

5.1 Two-Step γ Cascades Experiment

The TSC method was originally proposed by Hoogenboom in 1958 [112] and later modified for the Ge detectors [113]. As mentioned above, the events of interest are the cascades of multiplicity $M = 2$ terminating at the TSC final level (with excitation energy E_{TSC}), i.e. events for which sum of coincident detector signals equals to a fixed sum energy $E_{\mathrm{sum}} = S_n - E_{\mathrm{TSC}}$. Under these conditions the spectrum of energies deposited in one detector contains all transition energies involved in a TSC deexcitation process – this spectrum is called the TSC spectrum. The TSC method ensures that a cascade $S_n \to E_i \to E_{\mathrm{TSC}}$ via an intermediate level i contributes almost exclusively to the given TSC spectrum by a pair of narrow,

symmetrically situated lines at γ-ray energies $E_{\gamma_1} = S_n - E_i$ and $E_{\gamma_2} = E_i - E_{\mathrm{TSC}}$.

The typical TSC spectrum of a rare-earth nucleus contains several strong, well-resolved lines at low and high energies originating from the TSCs via low-lying levels. The mid-part of the spectrum consists of a number of rather weak lines coresponding to the TSCs through the levels of the quasi-continuum. The main goal of our TSC analyses is to find the models of PSFs and LD that can describe the mid-parts of the TSC spectra.

5.1.1 TSC Experimental Setup

In case of our TSC experiment two Ge detectors were installed at the end of a six meter long curved mirror neutron guide of the research reactor LVR-15 in Řež. The basic layout of the experimental setup is shown in Fig. 5.1. The Ge detectors – one Ge(Li) and one HPGe with efficiencies 12% and 20%, respectively – were placed in close side-to-side geometry with a sample situated in between their cylindrical surfaces [114]. The lithium carbonate ($^6Li_2CO_3$) plate with a small aperture was placed at the entrance to the sample area to reduce and shape the beam to 20×2 mm^2 with a uniform neutron flux of 3×10^6 n cm^{-2} s^{-1}. Same material was used to shield the detectors from sample-scattered and background neutrons, the $^6Li_2CO_3$ parts are depicted in light grey in Fig. 5.1, while the shielding from the γ background made of lead is depicted in dark grey.

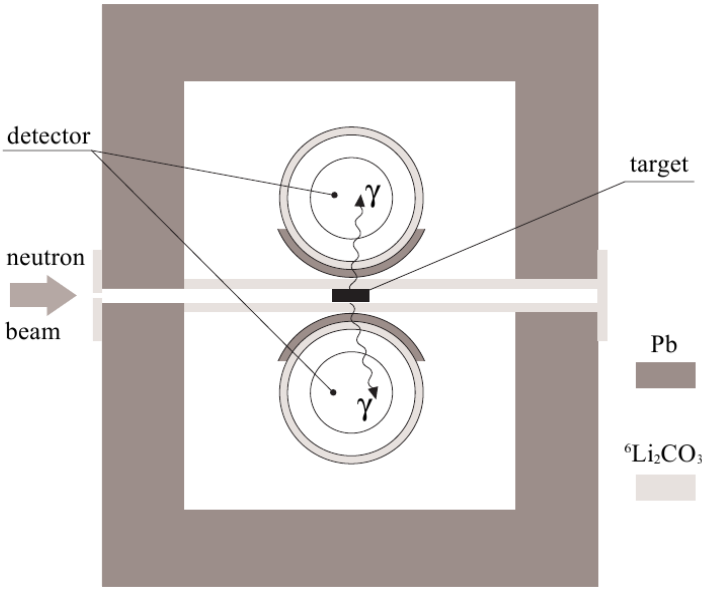

Figure 5.1: The layout of the TSC experiment. The shielding is drawn – lead in dark grey and lithium carbonate ($^6Li_2CO_3$) in light grey. The figure is taken from Ref. [115].

The layers of lead between the sample and each detector served an additional purpose. They reduced the γ cross-talk between the detectors – the events when one of the detectors registers (i) a γ ray after its backscattering in the other detector, (ii) an annihilation γ ray after pair production and the subsequent positron annihilation in the other detector, or (iii) a bremsstrahlung coming from

the other detector or (iv) any combination of (i)-(iii) which deposits the given E_{sum} in the detector pair[1]. The effect of so-called vetoing was also significantly decreased by this lead shielding. The vetoing is the detection of the decay of a TSC final level in coincidence with the detection of its feeding by TSC. It changes a desired TSC event to a parasitic event corresponding to another low-lying level, possibly another TSC final level, of lower excitation energy. As the deexcitations of TSC final levels are usually of low energy (tens or few hundreds of keV's), the lead layers significantly decrease the contribution of vetoing. Nevertheless, we calculated the corrections for vetoing using a decay scheme of each studied isotope and the energy dependence of the absolute detection efficiencies.

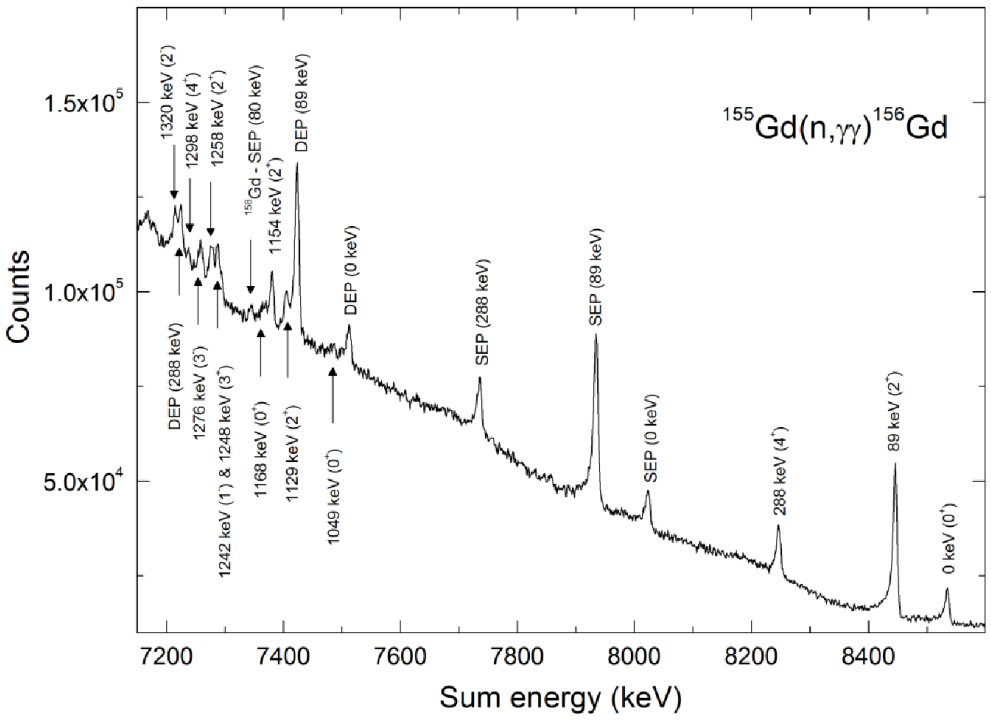

Figure 5.2: The experimental spectrum of sum energies as measured in the ^{155}Gd$(n,\gamma)^{156}$Gd TSC experiment. All observed TSC final levels are labeled by their energy E_{TSC} and J^{π} assignment. The TSC final levels selected for the analysis are specified later. The single and double escape peaks are marked as SEP and DEP with the energy of the corresponding TSC final level E_{TSC}. In the sum energy spectrum of the TSC experiment one can observe also triple and quadruple escape peaks – these were measured in our experiments and are out of the plotted ranges.

The auxiliary measurements of ^{137}Cs and ^{60}Co calibration sources were used to correct the GEANT3 simulations [116] of the absolute detection efficiencies, the corrections did not exceed 10%. It is important to note that the detector efficiencies for γ-ray energies $E_{\gamma} \geq 500$ keV remain almost unchanged after inserting the above discussed lead layers. To estimate the peak detection efficiencies ($\sim 1\%$ at 500 keV) we used also the measurements of ^{133}Ba and ^{152}Eu calibration sources and a measurement of ^{35}Cl$(n,\gamma)^{36}$Cl reaction. All of these auxiliary measure-

[1]For example the annihilation γ ray from (ii) can undergo backscattering in one of the detectors and reach the other detector.

ments were used for the channel-to-energy calibration. The energy resolution of the detectors is $\sim$ 2 keV at 1332 keV, the combined resolution in the sum energy spectra is $\sim$ 8 keV at $\sim$ 8 MeV, see Figs. 5.2 and 5.3. Futher details of the experimental setup are given in Refs. [114, 116].

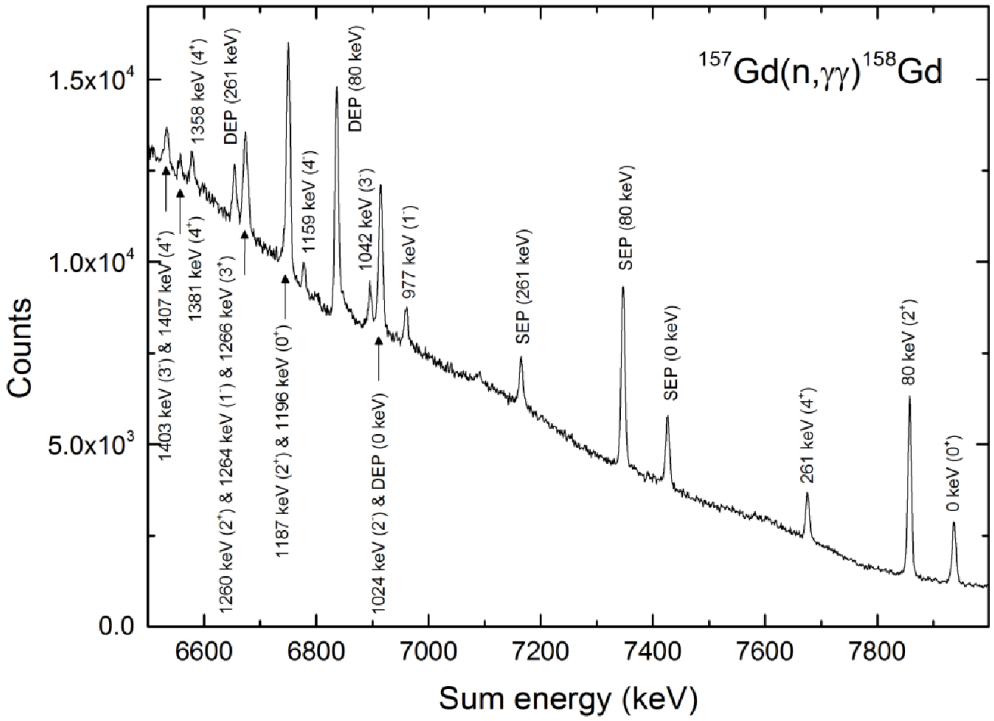

Figure 5.3: The same as in Fig. 5.2 but for the ^{157}Gd$(n,\gamma)^{158}$Gd reaction.

5.1.2 TSC Data Acquisition and Data Processing

The data acquisition hardware, a traditional fast/slow coincidence arrangement, is described in Ref. [114]. Information about each individual event consisting of amplitudes of both detector signals and their time difference Δt was recorded in a list mode for off-line analysis.

When constructing the TSC spectra the background caused by the accidental coincidences and the Compton effect is removed [114, 116]. By choosing three intervals of sum energy and three time difference intervals we define nine rectangular regions in the $E_{\rm sum} \times \Delta t$ plane. The central region contains the desired events – true coincidences terminating at the TSC final level with $E_{\rm sum} = S_n - E_{\rm TSC}$, while the other eight regions are used for the background subtraction, which is visualized in Fig. 7 of Ref. [114]. The background remaining in the TSC spectra after the subtraction was estimated using GEANT3 simulations [116]. At most $\approx 1\%$ of cascades with energies E_{γ_1} and E_{γ_2} contribute to the spectrum outside of the E_{γ_1} and E_{γ_2} lines, the individual contributions of processes (i)-(iii) described in Sec. 5.1.1 and their characteristic energies were identified, see Fig. 5 of Ref. [116].

As an example, the TSC spectrum for 88.97 keV, $J^\pi = 2^+$ TSC final level in ^{156}Gd is shown in Fig. 5.4. In Fig. 1 of App. A we plot the TSC spectrum populating the $J^\pi = 2^+$, 79.5 keV level in ^{158}Gd. The high energy half is flipped and plotted under the low energy half of the spectrum to emphasize its symmetry.

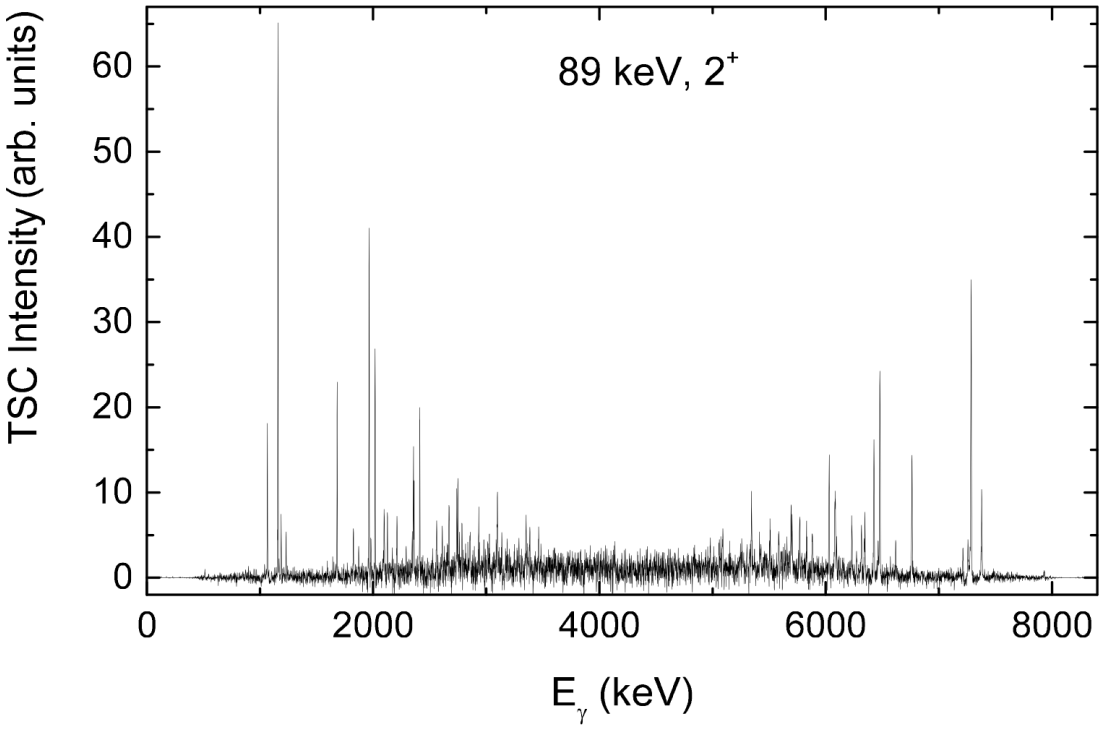

Figure 5.4: Background-free TSC spectrum for 88.97 keV, $J^\pi = 2^+$ TSC final level in ^{156}Gd. The symmetry of the spectrum around its midpoint ($E_\gamma = 4223.71$ keV) is evident (taking into account the effect of detector resolution). For example, four peaks just above $E_\gamma = 1000$ keV corresponding to the cascades through levels at 1154.15 keV $J^\pi = 2^+$, 1248.00 keV $J^\pi = 3^+$, 1276.14 keV $J^\pi = 3^-$ and 1319.66 keV $J^\pi = 2^-$ are easily identified, the strongest cascade via the 1248.00 keV level was used for the normalization as described in the text.

The background subtraction procedure produces the so-called bipolar structures [117]. An example of a bipolar structure is shown in Fig. 8 of Ref. [114]. A bipolar structure originates from a partial detection of a very strong cascade with $E_{\gamma_1} + E_{\gamma_2} \geq E_{\mathrm{sum}}$ when part of the energy is lost due to the Compton scattering. The area of a given bipolar structure is zero, its shape depends on widths and central values of the E_{sum} and Δt intervals chosen for the background subtraction, the only free parameter is the magnitude. In principle, the bipolar structures can be subtracted from the TSC spectra. However, as the visible bipolar structures practically occur only at the low and high energy parts of TSC spectra, they are out of the energy intervals of interest. Moreover, as the TSC analyses focusing on PSFs and LD use the TSC spectra binned into relatively coarse bins with width of hundreds of keV's, the bipolar structures often contribute by their integral which is zero as mentioned above. One of the bipolar structures observed in present analysis is shown in Fig. 2 and discussed in detail in App. A.

The TSC final level is in general also fed by three or more step cascades, in case of the rare-earth isotopes often with higher probability than by two step cascades. The probability of registration of three and more step cascade by a pair of relatively low efficient Ge detectors decreases with increasing number of steps. Nevertheless, the contribution of three and four step cascades is correctly treated in our simulations, see Sec. 5.1.3.

In order to express the yields of the experimental TSC spectra in well-defined intensity units and to normalize the simulated TSC spectra to the experimental ones, we determine an intensity of at least one distinct TSC cascade via a well-resolved low-lying level, see Fig. 5.4. The knowledge of the branching intensities of the involved primary and secondary transitions is essential and sometimes requires an auxiliary measurement, see Sec. 5.1.4. As a result of this procedure we can express the yields of all accumulated TSC spectra in units of number of emitted γ rays per neutron capture and unit of γ-ray energy.

5.1.3 Specific Features of TSC Simulations

The simulations of TSC experiments are specific compared to simulations of other experiments. Usually, the capture cascades generated by the DICEBOX code are fed into the Monte Carlo simulations of the detection system, often based on the GEANT4 toolkit [118]. However, in the case of TSC analyses the description of the setup is achieved using the efficiency curves. There are several effects that need to be taken care of, namely the angular correlation of γ rays and a possibility of detecting three- and more-step cascades. Besides the TSC, we account for the detection of three- and four-step cascades terminating at the TSC final levels, which typically represent $\lesssim 10\%$ of the integrated TSC intensity. We can safely omit higher multiplicity cascades because the probability of detecting M γ rays significantly decreases with increasing M.

The correction for the angular γ-γ correlation between primary and secondary γ ray is included using the angular correlation function expressed as [119]

$$W(\theta) = 1 + \sum_{L=2,4,\ldots} B_L(\gamma_1) A_L(\gamma_2) Q_L P_L(\cos\theta), \tag{5.1}$$

where B_L and A_L describe properties of the first and second γ transition, respectively, P_L are the Legendre polynomials of the L^{th} order and Q_L are the attenuation coefficients that describe the smearing of the angular correlation function due to finite detector solid angles. These coefficients can be calculated for a given detector and experimental setup [120]. In the very close geometry of our experimental setup the correction due to angular correlation does not exceed 10% for a dipole-dipole cascade. On the other hand mixed (i.e. $M1 + E2$) and quadrupole-quadrupole cascades may require a rather large correction.

5.1.4 The Specifics of Gadolinium TSC Measurements

As mentioned in App. A, the measured samples were enriched in ^{155}Gd and ^{157}Gd to 91.2 and 82.5 %, weighting 115 and 58 mg, respectively. Both were irradiated with the uniform neutron flux of $3 \times 10^6 \mathrm{cm}^{-2}\mathrm{s}^{-1}$ for 300 hours.

The measured spectra of sum energies are shown in Figs. 5.2 and 5.3. The background-free TSC spectra are shown in Figs. 5.4 and 1 and 3 of App. A.

The presumably complete decay schemes were taken from the recent evaluations of various experimental data, namely from Refs. [121, 122] for ^{156,158}Gd, respectively. The critical energies were chosen as $E_{\mathrm{crit}} = 1.95$ and 2.1 MeV for ^{156,158}Gd, respectively.

For the normalization of simulated and experimental TSC spectra two cascades in each nucleus, involving 7288- and 6750-keV primary transitions in ^{156}Gd

and ^{158}Gd, respectively, were chosen. The auxiliary measurement of these normalization TSC is described in App. A.

5.2 Multi-Step γ Cascades Experiment

The total absorption technique is one of the four methods to measure the neutron capture cross section[2]. Aiming at the detection efficiency for a γ-ray cascade as close to 100% as possible, high efficiency detectors cover a solid angle as close to 4π as possible.

The DANCE detector is based on the array of 42 BaF_2 crystals formerly installed at Forschungszentrum Karlsruhe [123]. This system has proven very useful in the field of cross-section measurements for nuclear astrophysics with a low-energy neutron source. The design studies of the DANCE array [124] were performed using the GEANT4 simulations [118]. Among other features, they accounted for the difference of the neutron sources. As a results, the DANCE detector displays higher granularity – it consists of 160 BaF_2 crystals, which enables more precise distinction of higher multiplicity γ-ray cascades as well as of the background events induced by sample-scattered neutrons [125]. The current knowledge of the DANCE detector response is achieved and routinely verified using the dedicated Monte-Carlo simulations [126] based on the GEANT4 toolkit [118]. The simulation of the DANCE detector response to cascades generated by DICEBOX represents an irreplaceable step in our MSC analyses.

5.2.1 MSC Experimental Setup

The DANCE detector is installed at the flight path 14 of the Manuel Lujan Jr. Neutron Scattering Center in the LANSCE at LANL. The neutrons are produced by the spallation reaction of 800-MeV protons from the LANSCE linac striking a tungsten target. The moderated spallation neutron source [127] produces a white spectrum of energies ranging from sub-thermal to hundreds of MeV at repetition rate of 20 Hz. The distance from the neutron source to the DANCE detector is about 20 m.

One hemisphere of the DANCE detector is shown in Fig. 5.5. Each BaF_2 crystal is wrapped in a PVC foil and glued to a photo multiplier tube (PMT) [125]. The crystal-PMT modules are held by the aluminium housings and supporting structure. A 6-cm-thick ^{6}LiH shell is placed between the sample and the BaF_2 crystals in order to reduce the scattered neutron flux striking the crystals.

The energy calibration of the individual DANCE crystals was performed with a combination of γ-ray sources (^{137}Cs, ^{88}Y, ^{22}Na). The signals of α particles from the intrinsic radioactivity in the BaF_2 crystals due to ^{226}Ra and its daughters were accumulated on a run-by-run basis to provide the stability check of the energy calibration, i.e. the energy alignment of all crystals for the whole measurement in the off-line analysis. The energy resolution is about 16% and 7% for 1- and 6-MeV γ rays, respectively.

[2]The other methods are activation, level population spectroscopy and total energy technique (often in conjunction with use of the pulse height weighting function).

The detection efficiency of the DANCE detector array was measured using the ^{60}Co and above mentioned γ-ray sources and verified by the GEANT4 simulations [126]. For a 1-MeV γ ray the efficiency is 86% and the total efficiency for detection of at least one γ ray from a cascade typically exceeds 95%. In our MSC analyses we use only cascades that were, roughly speaking, fully detected. In such case the efficiency falls to several tens of percent, exact value depends on the measured isotope.

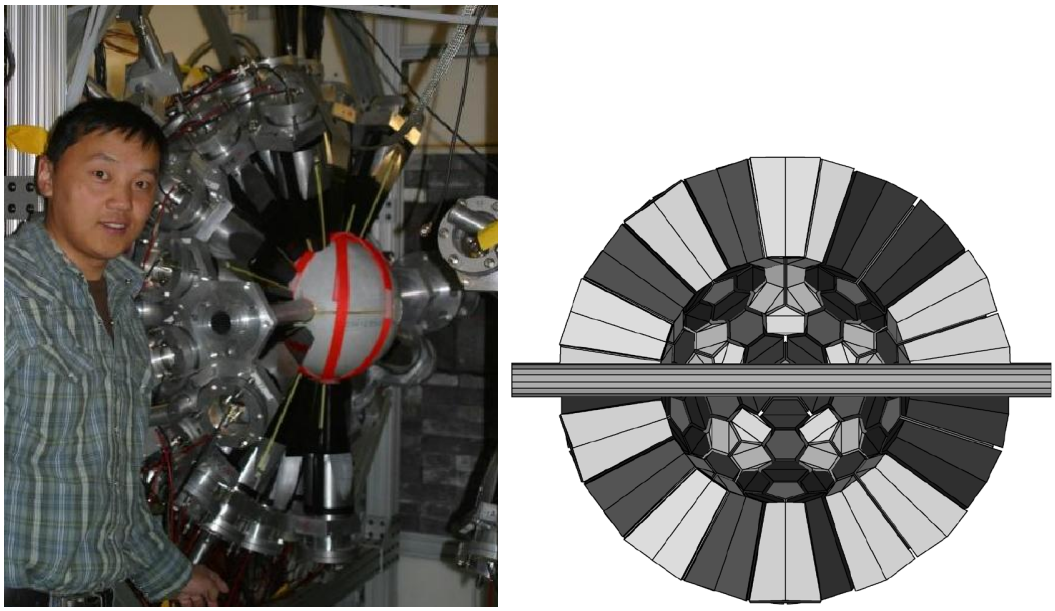

Figure 5.5: Left – a cutaway view of one hemisphere of the DANCE calorimeter. The gray ^{6}LiH shell is placed around the target in the center of the detector. Right – the GEANT4 implementation of the corresponding hemisphere, the colors indicate the four different shapes of BaF_2 crystals used in the detector. The ^{6}LiH shell is implemented in the simulations but not shown. The figure is taken from Ref. [128].

5.2.2 MSC Data Acquisition and Data Processing

The DANCE acquisition system [128] is based on digitization of signals from all 160 BaF_2 detectors using four-channel Acqiris DC265 digitizers with a sampling rate of 500 mega samples per second. Intensities of the fast (decay time $\approx$ 600 ps) and slow (decay time $\approx$ 600 ns) components of the scintillation signal from each BaF_2 detector are collected independently. The typical signals of a γ ray and an α particle are shown in Fig. 5.6. The α-background comes from natural radioactivity of Ra in the BaF_2 crystals [125]. The particle identification procedure is based on the obvious difference between the signals – the fast component is lacking in the α particle signals. The γ-ray signals are stored for futher analysis, the α-particle signals are utilized for the fine energy calibration of the individual crystals during the measurement. A timestamp of γ-ray arrival determined by the leading edge of the fast component is also stored and all signals are considered to belong to the same event if they arrive within preset time window, usually set to few tens of ns.

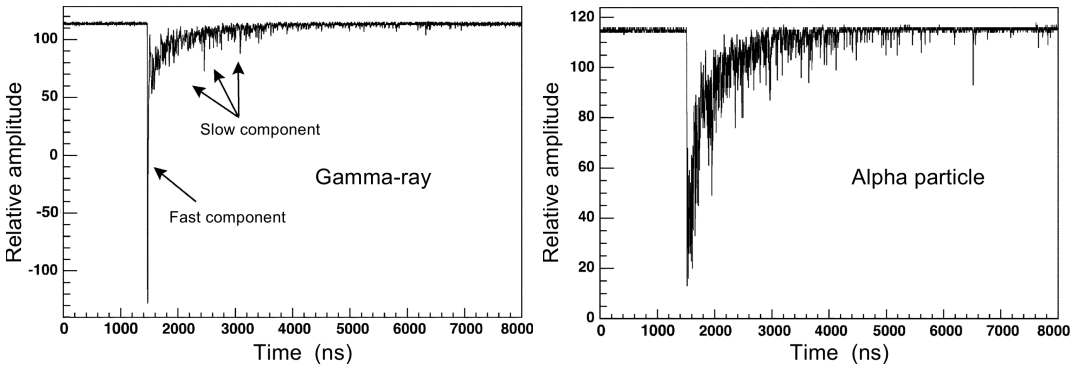

Figure 5.6: The signals from a BaF_2 crystal corresponding to left – γ ray and right – α particle. The characteristic difference between the signals, namely the lack of a fast component in the α-particle signal, is utilized for the particle identification in the analysis. The figure is taken from Ref. [128].

The calibration measurements and simulations show that an emitted γ ray does not necessarily deposit its full energy in a single crystal, but rather several, often neighboring, BaF_2 crystals [126], see Fig. 5.7. The number of crystals that fire during γ-ray cascade detection is thus usually higher than the true multiplicity. We combine all contiguous crystals that have fired during an event into *cluster*. In other words, the cluster is a set of all neighboring crystals firing within preset time window. The number of clusters observed in a capture event is called the *cluster multiplicity* M. As pointed out in the App. B, the results of our analyses do not depend on the choice between cluster and crystal multiplicity. The cluster multiplicity tends to be more practical and to better resemble the real multiplicity. To consider each cluster as the response of the detector array to a single γ ray is not fully correct, as can be seen from Fig. 5.7. The crucial point is that the procedure of clusterization is identical in the experimental data reduction and in the detector response simulation.

5.2.3 The Specifics of Dysprosium MSC Measurements

All enriched Dy targets were prepared at the Oak Ridge National Laboratory as self-supporting metal foils. Their masses and isotopic compositions are specified in Tab. 5.1. Data were accumulated for approximately one week for each target during regular beam cycles at LANSCE. The presumably complete decay schemes were taken from the recent evaluations of various experimental data, namely from Refs. [129–131] for $^{162-164}$Dy, respectively. The critical energies were chosen as specified in Tab. 5.2.

The time-of-flight can be calculated as a difference between the γ-ray time-stamp and the time of the initial saturation of the PMT by the relativistic particles. Alternatively the time information about the protons inducing the spallation reaction from the LANSCE linac can be used. The geometrical flight path length is used for the rough conversion of the time-of-flight to neutron kinetic energy. The final adjustment is performed using the tabulated energies of well-know resonances [36]. Each detected event, constructed with the preset time window of 20 ns, is then characterized by corresponding neutron energy, the cluster multiplicity M, the sum of deposited energies E_{sum} and the individual energies

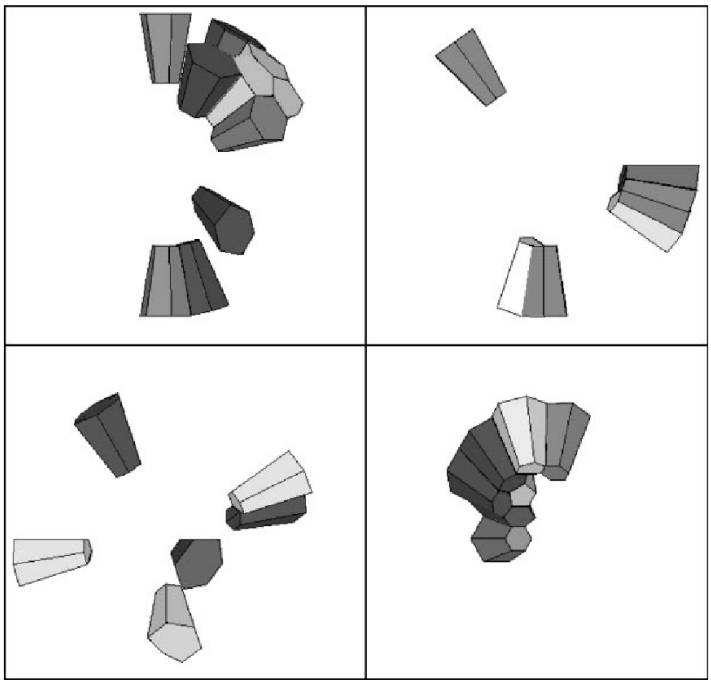

Figure 5.7: The visualization of the examples of the DANCE detector response to one 6 MeV γ ray as simulated by the GEANT4 toolkit. The shade of the crystals indicates the amount of deposited energy, only crystals with more than 50 keV are shown. The figure is taken from Ref. [124].

Target	Mass	Isotopic abundance (%)				
	(mg)	^{160}Dy	^{161}Dy	^{162}Dy	^{163}Dy	^{164}Dy
^{161}Dy	31	0.33(2)	95.69(37)	2.52(13)	0.90(8)	0.56(5)
^{162}Dy	69	0.08(2)	1.22(2)	96.26(2)	1.74(2)	0.69(1)
^{163}Dy	32	0.03(1)	0.36(1)	1.23(2)	96.86(4)	1.52(2)

Table 5.1: Mass and isotopic composition of the measured dysprosium targets. The abundance is given in atomic percent. The maximum abundance of other stable dysprosium isotopes is 0.03%. The maximum abundance of other elements is $< 0.2\%$ of Zn and Ce.

deposited in M clusters.

A relevant part of the experimental $E_n \times E_{\rm sum}$ spectrum for ^{162}Dy$(n,\gamma)^{163}$Dy reaction is shown in Fig. 5.8. Inspecting this spectrum (or its projection on neutron energy axis) we define the intervals of neutron energies coresponding to strong, well-resolved resonances with sufficient statistics and unambiguous spin assignment (in case of odd target nuclei). In the range of inspected neutron energies we observe only s-wave resonances. For these intervals of neutron energies we construct the spectra of sums of deposited energies, hereafter called *sum-energy spectra*. These spectra are shown in Fig. 5.9 and Fig. 2 of App. B.

As explained in App. B each sum-energy spectrum consists of (i) a peak near the neutron separation energy S_n, see Tab. 5.2, which corresponds to detection of all γ-ray energy emitted in a cascade, and (ii) a low-energy tail, which is formed

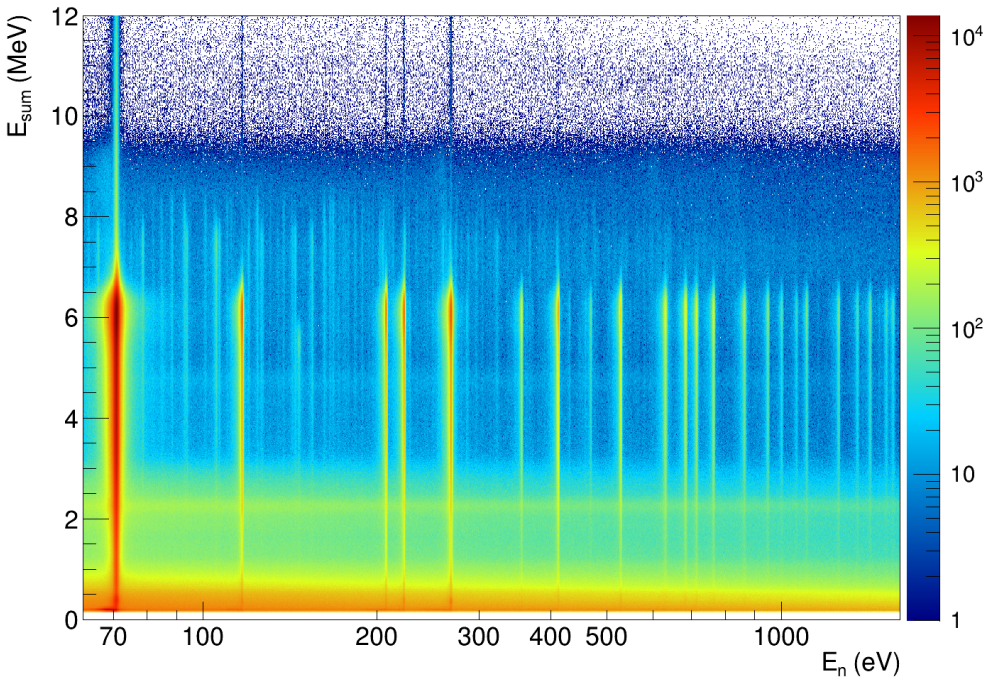

Figure 5.8: The experimental $E_n \times E_{\text{sum}}$ spectrum for all multiplicities for the ^{162}Dy(n,γ)^{163}Dy reaction. The resonance visible at $E_n = 71.10$ eV is the first resonance included in our analysis.

by events where a part of the emitted γ-ray energy escapes the detection. For low multiplicities, $M < 3$, there is also a strong contribution from background which dominantly comes from natural β radioactivity in the BaF_2 crystals at $E_\Sigma < 3$ MeV. Sometimes resonances in different isotopes have very similar energies to those under study. If there is a strong resonance in some Dy impurity of the target, a peak at S_n from the product nucleus appears in the spectrum. Such a "parasitic" resonance (from ^{160}Dy target) is clearly visible in the sum-energy spectrum for the 10.26 eV resonance in ^{162}Dy at ≈ 6 MeV, see Fig. 2 of App. B.

From the inspection of sum-energy spectra we define the intervals of sum energies E_Σ that contain mainly the events of the fully detected γ cascades. The sum-energy spectra are then normalized to the same total number of events for $M \geq 2$ in the E_Σ intervals listed in Tab. 5.2. The events with deposited sum energy falling into E_Σ intervals are used to construct the *experimental MSC spectra*. For a given resonance, an experimental MSC spectrum for multiplicity M is constructed by incrementing counts in M bins corresponding to the γ energies deposited in the M individual clusters within an event. The bin width of 100 keV, which is close to energy resolution of crystals for low energies, was chosen. The experimental MSC spectra inherit the normalization of sum-energy spectra. Examples of experimental MSC spectra are shown in Fig. 5.11 and Fig. 3 of App. B.

The background subtraction and the uncertainties of the MSC spectra are discussed in the App. B, together with the number of analysed resonances for odd Dy targets. For the ^{162}Dy target we obtained experimental MSC spectra for 17 s-wave resonances with energies from 71.1 eV to 1261.4 eV. We excluded

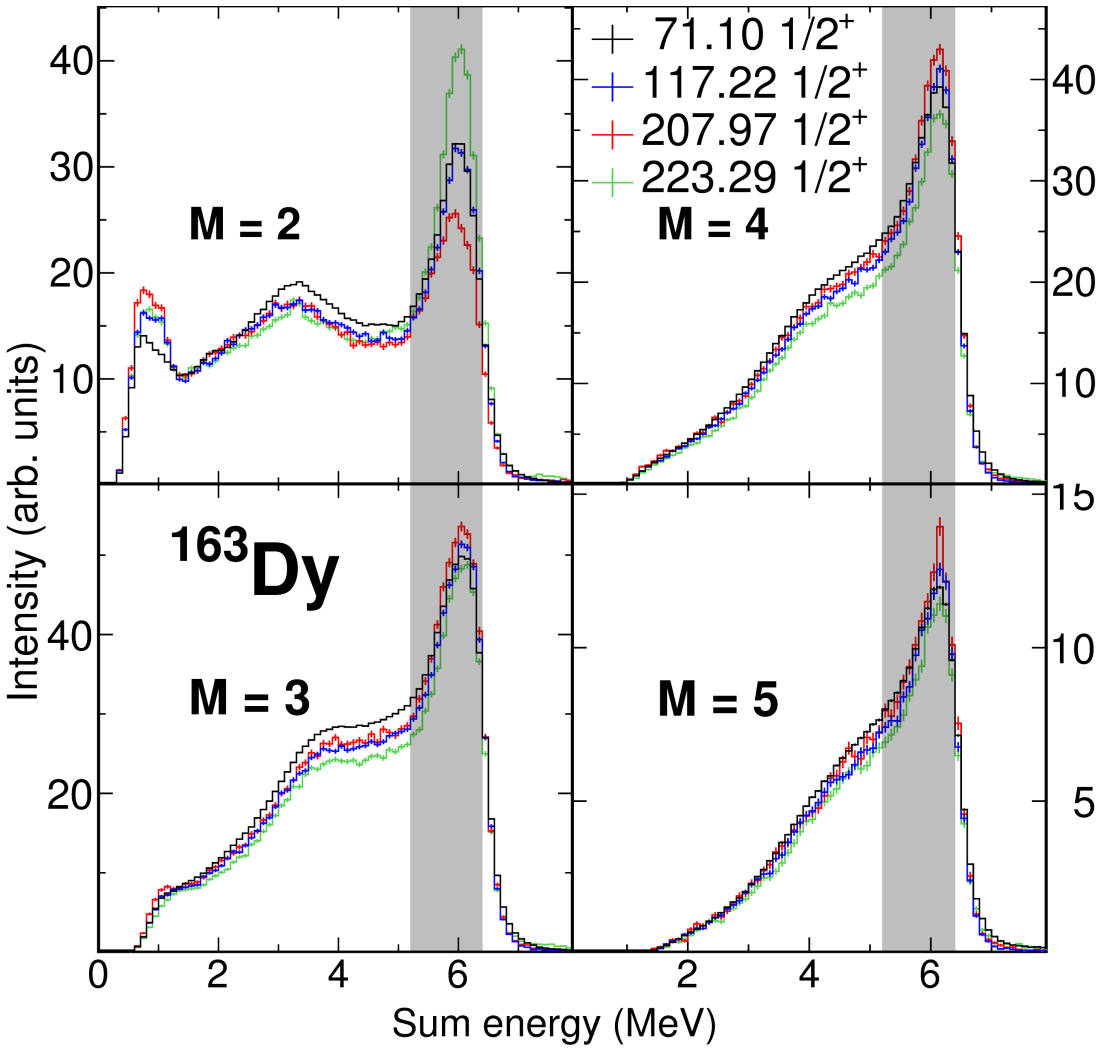

Figure 5.9: The examples of experimental sum-energy spectra for individual cluster multiplicities M. The energies and J^π assignments, $1/2^+$ in all cases, of the resonances from the ^{162}Dy(n,γ)^{163}Dy reaction are indicated. The shaded areas represent the E_Σ interval for ^{163}Dy as specified in Tab. 5.2. The spectra are normalized as described in the text.

Target	S_n (MeV)	E_Σ (MeV)	$E_{\rm crit}$ (MeV)
^{161}Dy	8.197	7.6 – 8.4	1.87
^{162}Dy	6.271	5.2 – 6.4	0.89
^{163}Dy	7.658	7.0 – 7.8	1.70

Table 5.2: The analysis conditions for dysprosium targets, namely the neutron separation energy S_n of the product nucleus, the range of sum energies used in the data processing (E_Σ) and the critical energy $E_{\rm crit}$ used in simulations.

the first resonance at energy of 5.44 eV. It was recognized that this resonance suffers from the effect of detection of more than one cascade within the preset time window. The experimental $E_n \times E_{\rm sum}$ spectrum exhibits the excess of counts with $E_{\rm sum} > 10$ MeV at neutron energies close to the resonance energy of 5.44 eV

when compared to the neutron energies lower than 4.5 eV and higher than 6 eV, see Fig. 5.10.

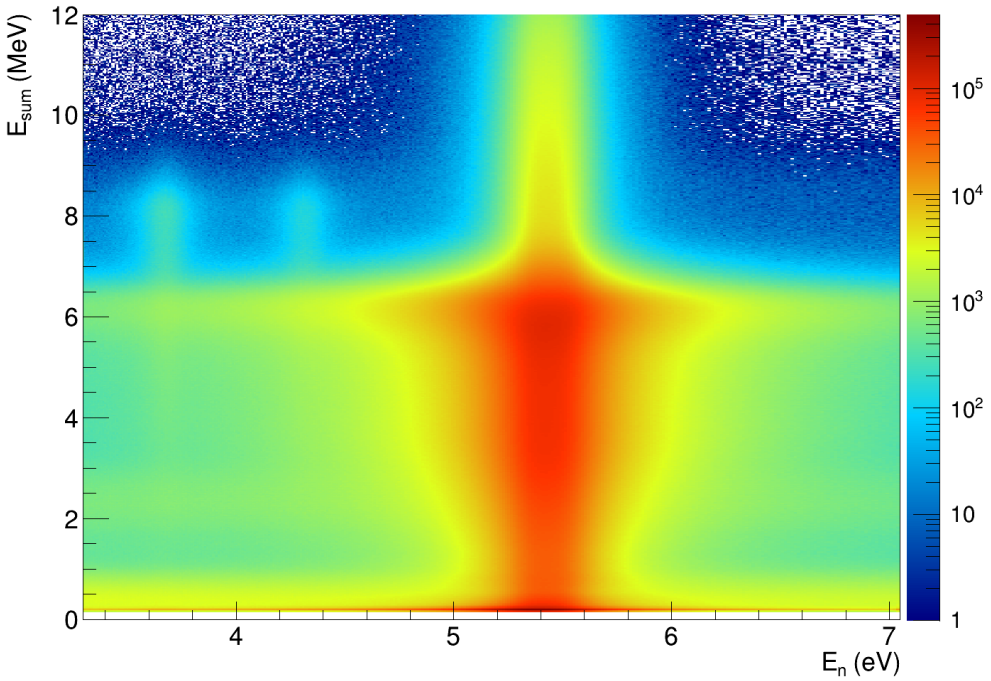

Figure 5.10: The experimental $E_n \times E_{\text{sum}}$ spectrum for the first ^{162}Dy resonance in the $^{162}\text{Dy}(n,\gamma)^{163}\text{Dy}$ reaction. The effect of detection of more than one cascade is clearly recognized, see text for explanation. The visible peaks at sum energy $E_{\text{sum}} \approx 8$ MeV at neutron energy $E_n = 3.68$ and 4.33 eV are the resonances of ^{161}Dy.

The fabrication of the *mean experimental MSC spectra* is described in App. B. The mean experimental MSC spectra for $M = 2 - 4$ of even Dy products are shown in Fig. 4 of App. B. The mean experimental MSC spectrum for $M = 2$ of ^{163}Dy product is shown in Fig. 5.11 together with the experimental MSC spectra extracted for the different intervals of neutron energies in the vicinity of the first resonance to illustrate the effect of detection of more than one cascade within the preset time window on the shape of the experimental MSC spectrum. It should be noted that the assumption of normally distributed experimental MSC intensities breaks down at high energies ($E \gtrsim 5$ MeV in case of ^{163}Dy). The different fluctuations are expected, because these parts of the spectra correspond to the few primary transitions feeding the low-lying levels. The distribution of experimental MSC intensities is then asymmetric and reflects the PT fluctuations of primary transitions.

In the comparison with simulated MSC spectra the uncertainty of I_{exp} as determined from the maximum likelihood fit, see Eq. (1) in App. B, is displayed as full rectangle, while the error bar represents the width of distribution of experimental MSC intensities and is drawn as $I_{\text{exp}} \pm \sigma_{\text{exp}}$.

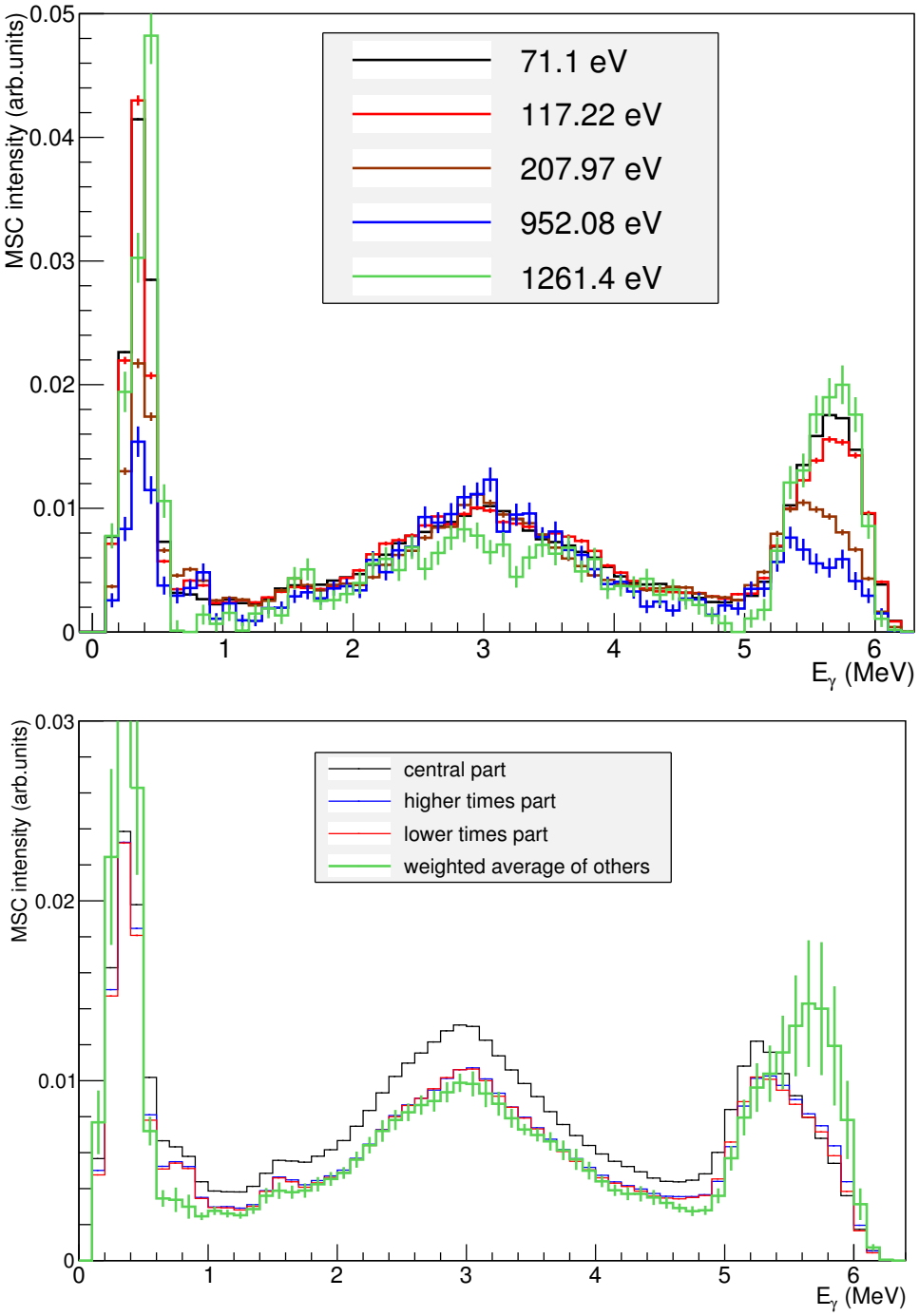

Figure 5.11: The $M = 2$ experimental MSC spectra for the $^{162}\mathrm{Dy}(n,\gamma)^{163}\mathrm{Dy}$ reaction. Top – the MSC spectra for 5 resonances included in our analysis. The resonance energies are indicated. Bottom – the MSC spectra of the first resonance at 5.44 eV are compared to the mean experimental MSC spectra of other resonances (green) drawn as $I_{\mathrm{exp}} \pm \sigma_{\mathrm{exp}}$. The effect of detection of more than one cascade is illustrated. The spectrum labeled cental part corresponds to neutron energies $E_n = 5.245 - 5.605$ eV, the higher times part to $E_n = 4.550 - 5.100$ eV and the lower times part to $E_n = 5.800 - 6.200$ eV.

Chapter 6

Results and Discussion

The information on level density and photon strength functions, in particular on scissors mode, was obtained by a trial-and-error approach of comparing the experimental and simulated spectra. Futher selection of model combinations was performed using the simulated and experimental average radiative width.

6.1 TSC Experiments

The experimental spectra of sum energies are shown in Figs. 5.2 and 5.3 for ^{156,158}Gd, respectively. The experimental TSC spectra gathered with a high resolution of HPGe detectors, see Fig. 5.4, enabled us to impose limits on spin and parity of some of the low-lying levels, see Figs. 1 and 2 of App. A. The results are listed in Tab. I of App. A, the ones for ^{158}Gd were included in the latest evaluated nuclear structure data file [132] (ENSDF).

The neutron separation energies are 8.536 and 7.937 MeV for ^{156,158}Gd, respectively. The spin and parity of the capturing state in thermal neutron capture is $J^\pi = 2^-$ for both isotopes due to the presence of resonances at very low energies (0.0268 and 0.0314 eV in ^{155,157}Gd, respectively [133]).

The data gathered during the TSC measurements enabled us to retrieve TSC spectra for 5 TSC final levels in each nucleus. The levels have spin and parity $J^\pi = 0^+, 2^+$ and 4^+ in ^{156}Gd and $0^+, 2^+, 4^+, 1^-$ and 3^- in ^{158}Gd. For the comparison with simulations the TSC spectra were binned into bins with width of 100 keV.

Taking into account the SM parameters determined in the MSC analyses [100, 101], namely $E_{\mathrm{SM}} \approx 2.9$ MeV, the TSC spectra could have been expected to have lower sensitivity to the PSFs, specifically to the SM strength, compared to the measurement of ^{162}Dy target [96, 97]. Therein it was shown that the sensitivity is enhanced for the final state that can be fed by the $M1 - M1$ cascades with the cascade energy close to $2E_{\mathrm{SM}}$. There is no TSC final level that would satisfy these conditions in ^{156}Gd, because all TSC final levels have positive parity and thus are dominantly fed by $E1 - M1$ or $M1 - E1$ TSCs. There are two negative parity TSC final levels in ^{158}Gd, but the energy of TSCs feeding these levels is $\gtrsim 6.9$ MeV, which is considerably higher than $2E_{\mathrm{SM}} \approx 5.8$ MeV, and the TSC spectra for these final levels exhibit higher uncertainties, see Fig. 5 of App. A.

This expectation was confirmed during the analysis. Consequently, the main result of the TSC analysis regarding the PSFs is that the TSC spectra are re-

produced by the PSFs determined in the MSC analyses [100, 101], specifically with the $E1$ PSF given by the KMF or MGLO ($k_0 \approx 2$) model and with the composite $M1$ PSF with the SM parameters $E_{\mathrm{SM}} \approx 2.9$ MeV, $\Gamma_{\mathrm{SM}} \approx 1.0$ MeV and $\sigma_{\mathrm{SM}} \approx 0.2$ mb and a SP strength $S_{\mathrm{SP}}^{(M1)} \approx 2 \times 10^{-9}\mathrm{MeV}^{-3}$.

6.2 MSC Experiments

As the main results for the even dysprosium nuclei were published in App. B, we focus here on the ^{163}Dy results. Some details concerning the LD models in the analysis of even isotopes are also discussed. We should note here that we do not explicitly discuss the G-C LD model. The matching energy E_x in the G-C LD model from the RIPL parametrization [33] is for odd isotope very close to neutron separation energy S_n and for even isotopes $E_x \gtrsim (S_n - 2)$ MeV, futhermore the parameters of CT formula within the G-C LD model from Ref. [33] are very close to the parameters of CT LD model from Ref. [32] making the models very similar. Consequently, the conclusions from the simulations with G-C LD model according to RIPL database [33] are the same as for the CT LD model according to von Egidy and Bucurescu [32].

During the search for an acceptable description of the mean experimental MSC spectra for all three isotopes, we have simulated one nuclear realization ($I = 1$) within each of $K = 20$ nuclear suprarealizations, i.e. a set $\{\omega_{1k}\}_{k=1}^{20}$. The results of simulations, plotted as a gray band, are compared in Figs. 6.1-6.14 with the mean experimental MSC spectra. The gray band is centered at the average of the set of simulated MSC intensities $\{I_{1k}\}_{k=1}^{20}$ and has a width of two standard deviations of the set. These fluctuation corridors from simulations should be, in general, broader than those for experimental spectra – the experimental ones rather correspond to the fluctuations obtained from simulations of number of nuclear realizations within a certain nuclear suprarealization $\theta_{k'}$, i.e. from a set $\{\omega_{ik'}\}_{i=1}^{I}$.

To verify this expectation and to compare the experimental fluctuations to properly simulated counterparts, we have performed the *extended simulations* of $K = 50$ nuclear suprarealizations with $I = 50$ nuclear realizations within each suprarealization. This comparison is meaningful only for the combinations of PSF and LD models that yield satisfactory description of the mean experimental MSC spectra. Futhermore, the extended simulations are very time consuming, so they were performed only for a couple of combinations of PSF and LD models for the ^{162,164}Dy. The results are presented in Sec. VI. of App. B. Despite the fact that we performed several thousands simulations for ^{163}Dy, we have not been able to reach better description of the mean experimental MSC spectra than presented in Fig. 6.1, so the extended simulations were postponed.

6.2.1 LD in Even Dysprosium Isotopes

The main result, as presented in App. B, is the clear preference of BSFG model, see Figs. 7 of App. B and 6.2, over the CT, see Fig. 6.3, and G-C models and the HFB calculation of LD. The simulations using the BSFG formula with parameters of either work by von Egidy and Bucurescu [31, 32] and with the SMMC LD [45] are practically identical, compare Figs. 7 of App. B, 6.2 and 6.4. The two

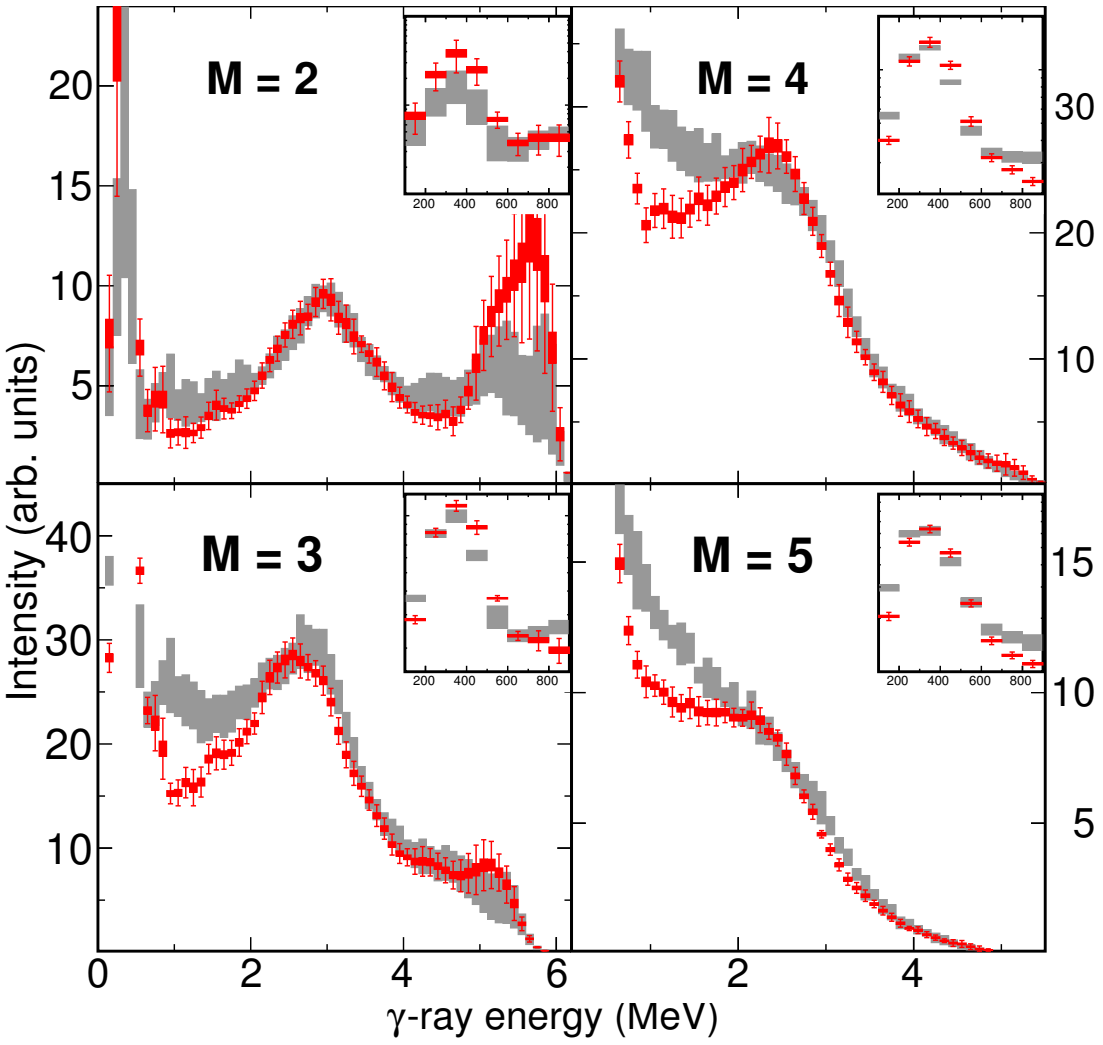

Figure 6.1: Comparison of ^{163}Dy mean experimental MSC spectra with simulations using the BSFG LD model, MGLO $E1$ PSF model and the composite $M1$ PSF model. The k_0 and $M1$ PSF parameters were adjusted to best describe the mean experimental MSC spectra yielding $k_0 = 4$, $E_{\mathrm{SM}} = 3.1$ MeV, $\Gamma_{\mathrm{SM}} = 1.0$ MeV, $\sigma_{\mathrm{SM}} = 0.6$ mb. The insets show the low-energy parts of the spectra, note that in the insets the γ-ray energy axis is in keV and the Intensity axis is in logarithmic scale. The full red rectangles show the mean experimental MSC intensities I_{exp} with their uncertainties coming from the maximum likelihood fit. The red error bars represent the width of distribution of experimental MSC intensities, drawn as $I_{\mathrm{exp}} \pm \sigma_{\mathrm{exp}}$, see Sec. 5.2.3. The gray band corresponds to the result of simulations drawn as a two standard deviation corridor centered at the average MSC intensity, for details see Sec. 4.3.

parametrizations of von Egidy and Bucurescu differ mainly in the spin distribution, namely by the inclusion of the even-odd spin staggering and by the form of spin cut-off parameter σ. The SMMC LD is the only one with parity distribution different from $g(+) = g(-) = \frac{1}{2}$.

For the practical reasons and because of the similarities discussed in Secs. 2.3, 2.4 and 2.5 the simulations using SMMC LD [45] were performed using the BSFG formula with parameters of von Egidy and Bucurescu [32], the spin distribu-

tion with the spin-cutoff parameter from the same work and with the even-odd spin staggering vanishing at 4 MeV and with the parity distribution given by Eq. (2.20).

6.2.2 LD in ^{163}Dy

The prefered LD model is the BSFG formula with the parametrization of Ref. [32]. The best overall description of the mean experimental MSC spectra was found in combination with the MGLO $E1$ PSF model and the composite $M1$ with adjusted SM parameters, see Fig. 6.1. The simulations with older parametrization [31] display an overprediction of higher ($M \geq 5$) multiplicities, see Fig. 6.5. The preference of the BSFG formula is consistent with the results for even dysprosium isotopes.

We were not able to adjust the $M1$ PSF in conjuction with any $E1$ PSF and the CT LD model to achieve a satisfactory matching of the mean experimental MSC spectra, see e.g. Fig. 6.6. We conclude that the CT LD model is inappropriate for the ^{163}Dy. This conclusion is affirmed by the comparison between simulated and experimental average radiative width, see Sec. 6.2.6.

As in the case of older parametrization of the BSFG LD model, the simulations with the HFB LD calculation overpredict higher ($M \geq 5$) multiplicities, see e.g. Fig. 6.7.

6.2.3 $E1$ PSF in ^{163}Dy

Because no (γ,xn) data are available for Dy isotopes, the GEDR parameters from nearby nucleus ^{160}Gd [134] were used. This seems to be fully justified as the GEDR parameters are expected to vary smoothly with A for nuclei with similar deformation. Furthermore, the shape of $E1$ PSF models at $E_\gamma \lesssim S_n$, i.e. in the region of our interest, is, within uncertainties of the GEDR parameters, almost indistinguishable when the GEDR parameters are taken from the fit of (γ,xn) experimental data for different isotopes. Specifically, we inspected the ^{154}Sm, ^{156}Gd, ^{160}Gd and ^{165}Ho GEDR parameters [134]. The highest deviation of at most 10% from the $S^{(E1)}$ with ^{160}Gd GEDR parameters was observed with the ^{165}Ho GEDR parameters for all $E1$ PSF models.

Despite the enormous number of tested model combinations, probably the best possible description of the mean experimental MSC spectra was achieved only with the MGLO model after appropriate adjustion of the $M1$ PSF, see Fig. 6.1. The value of k_0 was determined to be $k_0 \approx 3-4$. For the other $E1$ PSF models introduced in Sec. 3.1 the description was always worse, the examples of simulation with the SLO, KMF and MLO2 models are shown in Figs. 6.8, 6.9 and 6.10, respectively. The observed trend is that (i) the model combinations of $E1$ PSF models that are lower than MGLO model, such as KMF model, overpredict the mean experimental MSC spectra for higher $M \gtrsim 4$ multiplicities when adjusted to $M = 2$ and 3 spectra and (ii) the model combinations of $E1$ PSF models that are higher than MGLO model, such as SLO and MLO2 models, underestimate the midpart of $M = 2$ spectrum when adjusted to $M = 3$ spectrum.

6.2.4 $M1$ PSF in ^{163}Dy

The parameters of the SM and the $S_{\mathrm{SP}}^{(M1)}$ were adjusted separately for combinations of LD and $E1$ PSF models to find the best possible description of mean experimental MSC spectra. For a given LD and $E1$ PSF model, the values of the SM parameters can be constrained by the requirement of a simultaneous matching of the bumps between $E_\gamma \approx 2-4$ MeV in the mean experimental MSC spectra of multiplicities $M = 2-4$ and the shapes of the high energy parts of the $M \geq 3$ spectra. We were never able to reproduce the dip at energy $E_\gamma \approx 1$ MeV in the experimental MSC spectra of $M \geq 3$.

The disagreement in the very low energy ($E_\gamma < 900$ keV) parts of MSC spectra, shown in the insets of Figs. 6.1-6.14, and the underestimation of measured intensities in the region of high energy primary transitions $E_\gamma \gtrsim 5$ MeV in the $M = 2$ MSC spectra might point to an inadequate description of the PSF at these γ-ray energies. On the other hand, the assumption of normally distributed MSC intensities in the high energy range might be unreasonable – the distribution might be asymmetric as discussed in Sec. 5.2.3.

As already mentioned, the best possible description was achived only for the combination of MGLO $E1$ model with the BSFG LD model with parameters from Ref. [32]. The prefered values of k_0 are between $k_0 \approx 3$, see Fig. 6.11, and $k_0 \approx 4$, see Fig. 6.1. The simulations with these values of k_0 yield the average radiative widths compatible with the experimental value within uncertainties, see Tab 6.2.

The adjusted parameters of the SM are given in Tab. 6.1, the intervals of allowed values are determined from the simulations with $k_0 = 3-4$. The strength of the SM listed in Tab. 6.1 corresponds to the interval $\sigma_{\mathrm{SM}} = 0.6 - 0.8$ mb. The problems with finding the model combination, that would precisely describe the mean experimental MSC spectra, might be related to the form of the composite $M1$ PSF model. This model has four adjustable parameters and exhibits no T_f-dependence. If we are unable to reach a model close to reality within our testing space, we can never find a satisfactory description. It is possible to enlarge the testing space by introducing for example more complicated structure of the SM or the T_f-dependence of the components of $M1$ PSF.

Isotope	E_{SM} (MeV)	Γ_{SM} (MeV)	$\sum B(SM)$ (μ_N^2)
^{162}Dy	2.8 - 3.0	1.0 - 1.4	2.3 - 4.3
^{163}Dy	3.0 - 3.1	0.8 - 1.2	5.4 - 9.0
^{164}Dy	2.8 - 3.0	1.0 - 1.4	5.3 - 7.5

Table 6.1: The parameters of the scissors mode reproducing both the mean experimental MSC spectra and the average radiative width as deduced in our analysis.

The single particle strength is limited to $S_{\mathrm{SP}}^{(M1)} \lesssim 1 \times 10^{-9}\mathrm{MeV}^{-3}$, there was no SP strength in the simulations presented in Figs. 6.1,6.5 and 6.11.

From the comparison of adjusted SM parameters given in Tab. 6.1, namely the observed strength of SM in ^{164}Dy, it is evident that we did not observe the even-odd effect in the SM strength as in the gadolinium isotopical chain [77, 100, 101]. It is worth reminding that the results on $S_{\mathrm{SP}}^{(M1)}$ in even isotopes, as given in

App. B, are very different and might point to more complicated behavior of $M1$ PSF as a whole.

6.2.5 Low-energy Enhancement of Dipole PSF

We made several tests of a possible influence of the low-energy enhancement on the decay of $^{162-164}$Dy. The enhancement following the Brink hypothesis was checked. None of the simulations with a low-energy enhancement led to a satisfactory description of mean experimental MSC spectra, see Fig. 6.12 and Fig. 11 of App. B. In our simulations we adopted the exponential form of low energy enhancement with parameters deduced from the ^{152,4}Sm(p,dγ) data [104] scaled down to the experimental data from ^{3}He-induced reactions [63, 98, 99]. Despite the indications about its $M1$ character, see Sec. 3.4.3, the enhancement was tested with a pure $E1$ or $M1$ character and as a 1:1 combination to cover all possibilities.

In order to test the PSF that is still consistent with the Oslo-type data but falls to zero for $E_\gamma \to 0$, we performed simulations with low-energy resonance. The parameters of this resonance were determined to describes the trend of the data from ^{152,4}Sm(p,dγ) experiment [104] scaled down to the experimental data from ^{3}He-induced reactions [63, 98, 99]. We tested the same possibilities of $E1$ or $M1$ nature as in the case of the exponential enhancement. The result of such simulation for ^{164}Dy is shown in Fig. 11 of App. B. None of these simulations led to a satisfactory description of our data. The common result of these simulations is a strong, unrealistic preference of higher multiplicities.

6.2.6 Average Radiative Width

As mentioned in Sec. 4.4, the simulated average radiative width $\overline{\Gamma}_\gamma$ is in general the only detector-independent quantity simulated with the DICEBOX code that depends on the absolute values of the PSFs. As such it can be used to further restrict the acceptability of the model combinations found from the comparison of simulated spectra with their experimental counterparts.

Although the majority of LD and $E1$ PSF models can be rejected just from the comparison of mean experimental and simulated MSC spectra, the resulting $\overline{\Gamma}_\gamma$ can provide additional support for such conclusions. The simulations using the CT LD model give a $\overline{\Gamma}_\gamma$ comparable with the experimental value only when the SLO model of $E1$ PSF is used, see Tab. 6.2. However, for this combination of LD and $E1$ PSF models we were unable to adjust the $M1$ PSF to reproduce the mean experimental MSC spectra.

For other $E1$ models the ^{162,164}Dy simulations with CT LD model could be rejected solely by the comparison of $\overline{\Gamma}_\gamma$. Futher conclusions for simulations with BSFG model are enabled by a good precision of the experimental average radiative widths and too low simulated values of $\overline{\Gamma}_\gamma$, see Tab. II of App. B.

In case of ^{163}Dy the uncertainty of the experimental $\overline{\Gamma}_\gamma$ is 18%, which limits the discrimination power of average radiative width, see Tab. 6.2. The model combinations that well describe the mean experimental MSC spectra, namely the BSFG LD model in conjuction with the MGLO $E1$ PSF model, reproduce also the experimental average radiative width. On the 3σ level only the combination

of CT LD model and KMF $E1$ PSF model can be rejected.

$\overline{\Gamma}_\gamma$ (meV)	LD	
PSF	BSFG	CT
SLO	191(8)	117(7)
KMF	76(2)	45(2)
MGLO($k_0 = 3$)	90(3)	52(3)
MGLO($k_0 = 4$)	104(4)	62(4)
Experiment	112(20)	

Table 6.2: The experimental average radiative width of s-wave neutron resonances compared to the simulated radiative width. The simulations are labeled with the used LD and $E1$ PSF model, the $M1$ PSF was adjusted as described in Sec. 6.2.4. The experimental value is taken from [36].

6.3 Comparison with Other Experiments

6.3.1 TSC Data

The simulation based on the LD and PSFs models determined in the TSC analysis [96, 97] is compared to the mean experimental MSC spectra in Fig. 6.13. An acceptable description of the $M = 2$ mean experimental MSC spectra is achieved, but higher multiplicities $M \geq 3$ display an apparent disagreement. This disagreement is induced by the relatively low width of the SM $\Gamma_{\mathrm{SM}} = 0.6$ MeV, the situation is not salvaged by changing the parametrization of the BSFG LD model to neither of the recent ones [31, 32]. Motivated by this observation, the test with the TSC data is needed to check their consistency with the best possible model combination coming from the MSC analysis. Our expectation is that the model combination from TSC analysis as listed in [97] represents one particular solution from the set of possible model combinations that are able to describe the TSC data.

6.3.2 NRF Data

To compare our results with the summed $M1$ strength as determined in NRF experiments we have integrated all $M1$ strength in the energy range $2.7 - 3.7$ MeV. The range of values obtained for ^{163}Dy using the composite model of $M1$ PSF $S^{(M1)} = S^{(M1)}_{\mathrm{SM}} + S^{(M1)}_{\mathrm{SF}} + S^{(M1)}_{\mathrm{SP}}$ is $3.4 - 5.4$ μ^2_N, which is compatible with the summed $M1$ strength of 3.30(36) μ^2_N [95]. We should again note that in case of ^{163}Dy the SM contributes between 80 and 90% of the strength in the composite $M1$ PSF model. The tail of SF resonances and the possible SP strength are responsible for the rest of this summed $M1$ strength.

6.3.3 Oslo Results

The mean experimental MSC spectra are compared to the simulations based on the Oslo results form Refs. [35, 99] in Fig. 6.14.

The SM parameters from the ^{3}He-induced reaction in ^{163}Dy were determined in Ref. [99] – the position $E_{\mathrm{SM}} = 2.81(9)$ MeV, which is lower yet compatible with our result, the width $\Gamma_{\mathrm{SM}} = 0.86(19)$ MeV, which nicely agrees with our result, and the $\sigma_{\mathrm{SM}} = 0.72(12)$ mb in excellent agreement with our result.

Contrary to the restricted energy range used to compare all $M1$ strength with the NRF data, the total SM strength can be compared to the Oslo results – excellent agreement is found between our interval of allowed values $\sum B(SM) = 5.4 - 9.0\ \mu_N^2$ and the strength of $7.1(20)\ \mu_N^2$ from Ref. [99].

This overall good agreement on the SM parameters is in contradiction with the comparison of MSC spectra in Fig. 6.14 and with the comparison of sum of dipole PSFs as presented in Fig. 3.5, notice the difference between green data-points (Oslo) and blue curves (MSC). Judging by our very good description of the average radiative width as listed in Tab. 6.2, we conclude that the normalization of Oslo data is questionable and the agreement of the SM parameters might be coincidental in this case.

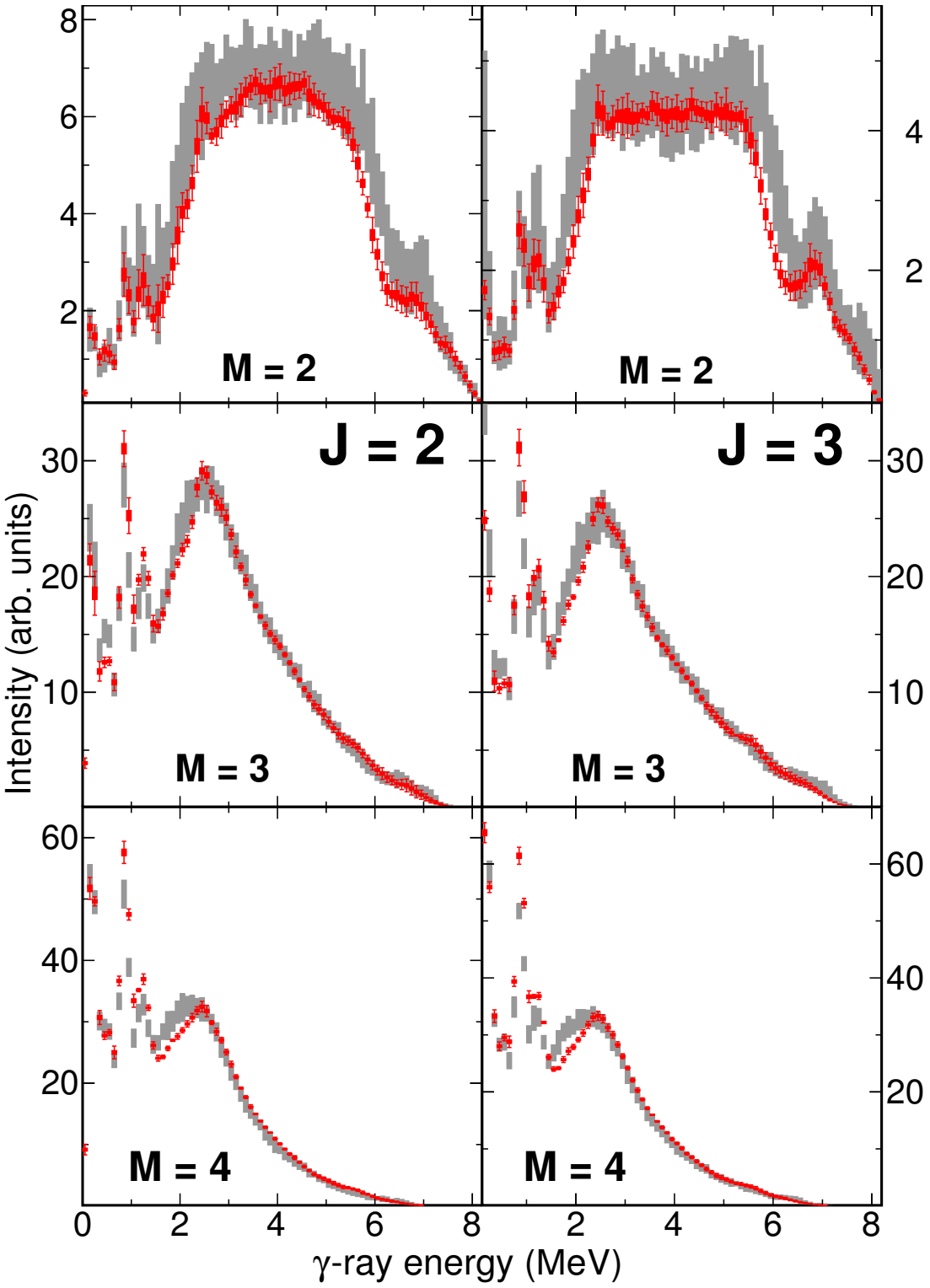

Figure 6.2: Comparison of ^{162}Dy mean experimental MSC spectra with simulations using BSFG LD model, MGLO $E1$ PSF model and the composite $M1$ PSF model. The k_0, SM and SP parameters were taken the same as in Fig. 7 of App. B with the SM width Γ_{SM} decreased by 0.1 MeV. The full red rectangles show the mean experimental MSC intensities I_{exp} with their uncertainties coming from the maximum likelihood fit. The red error bars represent the width of distribution of experimental MSC intensities, drawn as $I_{\mathrm{exp}} \pm \sigma_{\mathrm{exp}}$, see Sec. 5.2.3. The gray band corresponds to the result of simulations drawn as a two standard deviation corridor centered at the average MSC intensity, for details see Sec. 4.3.

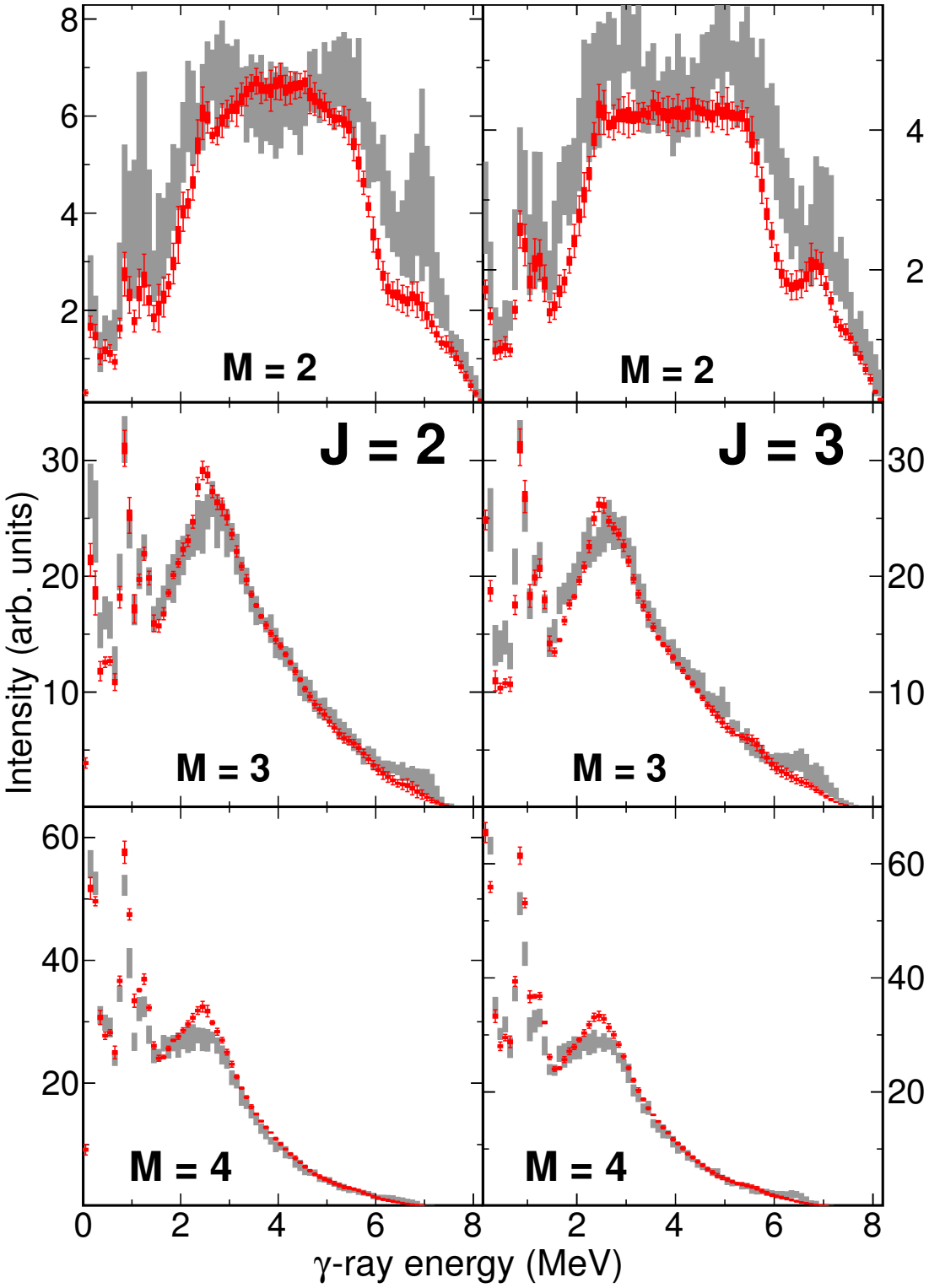

Figure 6.3: Comparison of ^{162}Dy mean experimental MSC spectra with simulations using the CT LD model, MGLO $E1$ PSF model and the composite $M1$ PSF model. The k_0, SM and SP parameters were adopted from simulations with BSFG LD that best described the mean experimental MSC spectra. For additional details see Fig. 6.2.

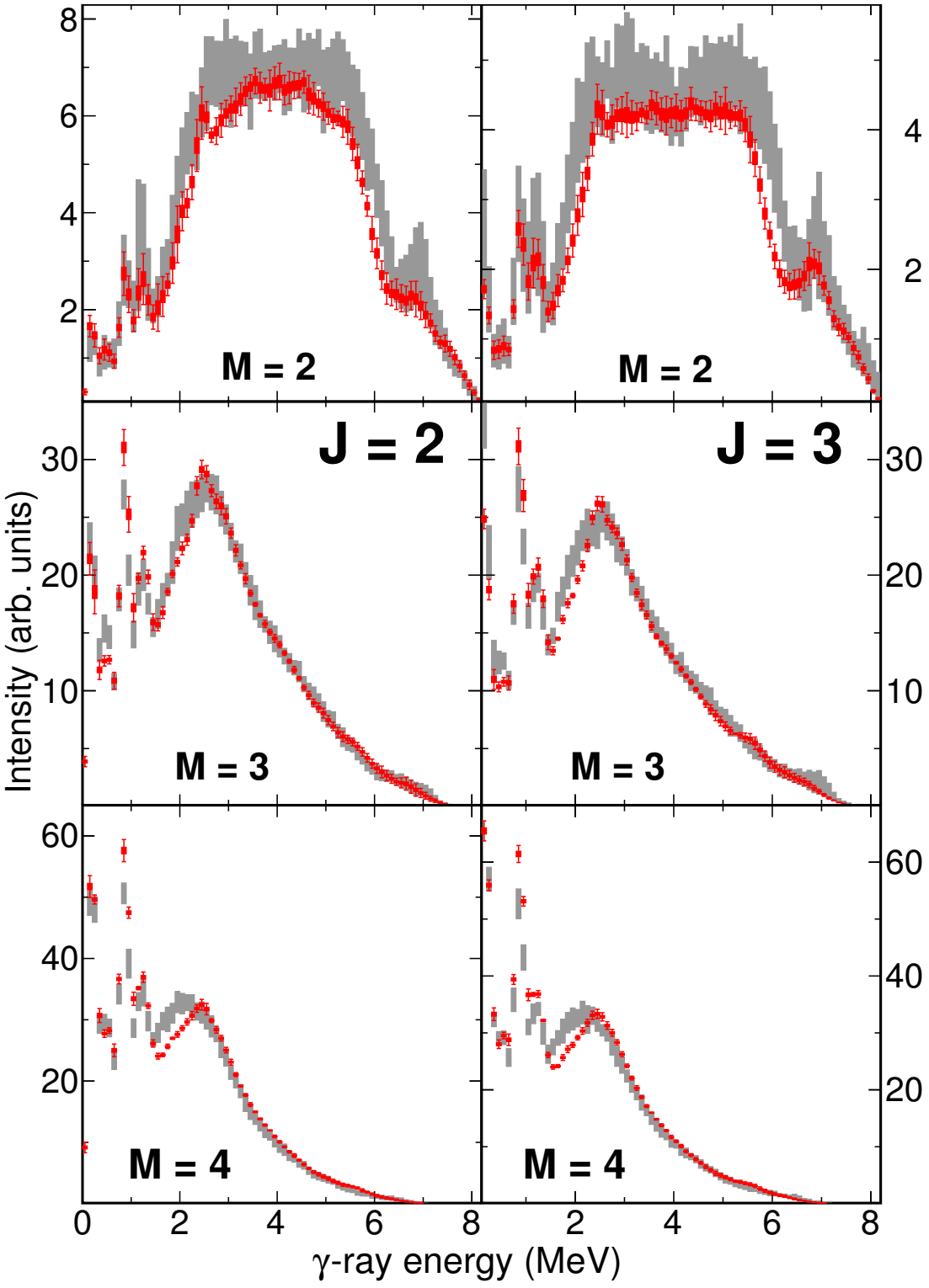

Figure 6.4: Comparison of ^{162}Dy mean experimental MSC spectra with simulations using the SMMC-like BSFG LD model, MGLO $E1$ PSF model and the composite $M1$ PSF model. The k_0, SM and SP parameters were adopted from simulations with BSFG LD that best described the mean experimental MSC spectra. For additional details see Fig. 6.2.

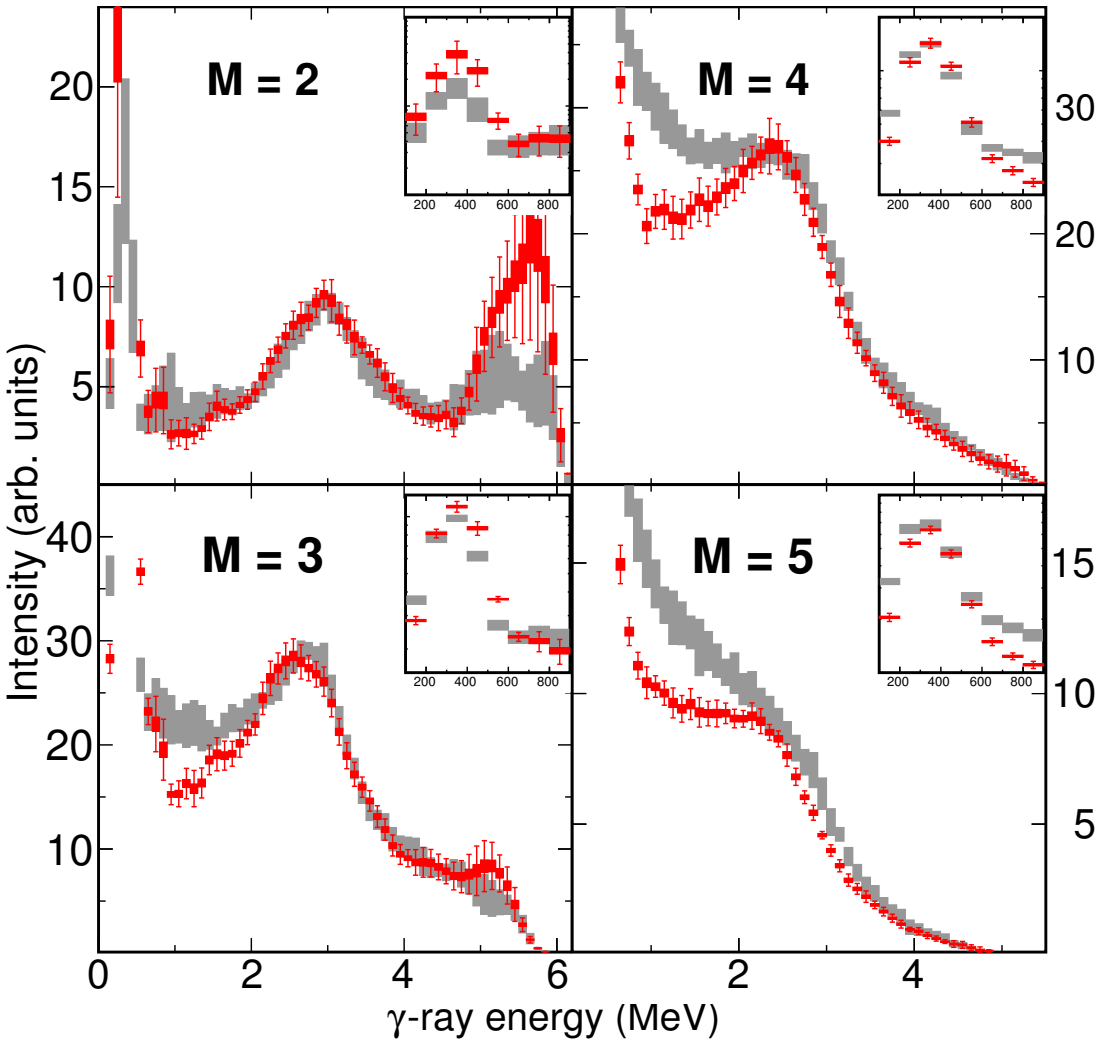

Figure 6.5: Comparison of ^{163}Dy mean experimental MSC spectra with simulations using the BSFG LD model, MGLO $E1$ PSF model and the composite $M1$ PSF model. The k_0 and $M1$ PSF parameters were adjusted to best describe the mean experimental MSC spectra yielding $k_0 = 4$, $E_{\mathrm{SM}} = 3.0$ MeV, $\Gamma_{\mathrm{SM}} = 1.0$ MeV, $\sigma_{\mathrm{SM}} = 0.8$ mb. For additional details see Fig. 6.1.

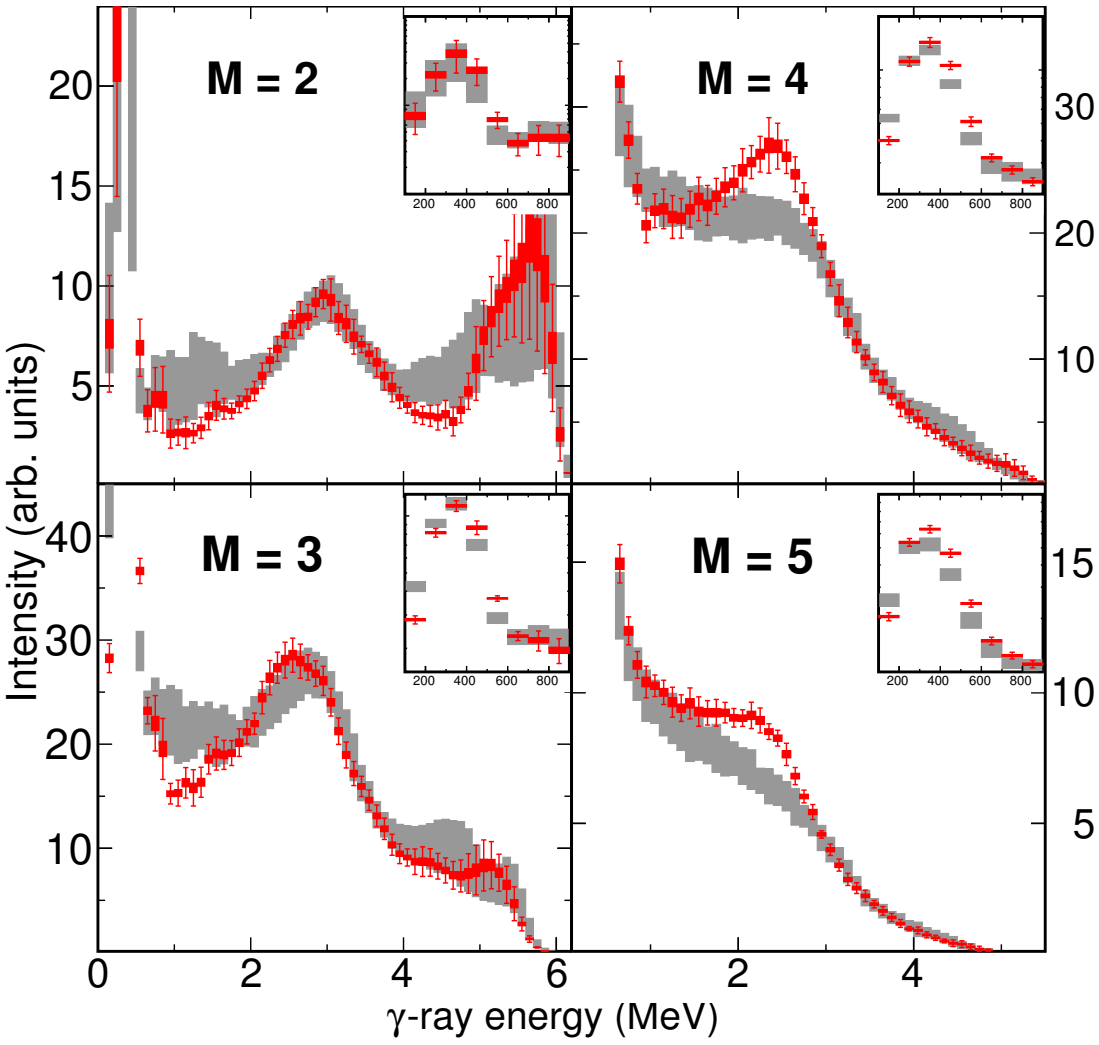

Figure 6.6: Comparison of ^{163}Dy mean experimental MSC spectra with simulations using the CT LD model, MGLO $E1$ PSF model and the composite $M1$ PSF model. The k_0 and $M1$ PSF parameters were kept identical to those in Fig. 6.1. For additional details see Fig. 6.1.

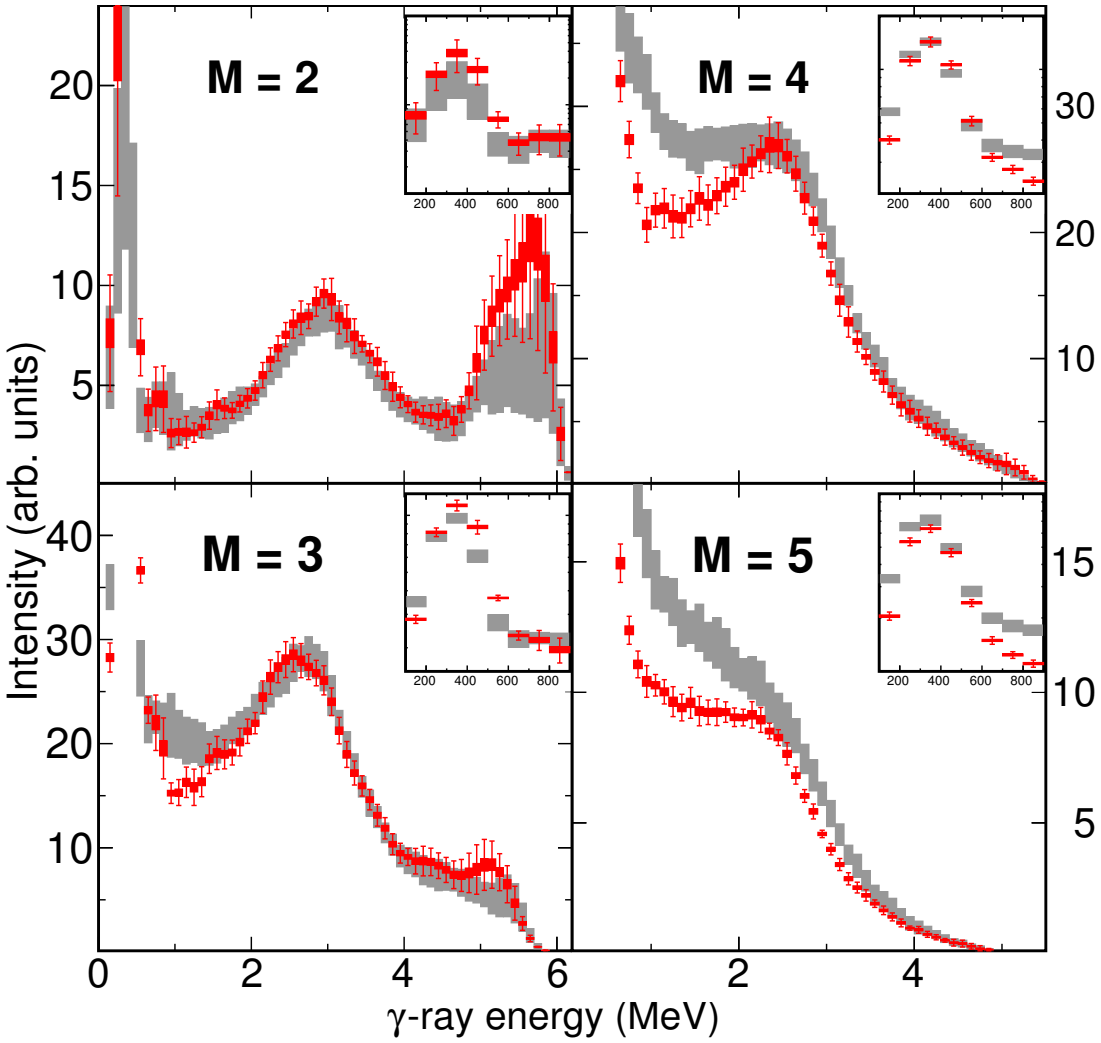

Figure 6.7: Comparison of ^{163}Dy mean experimental MSC spectra with simulations using the HFB LD calculation, MGLO $E1$ PSF model and the composite $M1$ PSF model. The k_0 and $M1$ PSF parameters were adjusted to described the midpart of $M = 2$ mean experimental MSC spectrum yielding $k_0 = 3$, $E_{\mathrm{SM}} = 3.0$ MeV, $\Gamma_{\mathrm{SM}} = 1.0$ MeV and $\sigma_{\mathrm{SM}} = 0.6$ mb. For additional details see Fig. 6.1.

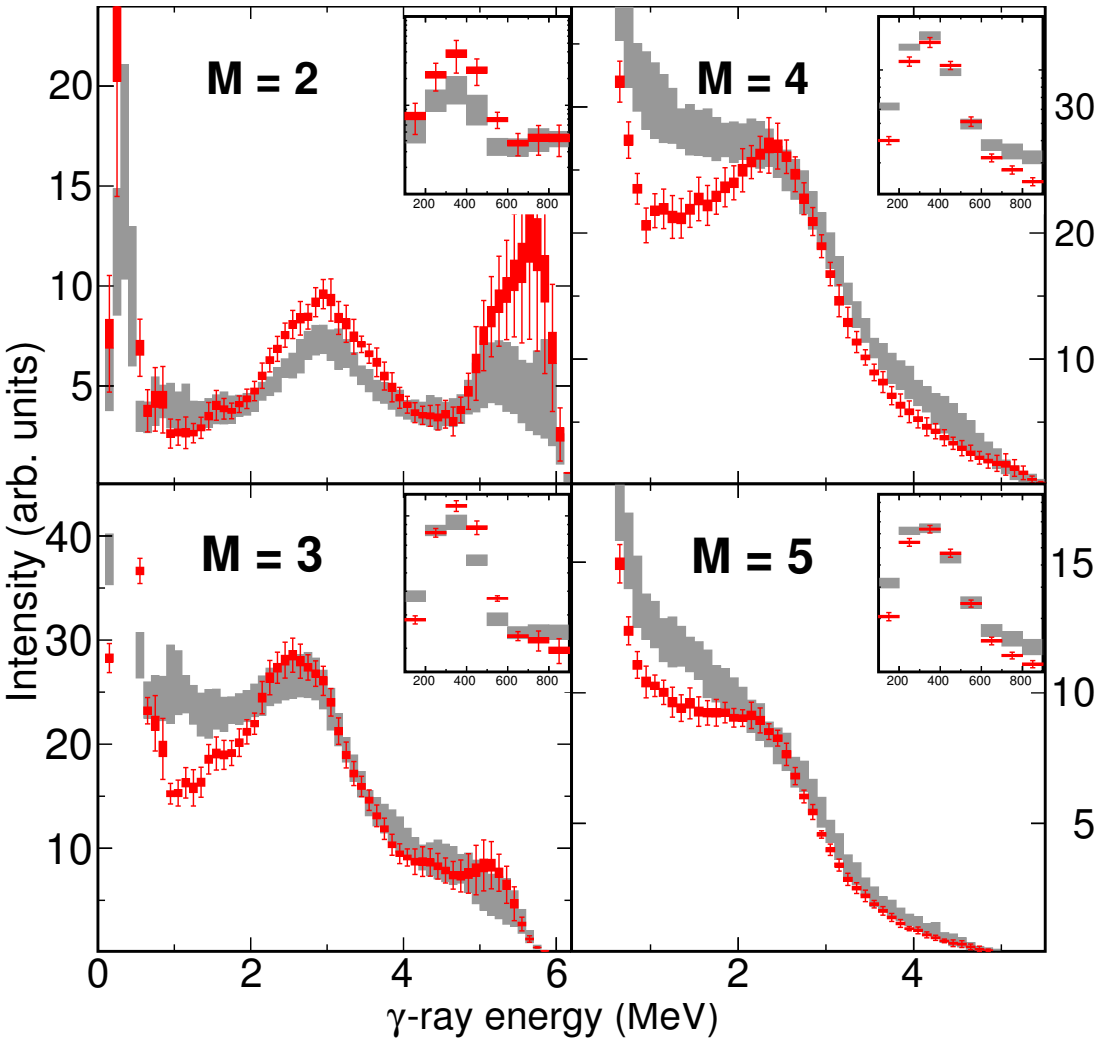

Figure 6.8: Comparison of ^{163}Dy mean experimental MSC spectra with simulations using the BSFG LD model, SLO $E1$ PSF model and the composite $M1$ PSF model. The SM parameters were adjusted to described the midpart of $M = 3$ mean experimental MSC spectrum. For additional details see Fig. 6.1.

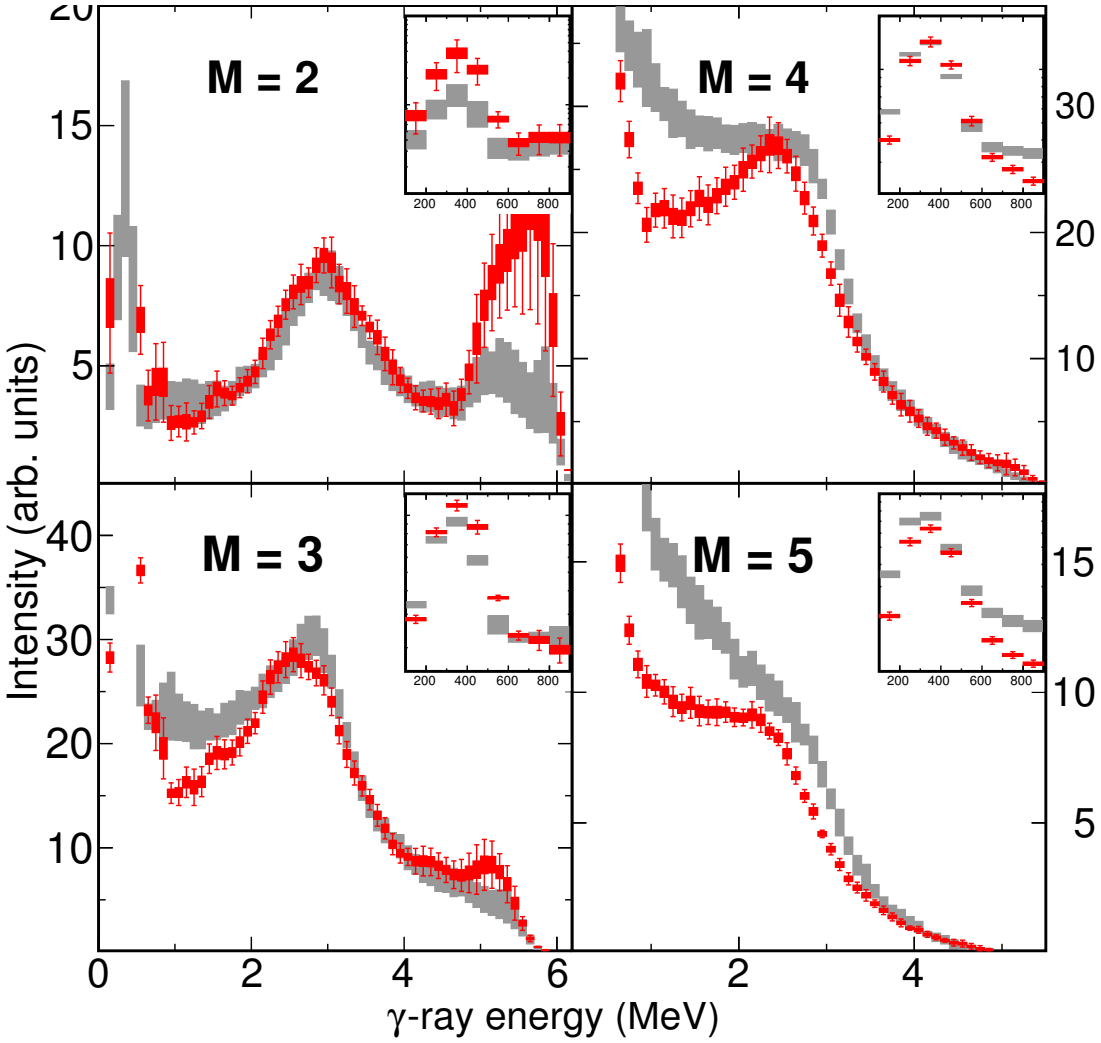

Figure 6.9: Comparison of ^{163}Dy mean experimental MSC spectra with simulations using the BSFG LD model, KMF $E1$ PSF model and the composite $M1$ PSF model. The $M1$ PSF parameters were adjusted to described the mid-part of $M = 2$ mean experimental MSC spectrum yielding $E_{\mathrm{SM}} = 3.0$ MeV, $\Gamma_{\mathrm{SM}} = 0.8$ MeV, $\sigma_{\mathrm{SM}} = 0.6$ mb and $S_{\mathrm{SP}} = 2 \times 10^{-9}\mathrm{MeV}^{-3}$. For additional details see Fig. 6.1.

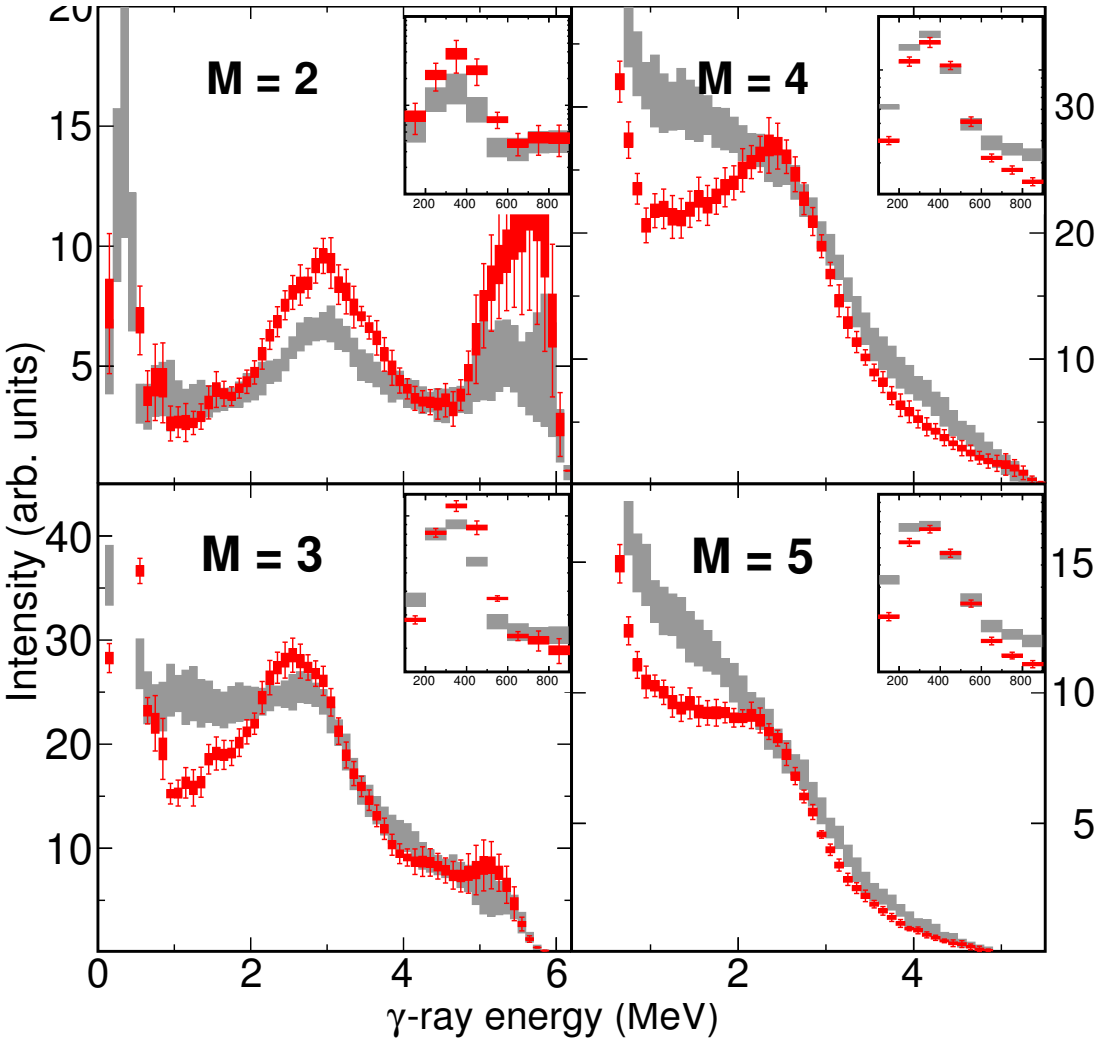

Figure 6.10: Comparison of ^{163}Dy mean experimental MSC spectra with simulations using the BSFG LD model, MLO2 $E1$ PSF model and the composite $M1$ PSF model. The $M1$ PSF parameters were taken identical to simulations in Fig. 6.1. For additional details see Fig. 6.1.

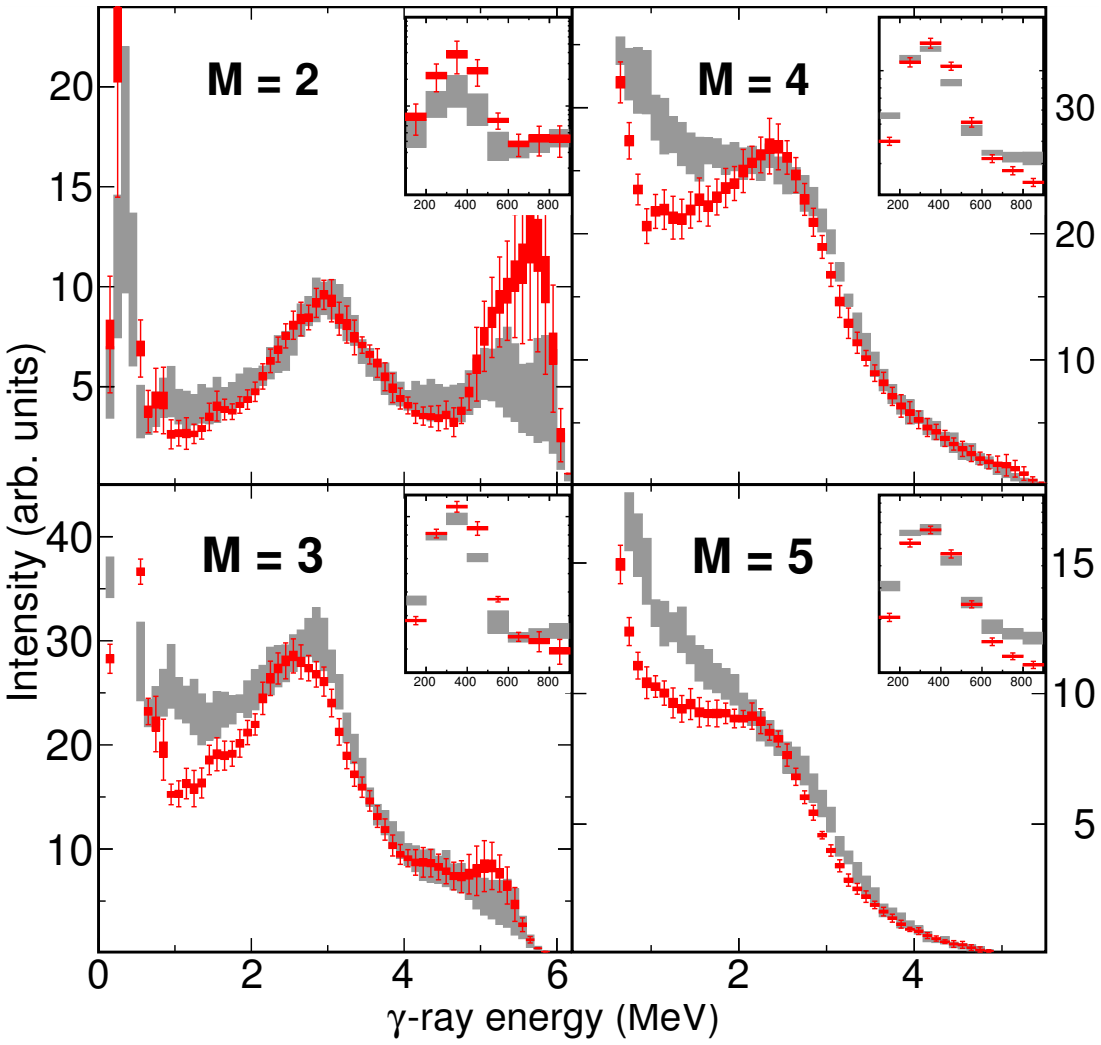

Figure 6.11: Comparison of ^{163}Dy mean experimental MSC spectra with simulations using the BSFG LD model, MGLO $E1$ PSF model and the composite $M1$ PSF model. The k_0 and $M1$ PSF parameters were adjusted to best describe the mean experimental MSC spectra yielding $k_0 = 3$, $E_{\mathrm{SM}} = 3.1$ MeV, $\Gamma_{\mathrm{SM}} = 1.0$ MeV, $\sigma_{\mathrm{SM}} = 0.6$ mb. For additional details see Fig. 6.1.

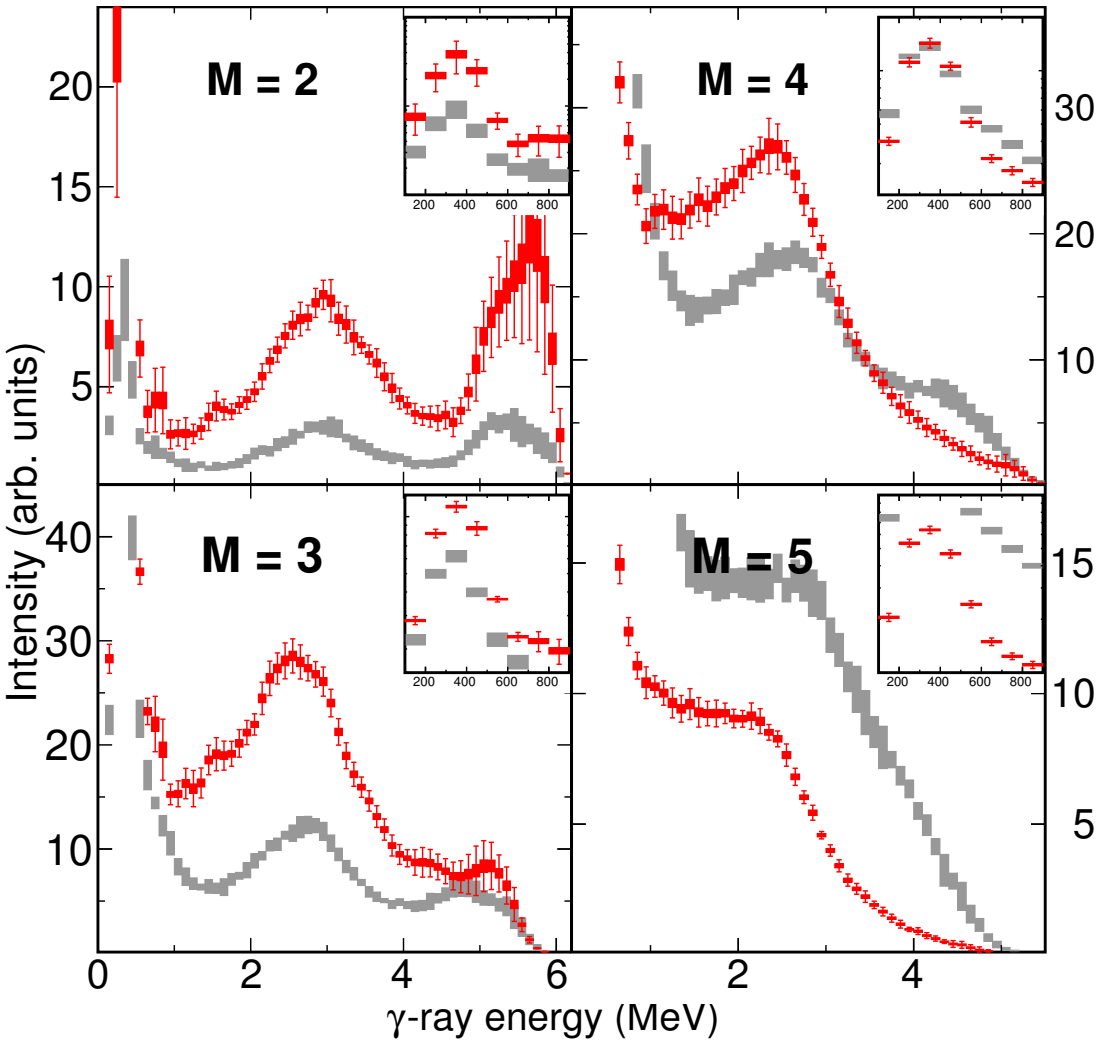

Figure 6.12: Comparison of ^{163}Dy mean experimental MSC spectra with simulations using the LD, $E1$ and $M1$ PSF models including the low-energy enhancement in $M1$ PSF in accord with the Oslo-type analysis [104]. The SM parameters were $E_{\mathrm{SM}} = 3.0$ MeV, $\Gamma_{\mathrm{SM}} = 1.0$ MeV and $\sigma_{\mathrm{SM}} = 0.6$ mb. For additional details see Fig. 6.1.

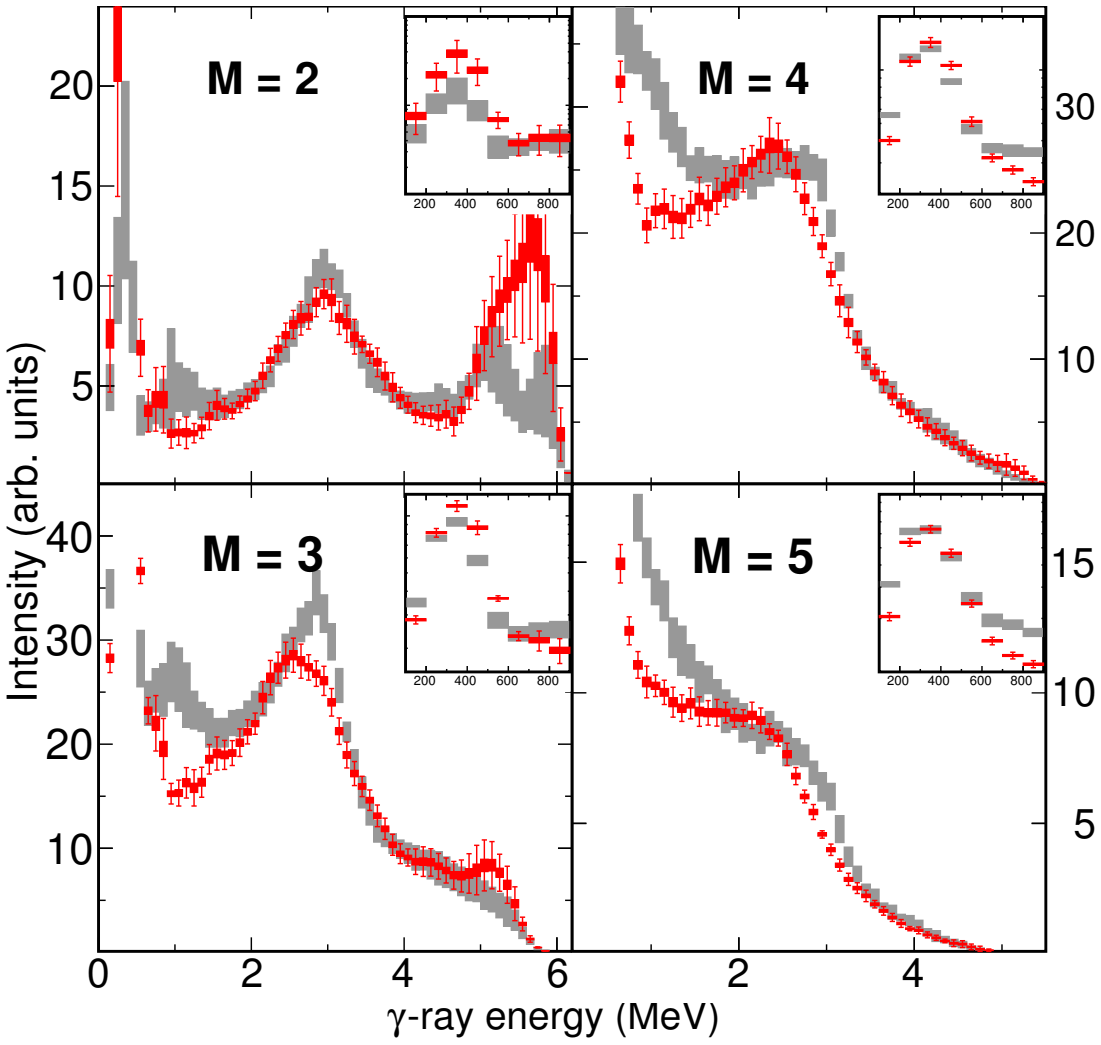

Figure 6.13: Comparison of ^{163}Dy mean experimental MSC spectra with simulations using the LD, $E1$ and $M1$ PSF models from the TSC analysis [96,97]. The SM parameters were $E_{\mathrm{SM}} = 3.0$ MeV, $\Gamma_{\mathrm{SM}} = 0.6$ MeV and $\sigma_{\mathrm{SM}} = 1.0$ mb. For additional details see Fig. 6.1.

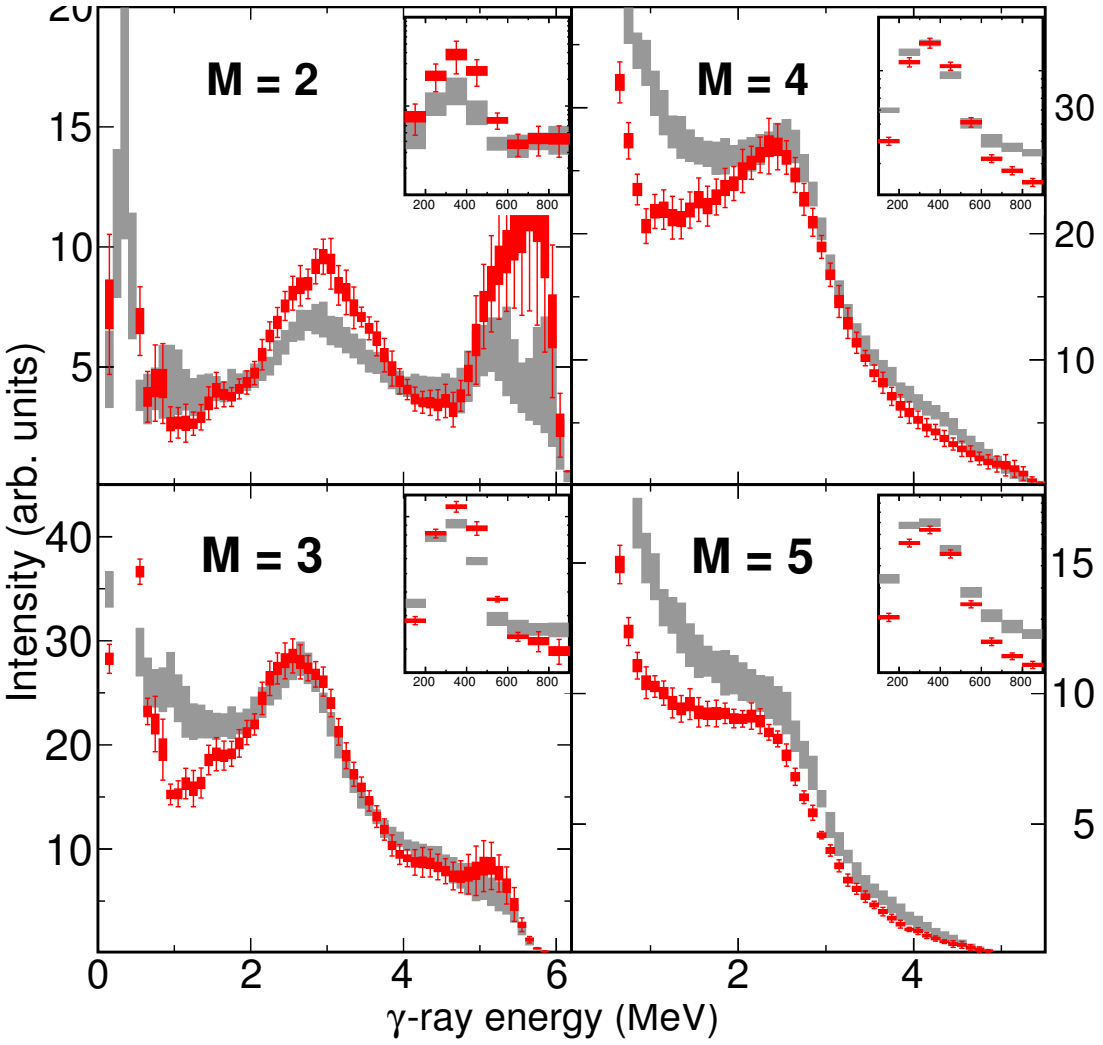

Figure 6.14: Comparison of ^{163}Dy mean experimental MSC spectra with simulations using the LD, $E1$ and $M1$ PSF models from the Oslo analysis [35, 99]. The temperature of KMF-T model was determined as $T = 0.3$ MeV, the SM parameters $E_{\mathrm{SM}} = 2.81$ MeV, $\Gamma_{\mathrm{SM}} = 0.86$ MeV and $\sigma_{\mathrm{SM}} = 0.72$ mb. For additional details see Fig. 6.1.

Chapter 7

Conclusions and Outlook

The coincidence data on γ cascades from radiative capture of thermal and resonance neutrons on well-deformed rare-earth nuclei were analysed within the statistical model of γ decay. Specifically, the spectra for two even gadolinium isotopes, measured by two-step γ cascades experimental setup at the research reactor LVR-15 in Řež, enabled a confirmation of preceding findings on level density and photon strength functions [77, 100, 101] deduced from the multi-step γ cascades experiments performed with DANCE calorimeter in LANSCE at LANL with these isotopes. The DANCE setup was also utilized to measure the multi-step γ cascades for three dysprosium isotopes. While the gadolinium data proved a consistency of results from two- and multi-step γ cascades measurements, the analysis of ^{163}Dy multi-step γ cascades encourages us to revisit the two-step γ cascades data [96, 97].

The common result for all analysed isotopes is the clear influence of the scissors mode on the decay of excited levels, which persists quite high in the excitation energy. The preference of the BSFG LD and the MGLO $E1$ PSF models is also a common feature. Despite the fact that the success of MGLO is likely achieved by the *ad hoc* adjustable parameter k_0, the prefered shape (and its change with excitation energy) of the $E1$ PSF was determined for all isotopes.

The dysprosium isotopes are the first isotopes that were analysed by the Oslo method [63, 98, 99], measured with the nuclear resonance fluorescence scattering [91–93, 95] and studied in the multi-step γ cascades experiments. Moreover, the two-step γ cascades data are available for ^{163}Dy [96, 97]. This enabled the direct comparison of results coming from these experimental techniques. With the exception of ^{164}Dy, it can be said that for even-even gadolinium and dysprosium isotopes the $M1$ strength determined by the Oslo method is the only one inconsitent with the results of the other methods. On the other hand, the nuclear resonance fluorescence scattering results for odd isotopes are very likely underestimating the $M1$ strength in well-deformed rare-earth nuclei, which is consistently found by at least a factor of 2 higher by all other techniques. Keeping in mind the determined values of the average radiative width, the comparison of dipole PSF from Oslo method and from multi-step γ cascades analyses hints to possible problems in normalization of ^{163,164}Dy Oslo data.

The ^{161}Dy(n,γ)^{162}Dy reaction was measured using an array of segmented HPGe clover detectors EXOGAM at the cold neutron beam facility PF1B of the Institut Laue-Langevin within the EXILL campaign [135]. After validating

the currently developed GEANT4 description of the setup, the models that best describe the MSC data are planned to be tested also on the EXILL data, that are ready for the comparison in the form analogous to the MSC data ($M = 2-4$) for several TSC final levels. The data for ^{155,157}Gd and ^{167}Er targets are also possibly available from the EXILL campaign [135] as well.

There is a wealth of MSC data measured by DANCE calorimeter and Total Absorption Calorimeter [136] installed at n_TOF facility at CERN [137], that are being analysed or waiting to be analysed. Within the DANCE collaboration, the MSC analysis for ^{168}Er compound is ongoing, it will provide another point of view to the applicability of the Statistical Model of γ decay through the comparison of measured and simulated population of 1.094 MeV K-isomer with halflife of ≈ 110 ns.

The results presented in this thesis confirm that at least the mean experimental quantities seem to be consistent with the predictions made within the Statistical Model of γ decay by appropriate choice of Level Density and Photon Strength Function models. The wealth and precision of the resonance experimental data enabled, for the first time, the analysis of fluctuations for a sizeable set of neutron resonances. The results, as puzzling as they are, will hopefully induce futher studies.

Bibliography

[1] J. Chadwick, Proc. Roy. Soc. A **136**, 692 (1932).

[2] J. Chadwick, Proc. Roy. Soc. A **142**, 1 (1933).

[3] E. Fermi *et al.*, Proc. Roy. Soc. A **146**, 483 (1934).

[4] E. Amaldi *et al.*, Proc. Roy. Soc. A **149**, 522 (1935).

[5] N. Bohr, Nature **137**, 344 (1936).

[6] N. Bohr, Science **86**, 161 (1937).

[7] O. R. Frisch and G. Placzek, Nature **137**, 357 (1936).

[8] G. Breit and E. Wigner, Phys. Rev. **49**, 519 (1936).

[9] H. Bethe and G. Placzek, Phys. Rev. **51**, 450 (1937).

[10] E. Fermi and E. Amaldi, La Ricercio Scientifica A **6**, 544 (1935).

[11] L. Szilard, Nature **136**, 849 (1935).

[12] O. R. Frisch, G. Hevesy and H. A. C. McKay, Nature **137**, 149 (1936).

[13] H. Bethe, Phys. Rev. **50**, 332 (1936).

[14] H. Bethe, Rev. Mod. Phys. **9**, 69 (1937).

[15] V. F. Weisskopf, Phys. Rev. **52**, 295 (1937).

[16] V. F. Weisskopf and D. H. Ewing, Phys. Rev. **57**, 472 (1940).

[17] T. Ericson, Adv. Phys. **9**, 425 (1960).

[18] G. C. Baldwin and G. S. Kleiber, Phys. Rev. **71**, 3 (1947); Phys. Rev. **73**, 1156 (1948).

[19] A. B. Migdal, Journ. of Phys. **8**, 331 (1944).

[20] A. M. Lane and J. E. Lynn, Nucl. Phys. **11**, 646 (1959).

[21] D. M. Brink, Ph.D. thesis, Oxford University, Oxford, UK, (1955); unpublished.

[22] G. A. Bartholomew, Annu. Rev. Nucl. Sci. **11**, 259 (1961).

[23] T. D. Newton, Can. J. Phys. **34**, 804 (1956).

[24] A. Gilbert and A. G. W. Cameron, Can. J. Phys. **43**, 1446 (1965).

[25] N. Rosenzweig, Phys. Rev. **108**, 817 (1957).

[26] T. Ericson, Nucl. Phys. **11**, 481 (1959).

[27] T. Ericson, Nucl. Phys. **8**, 265 (1958).

[28] A. Bohr, B. R. Mottelson and D. Pines, Phys. Rev. **110**, 936 (1958).

[29] A. G. W. Cameron, Can. J. Phys. **36**, 1040 (1958).

[30] A. G. W. Cameron and R. M. Elkin, Can. J. Phys. **43**, 1288 (1965).

[31] T. von Egidy and D. Bucurescu, Phys. Rev. C **72**, 044311 (2005); **73**, 049901(E) (2006).

[32] T. von Egidy and D. Bucurescu, Phys. Rev. C **80**, 054310 (2009).

[33] R. Capote *et al.*, Nucl. Data Sheets **110**, 3107 (2009).

[34] G. Audi, A. H. Wapstra and C. Thibault, Nucl. Phys. A **729**, 337 (2003).

[35] H. T. Nyhus *et al.*, Phys. Rev. C **85**, 014323 (2012).

[36] S. F. Mughabghab, *Atlas of Neutron Resonances*, (Elsevier, Amsterdam, 2006).

[37] A. V. Ignatyuk, G. N. Smirenkin, and A. S. Tishin, Sov. J. Nucl. Phys. **21**, 255 (1975).

[38] RIPL database as available at https://www-nds.iaea.org/RIPL-3/

[39] T. von Edigy, H. H. Schmidt and A. N. Behkami, Nucl. Phys. A **481**, 189 (1988).

[40] G. Reffo, IAEA-SMR–43 report, 205 (1980).

[41] V. Paar *et al.*, Z. Phys. A **345**, 343 (1993).

[42] F. Garcia *et al.*, Phys. Rev. C **60**, 064311 (1999).

[43] S. Goriely, S. Hilaire and A. J. Koning, Phys. Rev. C **78**, 064307 (2008).

[44] A. J. Koning, S. Hilaire and S. Goriely, Nucl. Phys. A **810**, 13 (2008).

[45] Y. Alhassid, L. Fang, and H. Nakada, Phys. Rev. Lett. **101**, 082501 (2008); private communication.

[46] C. Özen, Y. Alhassid and H. Nakada, Phys. Rev. Lett. **110**, 042502 (2013).

[47] Y. Alhassid, C. Özen and H. Nakada, Nucl. Data Sheets **118**, 233 (2014).

[48] C. Özen, Y. Alhassid and H. Nakada, Phys. Rev. C **91**, 034329 (2015).

[49] Y. Alhassid, S. Liu, and H. Nakada, Phys. Rev. Lett. **99**, 162504 (2007).

[50] K. Kaneko and A. Schiller, Phys. Rev. C **75**, 044304 (2007).

[51] T. von Egidy and D. Bucurescu, Phys. Rev. C **78**, 051301(R) (2008).

[52] N. Cerf, Nucl. Phys. A **554**, 85 (1993).

[53] B. Pichon, Nucl. Phys. A **568**, 553 (1994).

[54] S. I. Al-Quraishi *et al.*, Phys. Rev. C **67**, 015803 (2003).

[55] B. V. Zhuravlev *et al.*, Yad. Fiz. **39**, 264 (1984).
G. N. Lovtsikova *et al.*, Proc. of the 4th International Symposium, Smolenice, Czechoslovakia, June 1985, p. 82, ed. by J. Krištiak and E. Běták.
B. V. Zhuravlev, N. N. Titarenko and V. I. Trykova, Proc. of the OECD Meeting: Nuclear Level Densities, ENEA, Bologna, Italy, November 1989, p. 210, ed. by G. Reffo, M. Herman and G. Maino.
V. G. Pronyaev *et al.*, Yad. Fiz. **30**, 604 (1979); Sov. J. Nucl. Phys. **30**, 310 (1979).
B. V. Zhuravlev, N. N. Titarenko and V. I. Trykova, Proc. of VII International Seminar on Interaction of Neutrons with Nuclei, Dubna, Russia, May 1999, p. 208.

[56] B. V. Zhuravlev, Proc. of VI International Seminar on Interaction of Neutrons with Nuclei, Dubna, Russia, May 1998, p. 161.

[57] A. Wallner, B. Strohmeier and H. Vonach, Phys. Rev. C **51**, 614 (1995).

[58] J. Rekstad *et al.*, Phys. Scr. T **5**, 45 (1983).
M. Guttormsen, T. Ramsøy, and J. Rekstad, Nucl. Instrum. Methods A **255**, 518 (1987).
A. Schiller *et al.*, Nucl. Instrum. Methods A **447**, 498 (2000).

[59] M. Guttormsen *et al.*, Nucl. Instrum. Methods A **374**, 371 (1996).

[60] A. C. Larsen *et al.*, Phys. Rev. C **83**, 034315 (2011).

[61] T. von Egidy, H. H. Schmidt, and A. N. Behkami, Nucl. Phys. A **481**, 189 (1988).

[62] A. Schiller *et al.*, Phys. Rev. C **63**, 021306(R) (2001).

[63] M. Guttormsen *et al.*, Phys. Rev. C **68**, 064306 (2003).

[64] G. A. Bartholomew *et al.*, Adv. Nucl. Phys. **7**, 229 (1973).

[65] C. M. Cullagh *et al.*, Phys. Rev. C **23**, 1394 (1981).

[66] W. I. Furman *et al.*, Phys. Lett. B **44**, 465 (1973).

[67] L. Aldea *et al.*, Z. Phys. A **283**, 391 (1977).

[68] Yu. P. Popov, in *Neutron induced reactions*, Proc. Europhys. Topical Conf., Smolenice, Physics and Applications **10**, 121 (1982).

[69] S. G. Kadmenskii, V. P. Markushev, and V. I. Furman, Sov. J. Nucl. Phys. **37**, 165 (1983); in Russian.

[70] P. Carlos *et al.*, Nucl. Phys. A **172**, 437 (1971).

[71] R. E. Chrien, in *Proc. of the Vth International School on Neutron Physics*, Alushta, Dubna 1987, ed. by B.B. Kolesova and V.R. Sarantseva (Dubna Report No. D3, 4, 17-86-747, 1987).

[72] S. F. Mughabghab and C. L. Dunford, Phys. Lett. B **487**, 155 (2000).

[73] S. Goriely, Phys. Lett. B **436**, 10 (1998).

[74] V. A. Plujko *et al.*, Nucl. Data Sheets **118**, 237 (2014).

[75] J. Kopecky, M. Uhl and R. E. Chrien, Phys. Rev. C **47**, 312 (1993).

[76] J. Kopecky, in *Handbook for Calculations of Nuclear Reaction Data*, Report No. IAEA-TECDOC-1034, 97 (IAEA, Vienna, 1998).

[77] J. Kroll *et al.*, Phys. Rev. C **88**, 034317 (2013).

[78] S. Goriely and E. Khan, Nucl. Phys. A**706**, 217 (2002).

[79] E. Khan *et al.*, Nucl. Phys. A**694**, 103 (2001).

[80] M. Martini *et al.*, Phys. Rev. C **94**, 014304 (2016).

[81] D. Frekers *et al.*, Phys. Lett. B **244**, 178 (1990).

[82] J. Kopecky *et al.*, Phys. Rev. C **95**, 054317 (2017).

[83] R. R. Hilton, in *Proc. of the International Conference on Nuclear Structure*, Dubna, (1976); unpublished.

[84] N. Lo Iudice and F. Palumbo, Phys. Rev. Lett. **41**, 1532 (1978).

[85] F. Iachello, Nucl. Phys. A **358**, 89c (1981).

[86] D. Bohle *et al.*, Phys. Lett. B **137**, 27 (1984).

[87] D. Bohle *et al.*, Phys. Lett. B **148**, 260 (1984).

[88] U. Kneissl, H. H. Pitz and A. Zilges, Prog. Part. Nucl. Phys. **37**, 349 (1996).

[89] W. Ziegler, C. Rangacharyulu, A. Richter, and C. Spieler, Phys. Rev. Lett. **65**, 2515 (1990).

[90] N. Pietralla *et al.*, Phys. Rev. C **58**, 184 (1998).

[91] C. Wesselborg *et al.*, Phys. Lett. B **207**, 22 (1988).

[92] H. Friedrichs *et al.*, Phys. Rev. C **45**, 892 (1992).

[93] J. Margraf *et al.*, Phys. Rev. C **52**, 2429 (1995).

[94] I. Bauske *et al.*, Phys. Rev. Lett. **71**, 975 (1993).

[95] A. Nord *et al.*, Phys. Rev. C **67**, 034307 (2003).

[96] F. Bečvář *et al.*, Phys. Rev. C **52**, 1278 (1995).

[97] M. Krtička *et al.*, Phys. Rev. Lett. **92**, 172501 (2004).

[98] A. Voinov *et al.*, Phys. Rev. C **63**, 044313 (2001).

[99] H. T. Nyhus *et al.*, Phys. Rev. C **81**, 024325 (2010).

[100] A. Chyzh *et al.*, Phys. Rev. C **84**, 014306 (2011).

[101] B. Baramsai *et al.*, Phys. Rev. C **87**, 044609 (2013).

[102] S. Goriely *et al.*, Phys. Rev. C **94**, 044306 (2016).

[103] L. M. Bollinger and G. E. Thomas, Phys. Rev. C **2**, 1951 (1970).

[104] A. Simon *et al.*, Phys. Rev. C **93**, 034303 (2016).

[105] R. Schwengner, S. Frauendorf and A. C. Larsen, Phys. Rev. Lett. **111**, 232504 (2013).

[106] B. A. Brown and A. C. Larsen, Phys. Rev. Lett. **113**, 252502 (2014).

[107] R. Schwengner, S. Frauendorf and B. A. Brown, Phys. Rev. Lett. **118**, 092502 (2017).

[108] K. Sieja, Phys. Rev. Lett. **119**, 052502 (2017).

[109] E. Litvinova and N. Belov, Phys. Rev. C **88**, 031302(R) (2013).

[110] F. Bečvář, Nucl. Instrum. Methods A **417**, 434 (1998).

[111] C. E. Porter and R. G. Thomas, Phys. Rev. **104**, 483 (1956).

[112] A. M. Hoogenboom, Nucl. Instrum. Methods **3**, 57 (1958).

[113] S. T. Boneva *et al.*, Particles & Nuclei **22**, 479 (1991); in Russian.

[114] J. Honzátko *et al.*, Nucl. Instrum. Methods A **376**, 434 (1996).

[115] M. Krtička, Ph.D. thesis, Charles University, Prague, Czech Republic, (2002).

[116] F. Bečvář *et al.*, Nucl. Instrum. Methods B **261**, 930 (2007).

[117] A. A. Bogdzel *et al.*, JINR Report No. P15-82-706, JINR, Dubna, Russia, (1982); in Russian.

[118] S. Agostinelli *et al.*, Nucl. Instrum. Methods A **506**, 550 (2003).

[119] K. S. Krane and R. M. Steffen, Phys. Rev. C **2**, 724 (1970).

[120] D. C. Camp and A. L. van Lehn, Nucl. Instrum. Methods **76**, 192 (1969).

[121] R. G. Helmer, Nucl. Data Sheets **101**, 325 (2004).

[122] C. W. Reich, Nucl. Data Sheets **113**, 2537 (2012).

[123] K. Wisshak, F. Käppeler, Nucl. Instrum. Methods **227**, 91 (1984).
K. Wisshak *et al.*, Report KfK-4652, Kernforschungszentrum Karlsruhe, (1989).
K. Wisshak *et al.*, Nucl. Instrum. Methods A **292**, 595 (1990).

[124] M. Heil *et al.*, Nucl. Instrum. Methods A **459**, 229 (2001).

[125] R. Reifarth *et al.*, Nucl. Instrum. Methods A **531**, 530 (2004).

[126] M. Jandel *et al.*, Nucl. Instrum. Methods Phys. Res. B **261**, 1117 (2007).

[127] P. W. Lisowski *et al.*, Nucl. Sci. Eng. **106**, 208 (1990).

[128] J. M. Wouters *et al.*, IEEE Trans. Nucl. Sci. **53**, 880 (2006).

[129] C. W. Reich, Nucl. Data Sheets **108**, 1807 (2007).

[130] B. Singh, Nucl. Data Sheets **93**, 243 (2001).

[131] C. W. Reich and B. Singh, Nucl. Data Sheets **111**, 1211 (2010).

[132] N. Nica, Nucl. Data Sheets **141**, 1 (2017).

[133] D. A. Brown *et al.*, Nucl. Data Sheets **118**, 1 (2018).

[134] S. S. Dietrich and B. L. Berman, At. Data and Nucl. Data Tables **38**, 199 (1988).

[135] M. Jentschel *et al.*, Journ. of Instrum. **12**, P11003 (2017).

[136] C. Guerrero *et al.* (n_TOF Collaboration), Nucl. Instrum. Methods A **608**, 424 (2009).

[137] C. Guerrero *et al.* (n_TOF Collaboration), Eur. Phys. J. A **49**, 27 (2013).

List of Figures

List of Tables

Appendices

Appendix A

Two-step γ cascades following thermal neutron capture in ^{155,157}Gd

Authors:

S. Valenta, F. Bečvář, J. Kroll, M. Krtička and I. Tomandl

Published:

Physical Review C **92**, 064321 (2015).

Appendix B

Examination of photon strength functions for ^{162,164}Dy from radiative capture of resonance neutrons

Authors:

S. Valenta, B. Baramsai, T. A. Bredeweg, A. Couture, A. Chyzh, M. Jandel, J. Kroll, M. Krtička, G. E. Mitchell, J. M. O'Donnell, G. Rusev, J. L. Ullmann and C. L. Walker

Published:

Physical Review C **96**, 054315 (2017).